공학박사 학위논문

A STUDY ON THE CENTRIFUGAL FORCE-BASED FLUIDIC SYSTEM FOR BIOMEDICAL APPLICATIONS

원심력 기반 유체 시스템의 생물의학적 응용에 관한 연구

2017 년 2 월

서울대학교 대학원

협동과정 바이오엔지니어링 전공

박 지 흠

A STUDY ON THE CENTRIFUGAL FORCE-BASED FLUIDIC SYSTEM FOR BIOMEDICAL APPLICATIONS

원심력 기반 유체 시스템의 생물의학적 응용에 관한 연구

지도 교수 김 희 찬

이 논문을 공학박사 학위논문으로 제출함

2016 년 10 월

서울대학교 대학원

협동과정 바이오엔지니어링 전공

박 지 흠

박지흠의 공학박사 학위논문을 인준함

2016 년 12 월

위 원 장 최 영 빈 (인)

부위원장 김 희 찬 (인)

위 원 이 정 찬 (인)

위 원 박 중 열 (인)

위 원 김 원 정 (인)

Ph. D. Dissertation

A STUDY ON THE CENTRIFUGAL FORCE-BASED FLUIDIC SYSTEM FOR BIOMEDICAL APPLICATIONS

BY

JIHEUM PARK

FEBRUARY 2017

INTERDISCIPLINARY PROGRAM IN

BIOENGINEERING

THE GRADUATE SCHOOL

SEOUL NATIONAL UNIVERSITY

A STUDY ON THE CENTRIFUGAL FORCE-BASED FLUIDIC SYSTEM FOR BIOMEDICAL APPLICATIONS

BY

JIHEUM PARK

INTERDICIPLINARY PROGRAM IN BIOENGINEERING

THE GRADUATE SCHOOL

SEOUL NATIONAL UNIVERSITY

THIS DISSERTATION IS APPROVED FOR THE DEGREE OF DOCTOR OF PHILOSOPHY

DECEMBER 2016

Approved by Thesis Committee:

Professor _____ **Chairman**
Young Bin Choy, Ph. D.

Professor _____ **Vice chairman**
Hee Chan Kim, Ph. D.

Professor _____ **Member**
Jung Chan Lee, Ph. D.

Professor _____ **Member**
Joong Yull Park, Ph. D.

Professor _____ **Member**
Wonjung Kim, Ph. D

Abstract

A STUDY ON THE CENTRIFUGAL FORCE-BASED FLUIDIC SYSTEM FOR BIOMEDICAL APPLICATIONS

BY

JIHEUM PARK

INTERDICIPLINARY PROGRAM IN BIOENGINEERING

THE GRADUATE SCHOOL

SEOUL NATIONAL UNIVERSITY

This dissertation focuses on the design, fabrication, evaluation, and application of a centrifugal force-based fluidic system based on macro and micro scale engineering disciplines. Unlike other fluid control forces including electrical force, compression force, magnetic force, etc., centrifugal force is capable of manipulating fluids ranging from macro- to micro-scales with high efficiencies

regardless of fluid properties. Accordingly, centrifugal force has been extensively used for a great number of biomedical applications.

However, the design optimization of such centrifugal force-based fluidic system for practical use is still under investigation due to the inadequate integrating technique, especially for clinical settings, and the strong dependency on geometric designs within spatially varying three different rotational forces (centrifugal, Coriolis, and Euler forces) to precisely regulate the flow of the fluid. Therefore, this dissertation aims to develop a centrifugal force-based fluidic system appropriate for either clinical or biological research environment based on thorough investigations of the fluid flow, the environments created by the rotational forces, and the geometric designs of the system at both the macro- and micro-scale.

The macro-scale study involves the evaluation of design strategies for developing a smart all-in-one cardiopulmonary circulatory support device (CCSD) applicable to diverse clinical environments (emergency room (ER), intensive care unit (ICU), operation room (OR), etc.) (Chapter 2, Section 2.1), the evaluation of hemolytic characteristics of centrifugal blood pump (Chapter 2, Section 2.2), and the evaluation of drug sequestration (Chapter 2, Section 2.3) in CCSD component. Smart all-in-one CCSD equipped with a qualified low hemolytic centrifugal blood pump developed in this study resulted in low hemolysis with a free plasma hemoglobin level far less than 50 mg/dL, and an oxygenator membrane made of polyurethane fibers was turned out to be especially susceptible to the analgesic drug loss (41.8%). The micro-scale study involves the numerical evaluation of the Coriolis effects on fluid flow inside a

rotating microchannel (Chapter 3, Section 3.1), the feasibility study for the development of a centrifugal microfluidic-based viscometer (Chapter 3, Section 3.2), the evaluation of hypergravity-induced spheroid formation (Chapter 3, Section 3.3), and the cellular adaptation study to hypergravity conditions using human adipose derived stem cell (hASC) and human lung fibroblast (MRC-5) (Chapter 3, 3.4). Application studies performed under fundamental understanding of the microfluidic flows in rotating platform demonstrated new potential uses for centrifugal microfluidic technologies especially for cell research, revealing that hypergravity conditions can be an important environmental cues affecting cellular interactions.

Through evaluating various types of centrifugal force-based fluidic system designs for both practical applications and bench-scale experiments, considerable potential of centrifugal force-based fluidic system for introducing new paradigms in the development of medical devices and biomedical research has been demonstrated. The unprecedented integration technique to further miniaturize and improve usability of the centrifugal force-based system might facilitate product innovations, fostering its wide acceptance in the future (Chapter 4).

Keywords : centrifugal force, fluid manipulation, cardiopulmonary support system, centrifugal microfluidics, product design and development

Student Number: 2012-21018

Contents

List of Tables

List of Figures

Fig. 3.3.5 Statistical analysis for sphericity and size. Sphericity and size variations at 24h, Day2, and Day3 for (A, C) hASC and (B, D) MRC-5 were compared and analyzed. Mean sphericity was significantly greater with CMS formation method compared to WPS formation method for all three time durations for both cell types. However, in CMS formation method, the higher RPM undermined sphericity compared to the lower RPM from Day2 for hASC and from Day3 for MRC-5. Standard deviations for sphericity which may indicate shape consistency was significantly greater with CMS formation method compared to WPS formation method at 24h and Day2, but such effects disappears at Day3 for both cell types. Degree of size reduction was significantly greater with WPS formation method compared to CMS formation method despite of the same well sizes designed for both WPS and CMS formation method. While no significant effects on size reduction by different hypergravity conditions were found for hASC, 2000 RPM significantly reduces size compared to 1000 RPM for MRC-5. Standard deviations for size which may indicate size consistency were significantly less for spheroids under 2000 RPM compared to those under 1000 RPM and WPS formation method at all three hour durations, suggesting that

Chapter 1

Introduction

1.1. Centrifugal force

The motion of an object can only be described in respect to others. Therefore, descriptions for the object status can differ by coordinate systems, which is called frame of reference.

In rotating system, there is only one force that exists in real: centripetal force directed toward the center of a circular path, preventing the object from leaving the path and keeping it in a circular motion. It is the force that can be

perceived in an inertial reference frame. However, the forces that govern the motion of the object in the rotating system is three fictitious forces that exist only in the rotating reference frame and do not exist in others. Centrifugal force (f_ω) is one of the three fictitious rotating forces including Coriolis force (f_C) and Euler force (f_E) that apparently act on the object in the rotating reference frame.

According to equations for the three rotating forces, the force vectors are determined by angular velocity ($\vec{\omega}$), rate of angular velocity ($\frac{d\vec{\omega}}{dt}$), position of the object from the center (r), velocity of the object ($\vec{u}$), and mass of the object (m). The Coriolis force and Euler force are perpendicular in respect to the centrifugal force which is radially outward (Fig. 1.1.1).

$$\vec{f}_\omega = m\omega^2\vec{r} \tag{1.1.1}$$

$$\vec{f}_C = -2m\vec{\omega}\times\vec{u} \tag{1.1.2}$$

$$\vec{f}_E = -m\frac{d\vec{\omega}}{dt}\times\vec{r} \tag{1.1.3}$$

1.2. Centrifugal force-based biomedical system

Centrifugal force has been utilized for developing various biomedical systems both in macro- and micro scale. Pressure difference created by centrifugal force determines motion of the fluid. Therefore, centrifugal force-based biomedical systems are generally involved in fluid manipulation.

Macro system includes left ventricular assist device (LVAD), right ventricular assist device (RVAD), biventricular assist device (BIVAD),

extracorporeal membrane oxygenation (ECMO), and cardiopulmonary bypass (CPB) which all can include a centrifugal blood pump for assisting blood perfusion throughout the human body. All of these systems belong to a *cardiopulmonary support system* as their clinical role is to take functions of heart and lung artificially.

Micro system includes assays for nucleic acid analysis, blood analysis, immunoassay, etc. by utilizing diverse fluidic manipulation strategies such as mixing, valving, flow switching, metering, and sequential loading [1]. Therefore, two primary efforts have been made in *centrifugal microfluidic biochips*; to develop or improve strategies for each functional unit and to develop integrated systems aiming at certain biomedical applications or diagnosis.

Both macro and micro centrifugal force-based fluidic systems pursuit miniaturization to develop even smaller and more portable system without any functional deficit.

1.2.1. Cardiopulmonary support system: Macro-scale

Historically, cardiopulmonary support system, which was used to be called heart-lung machine in the past, was firstly constructed by physiologist Maximillian von Frey in 1885, but not feasible until discovery of heparin in 1916. In 1953, Jone Heysham Gibbon was the first surgeon succeeded in open heart surgery utilizing the heart-lung machine [2]. However, it has not been long since centrifugal blood pump became preferable to the use of other pumping devices in cardiopulmonary support system for the blood transfusion.

Roller pump, which processes fluid by compressing the tubing with a number of rollers as a rotor rotates, was the most commonly used until the centrifugal pump from BioMedicus came out in 1978. Superiority of centrifugal blood pump over roller pump has been proved in several pediatric studies [3] but in adult studies it is still controversial [4, 5]. However, recently, use of the centrifugal blood pumps in adult ECMO system is in fact considerably increasing.

Design optimization in terms of size, endurance, efficiency, antitraumatic feature, antithrombogenic feature, and biocompatibility is essentially important in the development of centrifugal blood pump. However, the optimization that allows the product to have both high performance and low hemolytic characteristics is very challenging since design parameters conflict to each other [6]. For example, small gap sizes between housing and impeller improves pump hydraulic performance while more susceptible to damage blood cells [7, 8]. Impeller size and vane designs (e.g. curved vs straight) also affects pump performance and its hemolytic characteristics [9, 10]. Coupling between motor and the pump head is also a critical issue in order to prevent from blood leakage and thrombosis issue. Magnetic suspension techniques have been applied to eliminate such problems, but shaft, bearings, and seals which can accompany durability and hemolysis issue due to constant exposure to mechanical wear and shear stress were incorporated in many of earlier designs since fully suspending the rotating impeller and stabilizing it without any mechanical support are greatly challenging as it involves complex control mechanism [11]. Great advances have been made until now and commercial products currently

available for clinical use minimizes friction and the risk of hemolysis by utilizing pivot bearing [12, 13] or by even realizing bearingless pump [14].

Integrating technique for developing compact and portable cardiopulmonary support system is being increasingly emphasized especially for the use in emergency and intensive care unit (ICU) environment. Miniaturization is essentially helpful not only for patient cohort from distal areas but also for safe interhospital transport during the support [15]. Moreover, recent cases of awake ECMO as bridge to either recovery or transplantation further reveal the importance of ambulatory and miniaturized system [16, 17].

1.2.2. Centrifugal microfluidic biochip: Micro-scale

The history of centrifugal microfluidic technologies began in 1960s with the development of centrifugal chemical analyzer by N. Anderson. Rotating disks were designed to contain channels and optical cuvettes at the outer edge for allowing propulsion of the loaded reagent by centrifugal force and its chemical reactions at the cuvette as the disk rotates. The analyzer has further advanced by incorporating optical technologies to measure light absorbance or transmittance of the reacted reagent, opening new paradigms in centrifugal microfluidics for clinical use. Its evolution has been continued and commercialization efforts by several business groups started to appear. In 1989, Abaxis Inc. began to develop the centrifugal analyzer for blood analyte analysis and introduced Piccolo rotor system that integrates all necessary sample processing steps for the analyte analysis in 1995. The startup company in US, Gamera, introduced further advanced model with microfabrication technique

and demonstrated new possibilities for the application in drug development. In 2000s, new designs for disk-based immunoassay microarrays, protein arrays, and nucleic acid analysis arrays were introduced by several research groups and companies including Gyro AB, Quadraspec, Burstein Technologies, and Advanced Array Technology [18].

Such biomedical applications are basically an integration of each functional unit implemented in rotating platform such as mixing, valving, flow switching, metering, and sequential loading. Therefore, advances in biomedical applications were able to be achieved based on those in each functional unit development. Strategies for the implementation can be classified into two ways; passive and active. Passive control is based on intrinsic forces governed by channel geometries, fluid properties, and rotational forces while active control is by implementing external regulating mechanism such as using magnetic beads for effective mixing [19], electrochemical method for cell capture [20], and laser-actuated ferrowax for fluid routing [21]. The active control can result in more reliable manipulation compared to the passive control, but more complexities on device. Therefore, it is important to use passive and active control simultaneously for effective management based on fundamental forces acting on the centrifugal microfluidic platform, governing fluidic behaviors. There are three other forces; viscous (ΔP_{vi}), capillary (ΔP_{ca}), and fluidic inertia force (ΔP_{in}), that work with rotating forces [Eq. (1.1.1), Eq. (1.1.2), and Eq. (1.1.3)] but which are not based on rotation .

$$\Delta P_{vi} = -R_{hyd} Q \tag{1.2.1}$$

$$\Delta P_{ca} = \sigma \kappa \tag{1.2.2}$$

$$\Delta P_{in} = \rho \ell a \tag{1.2.3}$$

where R_{hyd} is the hydraulic resistance, Q is the volumetric flow rate, σ is the surface tension of the fluid, κ is the curvature of the fluid, ρ is the density of the fluid, ℓ is the channel length, and a is the acceleration of the fluid. For convenience, centrifugal force shown as vector form in Eq. (1.1.1) usually expressed in differential pressures together with the forces shown in Eq. (1.2.1)-(1.2.3) as the following [22].

$$\Delta P_{ce} = \frac{1}{2} \rho \omega^2 (r_2^2 - r_1^2) \tag{1.2.4}$$

where r_1 is the inner radial point, and r_2 is the outer radial point of the liquid column.

Biomedical applications of centrifugal microfluidic platform are being continually expanded such as circulating tumor cell (CTC) isolation [23], blood plasma quantification in protein level [24] , droplet generation platform [25], dengue virus (DV) detection [26], etc., which are all successfully implemented based on systematic integration of functional units. However, as versatility of the system is getting improved, the importance of miniaturization is getting more emphasized while retaining major advantages of centrifugal microfluidic system, compactness and portability [1].

1.3. Research Aims

Research aim of this dissertation is to develop centrifugal force-based fluidic systems in macro- and micro-scales appropriate for clinical or experimental settings and to investigate their new biomedical applications. Both macro- and micro-scale systems described in this study involve product development processes including design, unit operating module development, mock-up production, system integration, and manufacturing. The main purpose of the macro-scale study is to develop a low hemolytic smart all-in-one CCSD that is capable of stably preserving its clinical effectiveness and the main purpose of the micro-scale study is to investigate new potential uses for centrifugal microfluidic technologies especially in cell research.

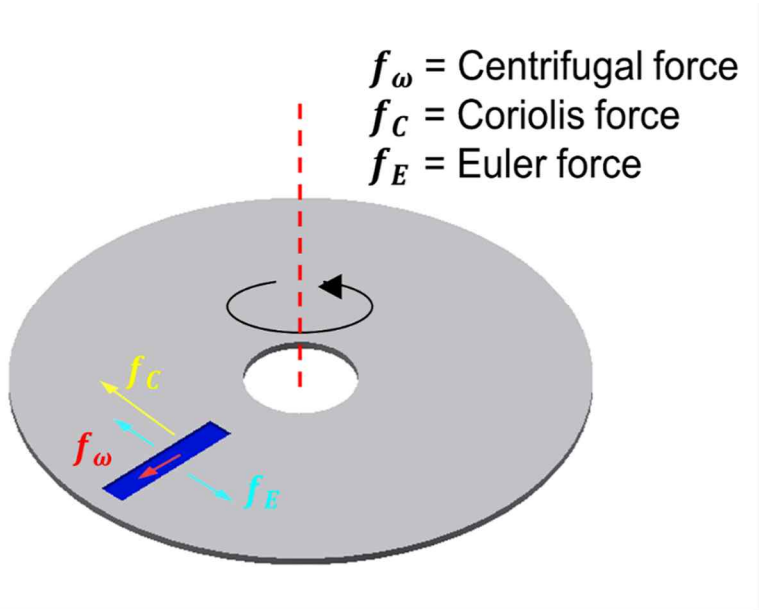

Fig. 1.1.1 The three governing fictitious forces in non-uniformly rotating; Centrifugal force ($f\omega$), Coriolis force (f_C), and Euler force (f_E).

Chapter 2

Macro-scale centrifugal-fluidic system for biomedical application

2.1 Development of a smart all-in-one cardiopulmonary circulatory support device [27]

Cardiopulmonary circulatory support device (CCSD) is composed of cannula, tubing, centrifugal pump head, control system, and oxygenator. However, the system becomes bulky and complex while integrating these components,

leading to difficulties in use for diverse clinical environment including emergency room (ER), operation room (OR), intensive care unit (ICU), etc. Accordingly, this study aimed at developing a portable and cost-effective smart all-in-one CCSD that is capable of interactively and autonomously operating in accord with various indications of patients. By integrating all necessary components including core sensor modules for monitoring patient status into one single device, prototypes of smart all-in-one CCSD with preliminary performance result of pump driver and control unit on a mock circulation loop were presented.

2.1.1 Introduction

Since H1N1 Influenza virus swept the whole world in 2009, extracorporeal membrane oxygenation (ECMO) care, which is one of the representative model of CCSD, has received great attention by discovering high survival benefits with ECMO use for patients suffering from severe respiratory failure.

ECMO system requires a number of sensors and control systems in order to monitor physiological conditions that could vary by patients [28]. Therefore, portability and versatility of the system is very important to appropriately use in the intensive care unit (ICU) environment by achieving compactness of the system and to accommodate different clinical situations. However, most CCSDs currently available in market are highly expensive, bulky, and complicated to use. Accordingly, this study aimed to develop a portable and cost-effective smart all-in-one CCSD that is capable of interactively and autonomously operating in accord with various indications of patients (e.g.

heart failure and lung failure). Maintaining appropriate temperature and flow rate without bubble is a key to successful treatment. Here, blood clotting inside the CCSD circuit and patients' coagulation status are the influential factors, which can be shown by a variation of pressure gradient across the pump or oxygenator. Core sensor modules for monitoring these necessary indications were integrated into a one single portable system throughout conceptual design, rapid prototyping, and the performance test based on mock circulation loop. Functional prototypes of the smart all-in-one CCSD were built and further optimized through *in-vivo* as well as *in-vitro* evaluations. In this study, procedures for product development to achieve clinical approval and ultimately to commercialize the product were presented.

2.1.2 Materials and Methods

Core sensor module preparation

Core sensor modules for smart all-in-one CCSD including brushless DC motor (EC-i40 70W + ENX16EASY, Maxon Motor, Sachseln, Switzerland) with its driving unit (mmc ESCON 50/5, Maxon Motor, Sachseln, Switzerland), clamp-on type ultrasonic flow meter (Jain Technology Co., Ltd, Korea), bubble sensor (ABD06-L, NY, USA), temperature sensor (DTPML-SPI-81, DWELLSHOP, Korea), thrombosis sensor, pressure sensor (HSCDANT030PDSA5, Honeywell Inc., Indiana, USA), Switched-Mode Power Supply (RT-50, Mean Well, Taiwon), Li-polymer battery (MS98106-10A6S1P, MS-TEK, Suwon, Korea), emergency driving unit, and touch user interface (IEC1000Lite-08, HNS, Korea), were prepared (Fig. 2.1.1).

For noninvasive flowmeter, two versions of the flowmeter based on transit time technique were developed, one with V-method in which two transducers are mounted on the same side and the other with X-method in which four transducers are mounted, two on the top and the other two at the bottom by cooperating with Korean business group of Jain Technology Co., Ltd (Fig. 2.1.2). Performance evaluation for the developed clamp-on type ultrasonic flowmeter included measurement of flow and response time at different rotational speed of centrifugal pump. Gold standard data were determined to be weight changes of reservoir according to time as water flows into it. Comparison test with one of the most widely used ultrasonic clamp-on type flowmeter composed of the sensor probe, 9PXL, and its console, TS410, supplied by Transonic Systems Inc was also carried out.

System integration

Printed circuit board (PCB) that includes Micro Controller Unit (MCU) for collecting data from each sensor by serial communication was developed. Collected data were then displayed on the user interface for monitoring. To evaluate feasibility of the product concepts, computer assisted design (CAD) programs (e.g. Rhino, Inventor, and AutoCAD) were used for visualization. Rapid prototyping was then processed by CNC (computer numerical control) laser cutter or 3D printers for design verification. Throughout a number of the evaluation, functional prototypes were manufactured for *in-vivo* as well as *in-vitro* performance test.

Mock circulation loop

A mock circulation loop that comprises a mechanical valve for resistance control, turbine flowmeter for performance evaluation of the developed clamp-on type ultrasonic flowmeter, and two acrylic chambers; one for filling and drining the fluid and the other for compliance control with air pump (Fig. 2.1.3A) was built. *In-vitro* evaluation of the pump was conducted using the mock circulation loop by creating pump performance curve. At defined rotational speed ranging from 1000 to 5000 RPM, pressure differences between inlet and outlet, referred as pressure head, were measured according to the flow rate regulated by resistance valve (Fig. 2.1.3B).

2.1.3 Results and Discussion

Pump performance curve that shows the range of possible operating condition was successfully created for the developed pump head by using the mock circulation loop. Resulted curve well matched with the simulation results. The curve demonstrates the validity of the pump for ECMO and VAD use as it is capable of generating necessary amount of volumetric flow rate at pressure head required for each condition (Fig. 2.1.3B). With the pump driver, the pump performance curve for Capiox SP centrifugal Pump (Terumo Inc, Osaka, Japan) was also able to be reproduced as similar to its real specification.

As a result of the performance evaluation of the developed clamp-on type ultrasonic flowmeter, X-method further improved accuracy of the measurement compared to V-method. Average error significantly reduced from 0.768 L/min with V-method to 0.154 L/min with X-method, achieving high quality of the

performance comparable to that of commercial product, Transonic and NovaFlow ultrasonic flowmeter (Fig. 2.1.4).

Based on the performance test, the product features in terms of casing size, weight, sensor arrangement, user friendliness, etc. were further optimized (Fig. 2.1.5) and finally upgraded to Ver 3 where all sensors were connected by circular connectors to protect internal electrical parts (Fig. 2.1.6).

2.1.4 Conclusion

With further improvements by focusing more on the clinician-oriented usability, an effort to develop smart all-in-one CCSD described here is believed to make a success in the medical market shortly. Particularly for the domestic effort to open up a market for medical ultrasonic flowmeter would bring positive effects to the development of medical technology. Under all these efforts, smart all-in-one CCSD would be constantly upgraded, aiming at the first clinical trial in 2018 with this smart all-in-one CCSD by achieving medical device approval from the Ministry of Food and Drug Safety.

Fig. 2.1.1 Core sensor modules for SACSS

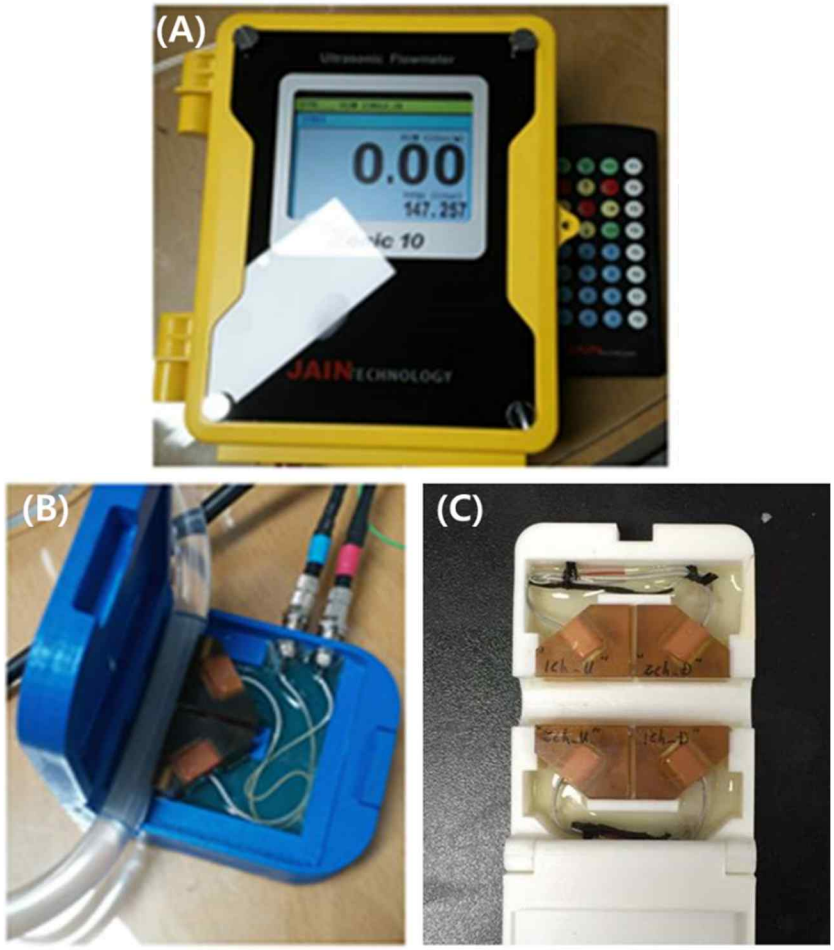

Fig. 2.1.2 (A) A converter with a patented algorithm that identifies optimal frequency automatically which significantly varies by the surrounding environment. (B) V-method flowmeter (C) X-method flowmeter.

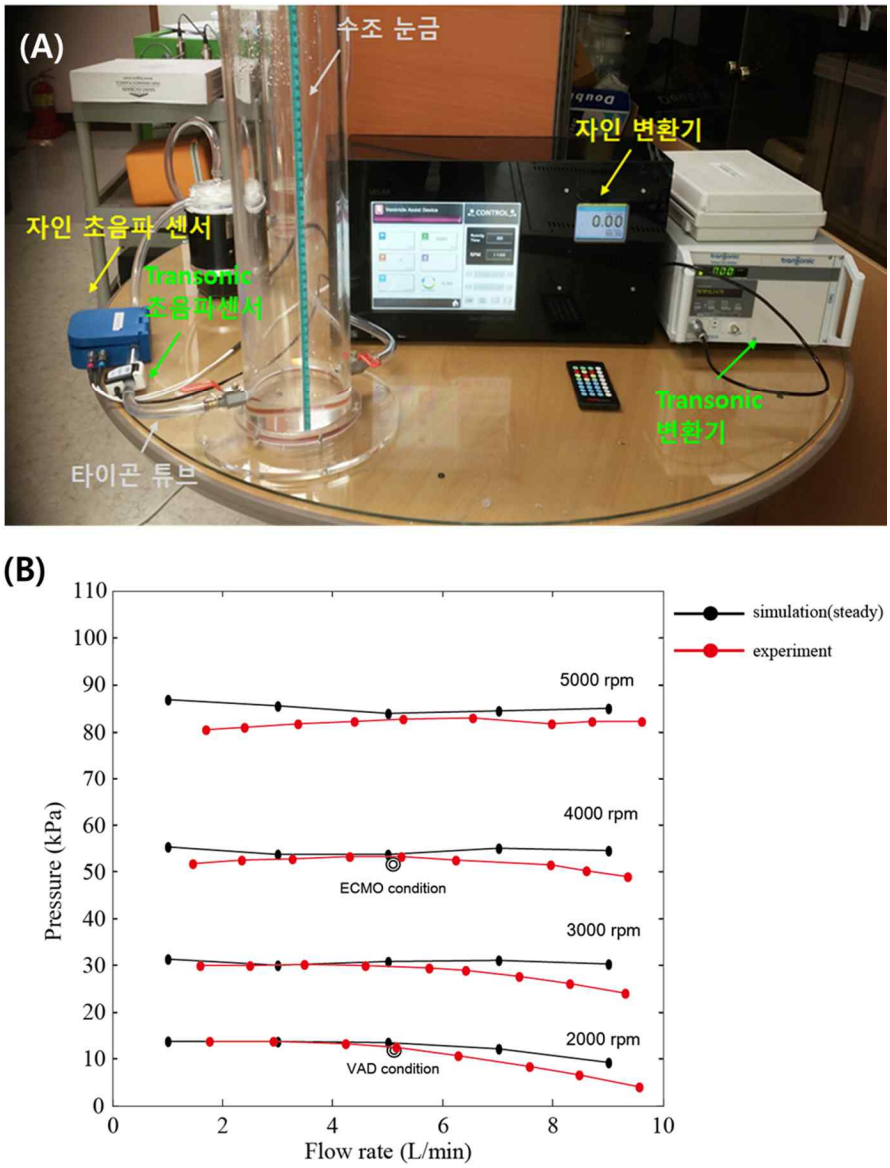

Fig. 2.1.3 (A) Mock circulation loop (B) Pump performance curve created using mock circulation loop

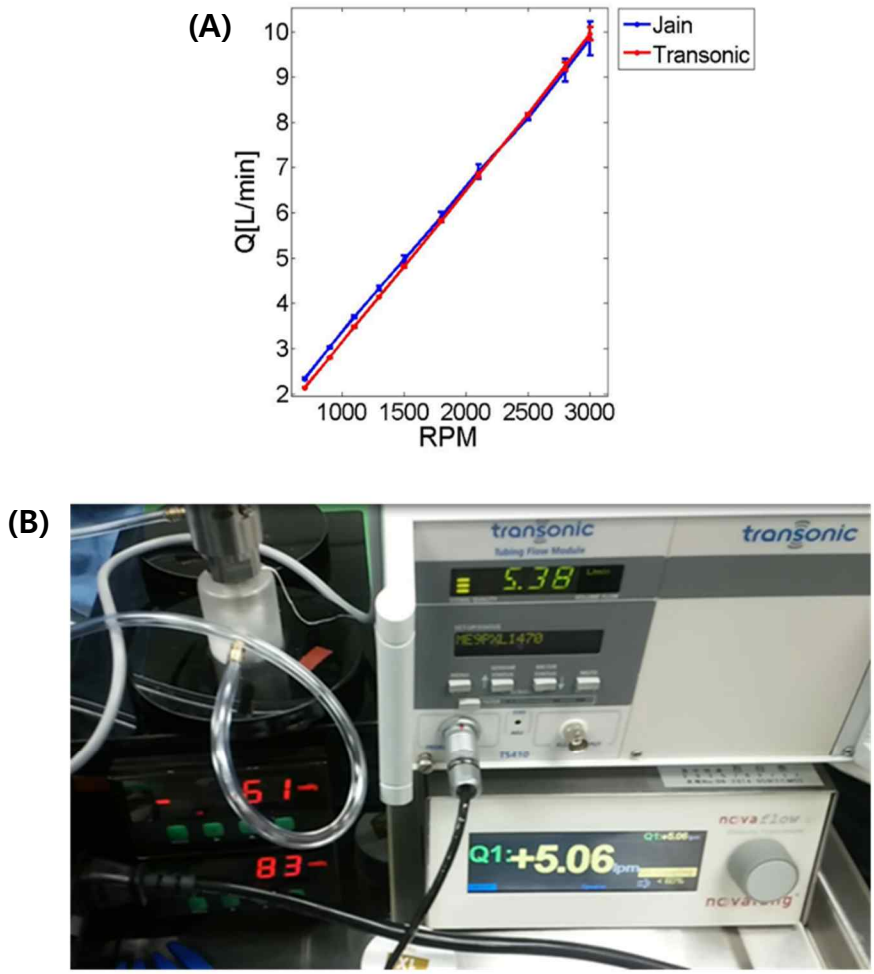

Fig. 2.1.4 In-vitro evaluation of the developed clamp-on type ultrasonic flowmeter based on X-method using (A) water and (B) blood.

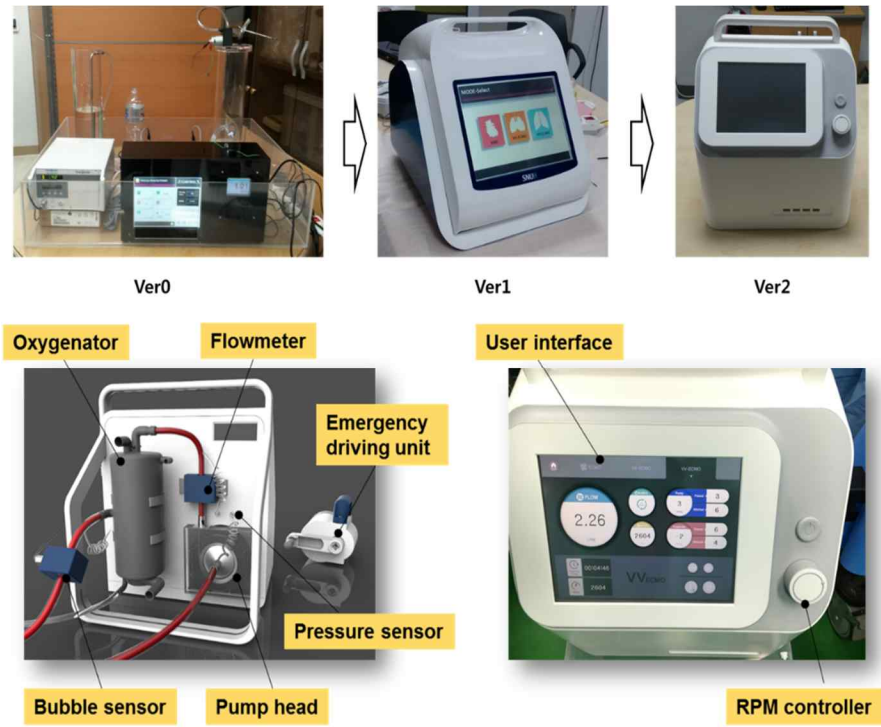

Fig. 2.1.5 Upgrade of the integrated system. Bottom figure shows details of Ver 2 integrated system.

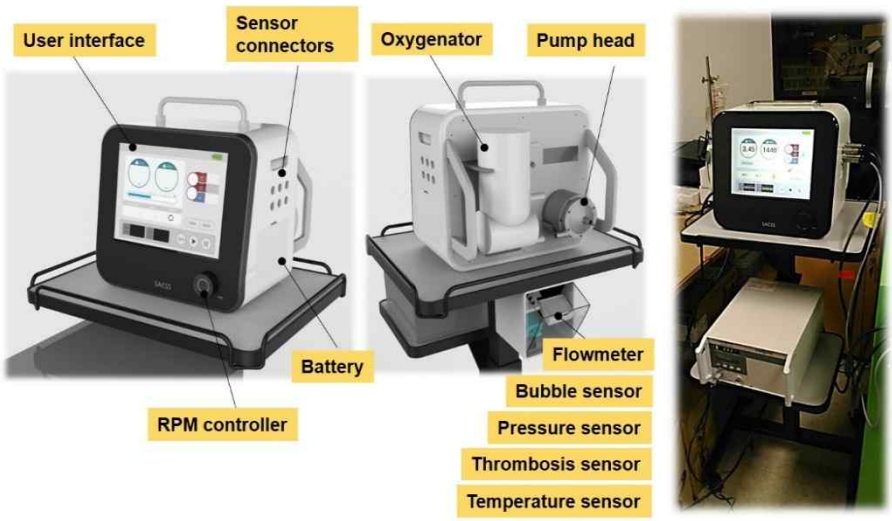

Fig. 2.1.6 Ver 3 integrated system

2.2 Evaluation of hemolytic characteristics of centrifugal blood pump [29]

Development of a low hemolytic centrifugal blood pump is a key for providing undamaged blood to patients during cardiopulmonary support. Hemolytic characteristics of the pump depend on its design, materials, and manufacturing processes. Design and manufacturing optimizations encompass very challenging problems to achieve low levels of hemolysis. In this study, hemolytic characteristics of multiple types of centrifugal blood pumps designed based on computational fluid dynamics (CFD) simulation study were evaluated. Hemolysis test was performed in accordance with American Society of Testing and Materials (ASTM) standards by preparing a circulation loop consisting of blood bag, polyvinyl chloride medical tubing, flowmeter, clamp, pressure sensors, water bath, and thermometer. 450 mL or 500 mL of fresh blood obtained from normal swine was circulated for 6 hours with a flowrate of 5 L/min at a pressure of 100 mmHg. Normalized indices of hemolysis (NIH) was determined by measuring free hemoglobin in plasma every hour. By incorporating pivot bearing, NIH value less than 0.005 g/100L which was comparable to that of commercial product was able to be stably achieved. Developed prototypes for the centrifugal blood pump were also integrated to the smart all-in-one CCSD for *in-vivo* evaluation and the pivot bearing-based centrifugal blood pump resulted in low free plasma hemoglobin (freeHGB) measurement during 6 hours of operation comparable to that resulted from the commercial product.

2.2.1 Introduction

Design of a centrifugal blood pump is an important determinant of its hemolytic characteristics. A number of influential factors are involved in the design criteria such as size, endurance, pump efficiency, antitraumatic feature, antithrombogenic feature, and biocompatibility. However, satisfying all these factors are extremely challenging since they are often opposing to each other (Fig. 2.2.1), requiring design optimization.

Centrifugal blood pump is composed of rotating impeller and housing. In order to rotate impeller without blood leakage, complete isolation of the rotating impeller from an exterior is primarily required. Therefore techniques for fully levitating impeller has been of great interest. However, such techniques involve complex control mechanism regulating six degrees of freedom in three dimensional space, forward/backward, up/down, left/right, pitch, yaw, and roll, making extremely difficult for precise control which would also certainly affect pump performance [30].

In the past, ball bearing that is able to rigidly and stably support shaft of the impeller and assist its rotation has been often used in centrifugal blood pump, but sealing between the shaft and the bearing was always an issue to prevent blood leakage. Ball bearing is composed of inner and outer frames arranged concentrically with one frame fixed and the other rotating. Small balls are placed between these two frames and freely rotates as the frame that grasp the shaft rotates. If such bearing is not completely sealed, blood would leak inside the ball bearing and may rupture blood cells, causing severe hemolysis. The sealing material (e.g. lip seal) would also eventually wear out [31]. Moreover, blood leaked inside the

bearing would result in blood clots. Therefore, seal-less design is associated with antithrombogenic as well as antitraumatic feature. One of the most representative model for centrifugal blood pumps based on ball bearing currently available in market is Capiox SP centrifugal pump (Terumo Inc.)

To minimize contact surfaces and eliminate sealing problem, single or double pivot bearing became more prevalent in centrifugal blood pump design. Pivot bearing is cylindrical bearing with pointed tip at the end, supporting axial load. With pivot bearing, impeller can be rotated without the leakage issue, but the contact area between the tip and the housing can still be the source of hemolysis if the blood cells squeeze into the gap.

Impeller vane design is another influential factor for pump performance and hemolysis. Number of vanes, vane angle, thread depth, shroud or open design, etc. are the antitraumatic feature [6]. Large number of vanes turned out to improve pump performance by creating large pressure gradient and have no significant effects on hemolysis [32]. Comparing 0 and 180 degree curved vanes, the latter turned out to create higher flow [33]. Deeper threads also resulted in best pumping performance [10].

Small priming volume and biocompatibility is also an important issue in the development of centrifugal blood pump. Low hemolysis can be expected with the smaller priming volume by reducing blood exposure to exterior components and therefore reducing external influences such as heating, mechanical friction, and thrombosis [34].

Gap size, surface polishing, and housing design are also related to antitraumatic features and need to be optimized to retain pump performance. For

example, large gaps between impeller and housing provide good surface washing and reduce shear stress, therefore result in low hemolysis, but lower pump efficiency [7, 8, 35]. Surface roughness should be also considered and 0.2mm Ra turned out to be sufficient to provide very low levels of hemolysis [36]. For housing design, effects of different inlet or outlet angle or the number of outlets has been examined, but no different hydrodynamic performance was found [33]. Instead, eccentric inlet turned out to be appropriate design for implantation by securing compactness [37]. Even though there is no distinct effects known for increased number of outlets, current design of centrifugal blood pump integrated to Cardiohelp system (Maquet Inc., Germany) has four outlets.

Depending on pump designs, flow characteristics vary and it is important to eliminate regions that create turbulent flow because shear stress generated by turbulent flow is known to be a major source that causes severe hemolysis. Therefore, hemolysis level can be predicted by analyzing shear stress generated in different pump designs. The magnitude of shear stress and exposure time have been reported to be the main factors that determine the levels of hemolysis. Accordingly, threshold level of shear stress that causes red blood cell damage has been extensively explored in previous literatures [38], suggesting that such threshold shear stress level that causes blood cell damage need to be carefully defined to precisely predict hemolysis by Computational Fluidic Dynamics (CFD) simulation.

In this study, multiple types of centrifugal blood pump based on CFD simulation were developed. By varying bearing type, priming volume, impeller angle, washing hole size, and volute design, prototypes were fabricated in polycarbonate by Computer Numerical Control (CNC) machining. In addition to

pressure and velocity profile analysis, hemolytic characteristics of the prototypes were also predicted by CFD simulation. Prototype designs and simulations were conducted by CFDlab in Sogang University (Seoul, Korea). According to American Society of Testing and Materials (ASTM) standards, hemolysis test for each prototype was carried out to determine the best design for centrifugal blood pump.

2.2.2 Materials and Methods

Prototype design and manufacturing

Prototypes were manufactured based on two types of bearings, ball bearing and double pivot bearing, to develop low hemolytic centrifugal blood pump. CFD simulation including velocity and pressure analysis (Fig. 2.2.2) was performed to examine commercially available centrifugal blood pump (Table 2.2.1) and to compare their numerical results with newly designed prototypes (Prototype 3, Prototype 4, Prototype 4.1, and Prototype 3.4).

Prototype 3, 4, and 4.1 were fabricated with ball bearing and Prototype 3.4 was with double pivot bearing similarly to CP Affinity (Medtronic, Inc.). All prototypes contained shrouded impellers and had six washing holes, while CP Affinity contains an open impeller and has an open path for blood at the center of the impeller. Prototype 4 and 4.1 had smaller priming volume of 19 mL than Prototype 3 which had the priming volume of approximately 23 mL.

Manufacturing process has been improved to reduce surface roughness (Fig. 2.2.3). In order to evaluate an effect of the surface roughness resulted by the manufacturing process used for the prototypes, CP Affinity was fabricated by the

identical manufacturing process to the prototypes.

Moreover, coated Prototype 3 and non-coated Prototype 3 were prepared by dip-coating process to evaluate a coating effects on hemolysis. The coating material was the co-polymer MPC (2-methacryloyloxyethyl phosphorylcholine, Lipidure® CM 5206, NOF Corp., Tokyo, Japan) and chosen thickness was 1 μm by conducting dip-coating process ten times [39].

Hemolysis test

Hemolysis test was performed in accordance with ASTM standards by preparing a circulation loop consisting of blood bag, polyvinyl chloride medical tubing, flowmeter, clamp, pressure sensors, water bath, and thermometer. 450~500 mL of fresh blood obtained from normal swine was circulated for 6 hours with a flow rate of 5 L/min at a pressure of 100 mmHg, an approval criteria for ventricular assist device (VAD) (Fig. 2.2.4). FreeHGB hemoglobin was measured every hour to determine normalized indices of hemolysis (NIH) by following Eq. (2.2.1)

$$N.I.H.g\ /\ 100\ell = \Delta freeHb \times V \times \frac{100-Ht}{100} \times \frac{10}{Q \times T} \qquad (2.2.1)$$

where $\Delta freeHb$ is the increase of plasma free hemoglobin concentration [g/L] over the sampling time interval, V is circuit volume [L], Q is flow rate [L/min], Ht is hematocrit [%], and T is sampling time interval [min].

Animal experiment

For *in-vivo* evaluation, non-coated Prototype 3 and Affinity NT oxygenator

(Medtronic Inc., Annaheim, CA) were incorporated to the functional prototype manufactured for the second version (Ver2) shown in Fig. 2.1.5 and it was applied to the normal swine model within veno-venous (VV) ECMO mode (Fig. 2.2.6). Left and right femoral veins were cannulated with either 17 or 19 Fr cannula. Venous blood drained from the left femoral vein was oxygenated by going through the oxygenator and returned to right femoral vein. Blood circulation was constantly assisted by the centrifugal blood pump and the flow rate was maintained at 1 to 2 L/min for 6 hours. 1 mL of blood was sampled every hour for complete blood count (CBC) and freeHGB measurement. Total three experiments were carried out including control group with Medtronic CP Affinity and Affinity NT oxygenator.

Based on the animal experiment with Ver 2 integrated system, prototype designs were further modified and improved considering clinical environment and user friendliness, producing Ver 3 integrated system (Fig. 2.1.6). Animal experiment with a normal swine model by applying veno-arterial (VA) ECMO mode was carried out with Ver 3 integrated system (Fig. 2.2.7), but without oxygenator in order to evaluate pump performance of Prototype 3.4 only. Using 15 and 17 Fr cannula, blood was drained from right atrium and returned to femoral artery, which would be an injection of opposing flow to blood pumping out from left ventricular. Flow rate was maintained at 1.6 to 2 L/min for 6 hours, and blood samples were analyzed identically to previous animal experiments. Prototype 3.4 was coated with the co-polymer MPC.

Prototype 3 was sterilized by Ethylene oxide (EO) gas but considering that the composing material could be affected by high temperature of about 60

Celsius degrees required for EO gas sterilization, Prototype 3.4 integrated in Ver 3 integrated system was sterilized by gamma irradiation.

2.2.3 Results and Discussion

Total four types of prototypes were designed and manufactured: Prototype3, 4, 4.1 and 3.4. Using these four prototypes, effects of surface roughness, priming volume, surface coating, and bearing type on hemolysis were evaluated.

By improving surface roughness (Fig. 2.2.3), Prototype 3 resulted in NIH of 0.003 g/100L which was comparable value to that of commercial product, Medtronic CP Affinity (Table. 2.2.2). No critical thrombosis was found for both the prototype and the CP Affinity after washing at the end of the experiment. In order to further evaluate the effect of surface roughness created by the machining process on hemolysis, CP Affinity with the identical machining process to the prototypes was fabricated. Shaft for pivot bearing was made of either stainless steel or alumina ceramic, and the tip that contacts with housing surface was made of SFRA500 (Igus Inc.) approved by the US Food and Drug Administration (FDA). NIH value for CP Affinity fabricated by machining resulted in 0.003 g/100L which is slightly greater than that for commercial CP Affinity. This evaluation suggests that hemolytic characteristics of Prototype 3 can be further improved to the level of those of commercial CP Affinity with injection molding process.

However, improved surface roughness was not an ultimate solution for lowering hemolysis. Promising NIH result acquired with Prototype 3 was not reproducible and this Prototype 3 constantly resulted in NIH value greater than

0.01 g/100L in later experiments which was an order difference. To resolve this problem, priming volume has been further reduced in the next version of prototypes from 23 mL for Prototype 3 to 19 mL for Prototype 4 and 4.1. As smaller priming volume was allowed for Prototype 4, ball bearing was placed outside of housing. Another different feature for Prototype 4 was a slanted bottom surface. However, it became venerable to blood leakage outside the housing due to the exterior ball bearing. Fabrication of washing holes on the slanted surface also raised leakage problem inside the impeller due to the limitation by hand making since the washing hole had to be drilled after bonding the slanted plate at the bottom of the impeller, creating small gaps during the drilling process. Moreover, hemolysis results were not improved with Prototype 4. Prototype 4 was then modified to Prototype 4.1 to have ball bearing inside and to have flat surface at the bottom of the impeller as Prototype 3, while smaller priming volume (19 mL) was maintained. However, hemolysis results were not again improved. Both Prototype 4 and 4.1 resulted in NIH value greater than 0.01 g/100L (Table 2.2.3).

Expecting that surface coating may further improve hemolytic characteristics of the pump, the co-polymer MPC has been applied to Prototype 3 and 4.1, and repeated the hemolysis test. Coating thickness was 1um. However, there was no coating effects probably due to the anticoagulant heparin that is already included during blood collecting procedure. Since 0.1 μm thickness is also known to be effective, thinner coating after the manufacturing process is advance to injected molding process would be applied. The co-polymer MPC is hemo-compatible material mainly used for non-thrombogenicity [40].

Ball bearing was then thought to be the source of reason creating unexpected hemolysis. To solve reproducibility issue that was occurred with prototypes having ball bearing (Prototype 3, 4, and 4.1), Prototype 4.1 was further modified to Prototype 3.4 to have the priming volume of 23 mL similar to Prototype 3 and to have a double pivot bearing as CP Affinity. Prototype 3.4 resulted in NIH value less than 0.005 g/100L, which is an acceptable standard for VAD. Although NIH value for Prototype 3.4 turned out be slightly higher than commercial products including Centrimag (Levitronix LLC, Waltham, Mass) [41] and CP Affinity, it could be attributed to surface roughness by machining process and therefore is fully capable of improvement (Fig. 2.2.5).

Blood quality was also an important issue. Blood obtained from a normal swine that experienced robot surgery for hemolysis test (fifth row in Table 2.2.3) resulted in severe hemolysis from initial stage, suggesting that hemolysis results can be greatly influenced by blood quality.

To accurately predict hemolysis in CFD simulation, threshold shear stress level needs to be properly determined. Reynolds shear stress was considered in this CFD simulation. However, according to a recent literature, turbulent viscous shear stress level may need to be considered to further enhance computational model in terms of reliable prediction [38] because Reynolds shear stress belongs to macro scale and therefore have limitations to predict blood cell damage which should belong to micro scale. Hemolysis results are summarized in Table 2.2.3.

In-vitro evaluations with blood to determine hemolytic characteristics of the prototypes were followed by *in-vivo* evaluation by incorporating prototypes to the integrated systems described in section 2.1. Non-coated Prototype 3 was

integrated to Ver 2 system and two experiments with the prototype and one control experiment with CP Affinity were performed. There was no technical problems during the experiments for 6 hours. However, kicking phenomenon which is the vibration of cannulated tubing was frequently occurred probably due to insufficient drainage volume. With saline injection, kicking phenomenon temporarily disappeared and therefore about six bags of saline were used during the 6 hours of experiment. The level of freeHGB was also significantly increased, incurring severe hemolysis compared to the control group. Kicking phenomenon also has been occurred in the control experiment, but only one bag of saline was used. Flow was also frequently dropped and such issue got worse over time, requiring continuous saline injection, while flow was constantly maintained in the control experiment. The hemolysis result from the second experiment where heparin was not administrated during the experiment was approximately more than twice worse compared to that from the first experiment where heparin was administered every hour. Severe coagulation was also apparently seen in the second experiment (Table 2.2.4).

In-vivo evaluation of Prototype 3.4 was conducted by incorporating it with Ver 3 integrated system (Fig 2.1.6). With the Prototype 3.4 coated with biocompatible co-polymer MPC, hemolysis results were dramatically improved without sever coagulation (Fig. 2.2.7). FreeHGB level was successfully maintained below 10 mg/dL, which is comparable to the results from the commercial product, CP Affinity, where freeHGB greater than 50 mg/dL is generally assumed to be severe hemolysis [42]. For *in-vivo* evaluation of Prototype 3.4 with Ver 3 integrated system, total two experiments were

carried out at the same time but Fig. 2.2.7 shows the best result only. The other experimental result turned out to have freeHGB of 29.7 mg/dL at 6 hour which is still far less than 50 mg/dL, but blood pressure of the swine continuously dropped and even epinephrine administration was not so effective, meaning that the swine model was in an abnormal state. In VA mode applied in this animal experiment, blood pumping into femoral artery is the opposite direction of the blood flow pumping out from left ventricular. Since the normal swine model was used here, flow generated by the centrifugal pump equipped in Ver 3 should be affected by large opposing force. However, Prototype 3.4 successfully created approximately 2 L/min which is acceptable range in ECMO use. In real clinical situation, flow drop for VA mode applied to the patient with heart failure is regarded as their heart recovery as it could mean opposing flow has strengthened.

2.2.4 Conclusion

In this study, a low hemolytic centrifugal blood pump was developed by using double pivot bearing and minimizing priming volume. Prototype designs were continually modified based on CFD simulation and validated by hemolysis test conducted in accordance with ASTM standards. Threshold shear stress level needs to be carefully considered to properly predict hemolysis with CFD simulation. In the hemolysis test, pump design, manufacturing process, and blood quality turned out to be important influential factors to develop low hemolytic centrifugal blood pump.

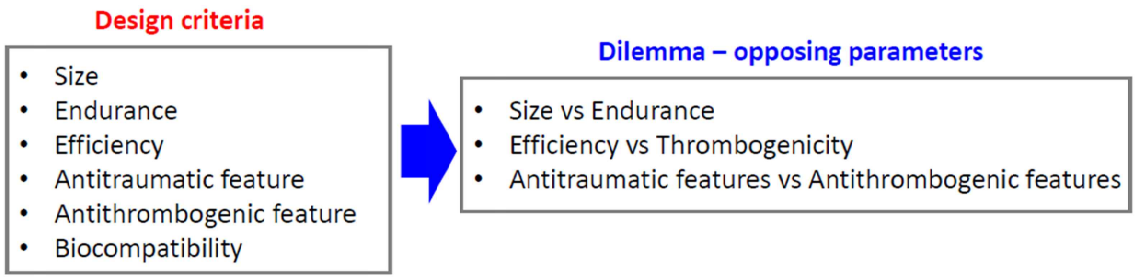

Fig. 2.2.1 Centrifugal blood pump design criteria and its dilemma.

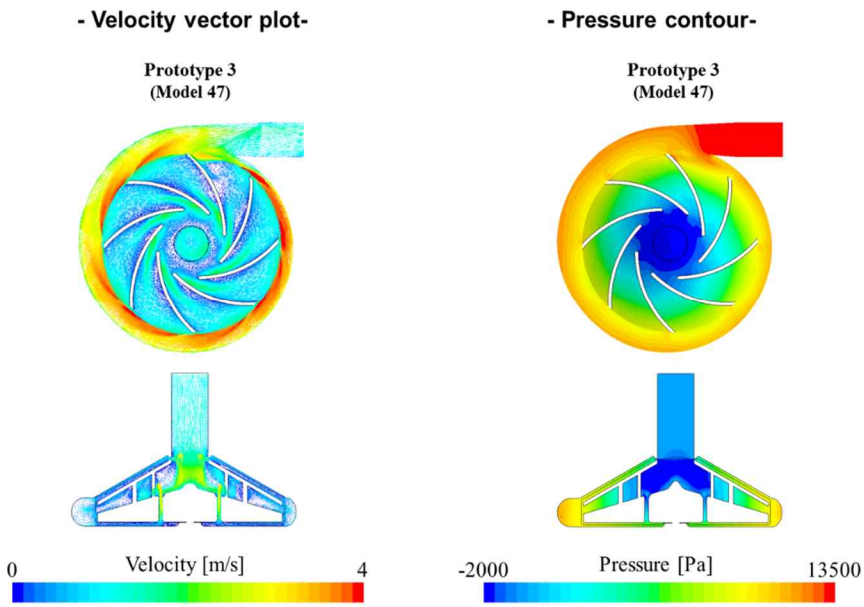

Fig. 2.2.2 Computational fluid dynamics (CFD) simulation for velocity and pressure analysis. Data were provided by CFDlab in Sogang University (Seoul, Korea)

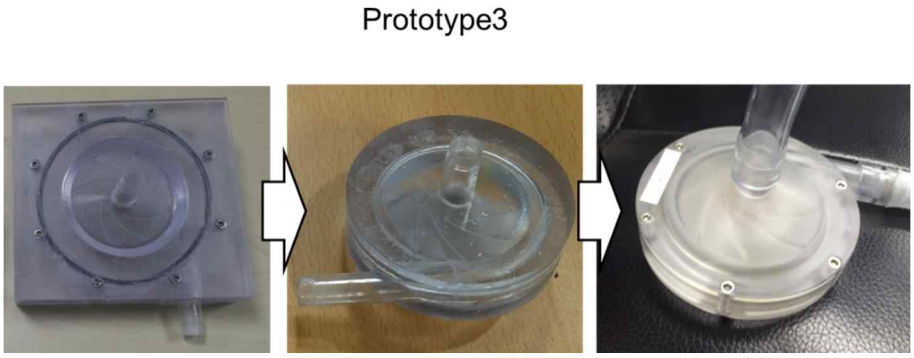

Fig. 2.2.3 Improved manufacturing process to reduce surface roughness.

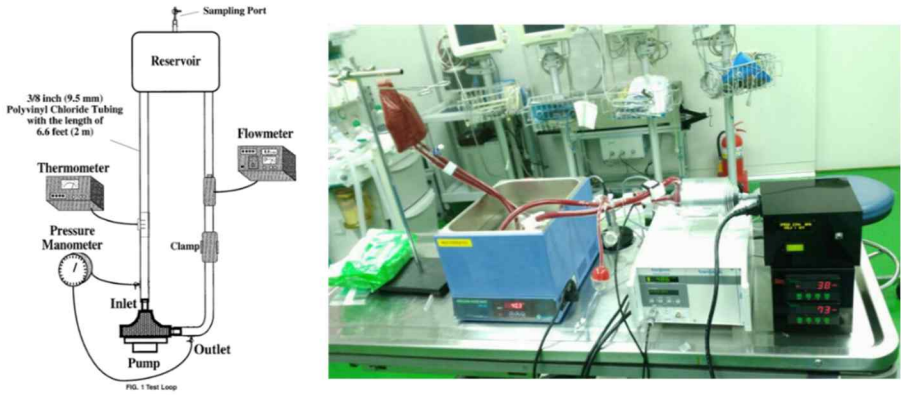

Fig. 2.2.4 Experimental setup for hemolysis test according to American Society of Testing and Materials (ASTM F1841-97).

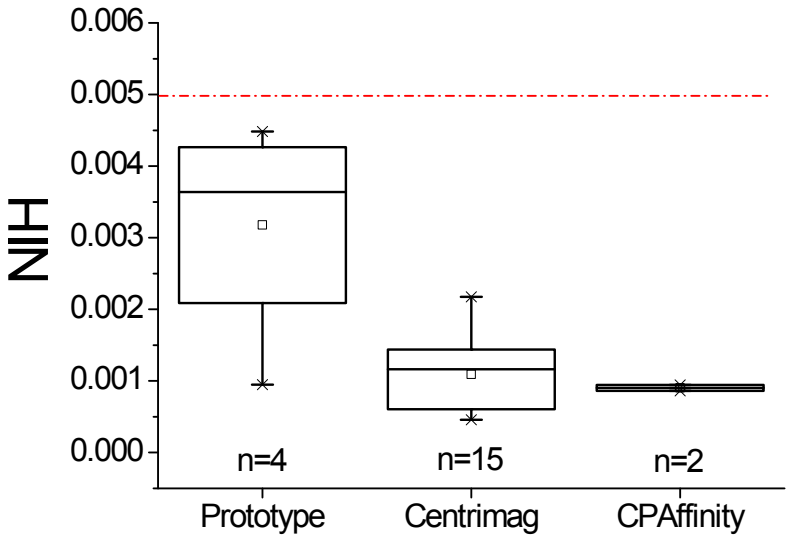

Fig. 2.2.5 Comparison of NIH values among Prototype 3.4 and commercial products, Centrimag [41] and CP Affinity

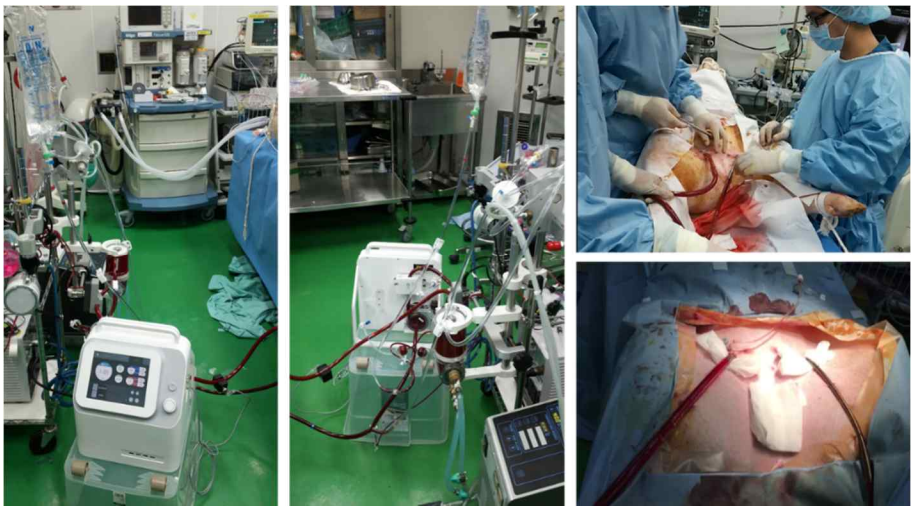

Fig. 2.2.6 In-vivo performance test by applying Ver 2 integrated system to normal swine model within veno-venous (VV) ECMO mode.

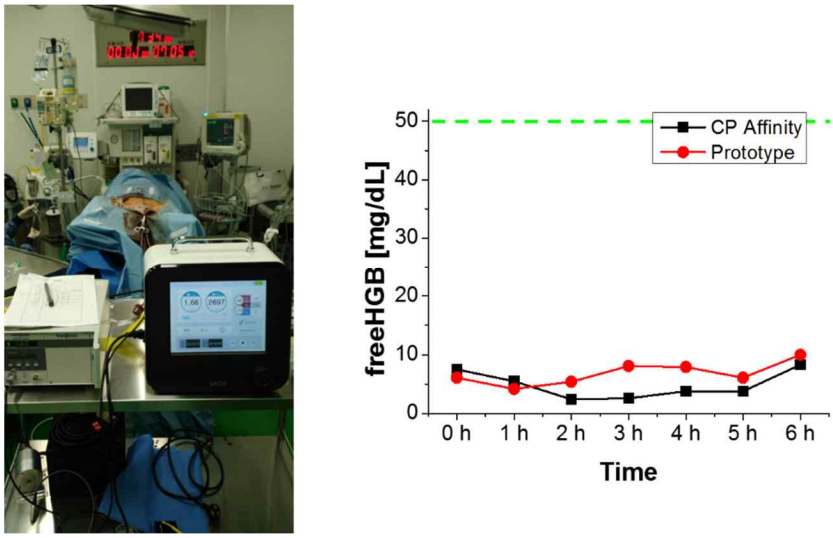

Fig. 2.2.7 Ver 3 *in-vivo* evaluation. Hemolysis level was maintained below 10 mg/dL for 6 h. freeHGB > 50 mg/dL is assumed to be a sign of severe hemolysis [41].

Table 2.2.1 Specifications for commercial products and Prototype 3. Data were provided by CFDlab in Sogang University (Seoul, Korea)

	Medtronic (BIO pump)	Terumo (Capiox)	St. Jude Medical (IsoFlow)	Medtronic (Affinity CP)	Maquet (Rotaflow)	Prototype 3
						
Radius of impeller [mm]	33	39	35	32	25	25
Priming Volume [mL]	80	45	48	40	32	24
Flow rate [L/min]	5	5	5	5	5	5
Rotational speed [rpm]	1830	1217	1452	1850	2200	1865
Head [mmHg]	100	100	100	99	100	101
MIH	3089	999	1502	2049	945	438
Thrombosis [μM]	2.42 E-03	1.10 E-03	1.61 E-03	1.20 E-03	7.28 E-04	6.57 E-04

Table 2.2.2 Hemolytic characteristics of Prototype 3 and commercial product, Medtronnic CP Affinity

Prototype 3 hemolysis test					
	RPM	Flow rate [L/min]	Pressure Head [mmHg]	Volume [mL]	NIH [g/100L]
Exp1	3000	5	270	500	0.172±0.034
Exp2	3000	5	270	500	0.102±0.015
Exp3	2400	5	120	500	0.027±0.002
Exp4	2200	5	150	500	0.003±0.001
Exp5	1800	5	104	450	0.005±0.001
Medtronic CP Affinity hemolysis test					
	RPM	Flow rate [L/min]	Pressure Head [mmHg]	Volume [mL]	NIH [g/100L]
Exp7	2000	5	189	500	0.001±0.001
Exp8	1700	5	114	500	0.001±0.001

Table 2.2.3 NIH results for prototypes and Medtronic CP Affinity. * indicates lipidure coating.

Experimental group							
	Prototype	**RPM**	**Flow rate [L/min]**	**△P [mmHg]**	**Volume [mL]**	**NIH by slope [g/100L]**	**Regression coefficient**
2016.02.04	Prototype3	2200	5	150	500	0.004	0.937
2016.07.14	Prototype4*	2200	5	111	500	0.013	0.931
2016.07.14	Prototype4*	2200	5	139	500	0.011	0.966
2016.07.21	Prototype4*	2200	5	117	500	0.011	0.968
2016.08.18 (blood issue)	Prototype3*	1900	5	96	450	0.035	0.991
2016.08.18	Prototype3*	1800	5	104	450	0.006	0.983
2016.09.23	Prototype4.1	2200	5	114	450	0.014	0.996
2016.09.23	Prototype4.1	2200	5	123	450	0.015	0.991
2016.10.12	Prototype4.1	1950	5	92	450	0.012	0.974
2016.10.12	Prototype3	1850	5	104	450	0.120	0.996
2016.10.12	CP Affinity by machining	1600	5	108	450	0.003	0.550
2016.11.02	Prototype3	1600	5	99	450	0.039	0.964
2016.11.02	Prototype3.4	1700	5	100	450	0.001	0.479
2016.11.02	Prototype3.4	1700	5	98	450	0.004	0.866
2016.11.17	Prototype3.4	1600	5	109	450	0.003	0.848
2016.11.17	Prototype3.4	1700	5	100	450	0.004	0.996
2016.11.24	Prototype3.4 (used)	1600	5	106	450	0.003	0.864
2016.11.24	Prototype3.4(new)	1700	5	97	450	0.003	0.976

Control group							
	Commercial product	RPM	Flow rate [L/min]	△P [mmHg]	Volume [mL]	NIH by slope [g/100L]	**Regression coefficient**
2016.02.18	CP콘	2000	5	189	500	0.002	0.6587
2016.07.21	CP콘	1700	5	114	500	0.000	0.0007

Table 2.2.4 In-vivo evaluation of the Ver 2 and control group with CP Affinity

	Experiment 1	Experiment 2	Control
	freeHGB [mg/dL]	freeHGB [mg/dL]	freeHGB [mg/dL]
0 hour	13.6	9.0	7.5
1 hour	32.3	22.1	5.5
2 hour	36.7	32.9	2.4
3 hour	39.7	45.1	2.6
4 hour	42.0	52.2	3.8
5 hour	42.6	57.9	3.8
6 hour	40.3	91.9	8.3

2.3 Evaluation of drug sequestration in the extracorporeal membrane oxygenation (ECMO) circuit [43]

The influence of the elements of the extracorporeal oxygenation (ECMO) circuit on drug sequestration was quantified by focusing on the interactions between materials and drugs. Tubing of three different brands (Tygon/Maquet/Terumo) and oxygenators of two different brands (Maquet/Terumo) were used. Drugs included dexmedetomidine, meropenem, and heparin which were dissolved in deionized water. Tubing was cut into ~7 cm sections and allowed drug solutions enclosed inside by clamping both ends. The oxygenator housing, gas membrane, and heat exchanger were dissected into ~1 g pieces and submerged into drug solutions. The experimental samples were then immersed in a water bath at 37°C for 1, 6, 12, and 24 h. After 24 h, the dexmedetomidine concentration was significantly reduced in all three types of tubing (<30.1%), the oxygenator heat exchanger from Maquet Inc. (41.8%), and the gas exchanger from Terumo Inc. (8.6%), while no significant losses were found for meropenem and heparin compared to the control group. The heparin concentration within the Maquet gas exchanger, on the other hand, increased significantly compared to the control group at 1 and 12 h ($p<0.05$). The in-vitro study reveals that material selection is a vital part of ECMO development.

2.3.1 Introduction

Extracorporeal membrane oxygenation (ECMO) is an essential therapy for

patients suffering from acute respiratory or cardiac failure, which supports blood oxygenation and circulation for a long period [44, 45]. Therefore, the constituents of the ECMO circuit, including the tubing, blood pump, and oxygenator, are a vital part of patients' body during the treatment by engaging in their complex physiological processes. A major complication of ECMO treatment is significant changes in pharmacokinetics of drugs injected into the patients for antibiosis, sedation, analgesia, or anticoagulation, which frequently leads to therapeutic failure due to drug sequestration in the ECMO circuit [46].

Because the physiological conditions, materials of the ECMO circuit, and drug characteristics differ among patients, products, and drugs, respectively, such drug sequestration is likely associated with several conditioning factors. Potential determinants of the altered pharmacokinetics revealed by previous studies include molecular size, degree of ionization [47], lipophilicity [48], plasma protein binding [49], type of priming solution [50], and type of pump or oxygenator [51]. However, the responsible factor is unclear, likely due to improperly controlled experiments.

For example, although materials used to manufacture each component of the ECMO circuit and those for surface coating vary among products, most previous studies involved *ex-vivo* experiments using an entire ECMO circuit [52] rather than focusing on individual components of the circuit. Therefore, these studies failed to identify out the constituents with the greatest influence on drug sequestration.

This study aimed to quantify the influences of each circuit element on drug sequestration by focusing on the interactions between materials and drugs.

Deionized water was used as the base solution for dissolving each drug to minimize other influential sources related to ionic reactions. The drugs used in this in vitro study were the antibiotic meropenem, analgesic dexmedetomidine and anticoagulant heparin.

2.3.2 Materials and Methods

ECMO circuit materials and components

The ECMO circuit components that are in contact with circulating blood are the tubing, pump housing, impeller, connector, gas exchanger, heat exchanger and oxygenator housing. Because the pump housing, impeller, connector, and oxygenator housing are made of polycarbonate (PC), the materials that need to be assessed for drug loss are the tubing, gas exchanger, heat exchanger, and oxygenator housing. Accordingly, a total of 132 samples including the controls for drug loss at 22°C (R) and at 37°C (C) were analyzed for each drug at 1, 6, 12, and 24 h. Regarding tubing, Tygon S-50-HL Medical tubing (T), Maquet Bioline-coated tubing (B), and Terumo X-coated tubing (X), were evaluated. The Quadrox PLS and Capiox RX oxygenators were disassembled into a gas exchanger, heat exchanger, and housing. The Maquet Quadrox PLS oxygenator is composed of polymethylpentene (PMP) microporous fibers for gas exchange (MaG), polyurethane (PU) fibers for heat exchange by water flow (MaW), and a polycarbonate (PC) housing (MaH), all of which have a Bioline coating. The Terumo Capiox RX oxygenator is composed of polypropylene (PP) microporous fibers for gas exchange (TeG), a stainless steel heat exchanger (TeW), and PC housing (TeH), all of which have an Xcoating. The Maquet and

Capiox ECMO circuits are adult-sized (Fig. 2.3.1).

Circuit sample preparation

Disassembled components of oxygenators (MaG, MaW, MaH, TeG, TeW and TeH) were dissected into ~1 g sections. Because circulating blood contacts only the inside of the tubing, the tubing was cut into ~7 cm sections in order to enclose ~3.5 mL of drug solution by clamping both sides. All ECMO circuit components (T, B, X, MaG, MaW, MaH, TeG, TeW and TeH) were then sterilized by ethylene oxide (EO) gas (Fig. 2.3.2A).

Drug solution preparation

Drugs were dissolved in deionized (DI) water to minimize ionic effects on the drug loss. Drug solutions with initial concentrations of 0.0075 μg/mL, 0.015 mg/mL and 1 U/mL for dexmedetomidin (Sigma-Aldrich, Cat. No. SML0956), meropenem (Sigma-Aldrich, Cat. No. M2574), and heparin (Sigma-Aldrich, Cat. No. H5515) respectively were prepared in a 1000 mL volume. Initial concentrations of all drugs were chosen based on the actual dose used for ECMO treatment of adults [48]. Because that meropenem is soluble in methanol, high concentrated meropenem solutions in <1 mL methanol was first prepared, and then diluted with DI water to 1000 mL. A heparin concentration of 1 U/mL was used based on the amount of initial bolus injection (50-100 U/kg body) specified in the Extracorporeal Life Support Organization (ELSO) criteria assuming that the average weight and blood volume of an adult human male, are 70 kg and 5 L, respectively.

Experiment procedure

For each drug, four groups of 11 samples (R, C, T, B, X, MaG, MaW, MaH, TeG, TeW and TeH) were prepared for evaluation of drug loss at four time points. Each sterilized oxygenator component was placed in a 30 mL amber glass bottle, to which was added 25 mL of the drug solution. Two control groups, R and C, were also prepared by introducing 25 mL of the drug solution into 30 mL amber glass bottles that did not contain materials. Each sterilized section of tubing was filled with 3.5 mL of the drug solution by clamping both sides. Four groups of 10 samples, excluding the control group R, were placed in a water bath maintained at 37°C with agitation at 30 RPM (Fig. 2.3.2B), while the four control groups (R) remained at room temperature (22°C).

At 1, 6, 12, and 24 h, samples were withdrawn from the water bath and aliquots of the drug solutions were collected into screw-cap freeze vials and stored at -80°C prior to analysis. Three identical experiments were carried out for each drug.

Measurement of drug concentrations

Concentrations of dexmedetomidine and meropenem in samples were determined by liquid chromatography-tandem mass spectrometry (LC-MS/MS), and those of heparin in samples were determined using an analytical procedure described previously [53]. A UV-1800 UV-VIS spectrophotometer (Shimadzu Europe GmbH, Germany) was used to measure absorbance at 631 nm.

Statistics

The amount of remaining drugs is described as a percentage. Student's two sample t-test, which is appropriate for use with small sample sizes ($N \leq 5$) so long as the effect size is large ($D > 0.8$) [54], was conducted to assess differences between the control group C and other samples at each time point using MATLAB (The Mathworks, Inc., Natick, MA, USA) "ttest2" function. To apply variance type for the two-sample t-test, homogeneity of variances was tested using SPSS 17.0 for Windows (SPSS, Inc., Chicago, IL, USA). Statistical analyses were performed at the 0.05 significance level.

2.3.3 Results

Concentration of dexmedetomidine was significantly reduced in all three types of tubing (T, B, and X) compared to the control group C. Among the three, B exerted the greatest influence on drug adsorption, and exhibited a significant 20% loss at 1 h to 30% loss at 24 h. T also showed significant loss from 12 h and X from 6 h (Fig. 2.3.3). Among the oxygenator samples, MaW showed significant loss from 6 h and 42% was lost at 24 h. TeG, which is stainless steel, also showed significant loss at 24 h (Fig. 2.3.3 and Table 2.3.1).

Meropenem exhibited no significant loss compared to the control group C, which also showed decreasing concentration over time (12% loss at 24 h) (Fig. 2.3.3). However, the meropenem solution that remained at room temperature (R) did not exhibit such instability, suggesting temperature to be the cause of the drug loss. A previous study in ECMO circuits also demonstrated chemically

unstable characteristics of meropenem in blood, showing an 80% loss in the experimental group and 58% loss in the control group, which remained at 37°C [48]. Compared to the control group R, however, all three types of tubing (20% loss for T, 9% for B and X), MaW (9% loss), MaH (11% loss), and TeW (15% loss) showed significant losses at 24 h (Table 2.3.1).

No significant loss of heparin occurred for any material (Table 2.3.1). However, the concentration within MaG was greater than the control group at all time points, possibly due to the heparin-based Bioline surface coating, while other samples were similar to the control groups R and C (Fig. 2.3.3).

Compared to meropenem and heparin, dexmedetomidine exhibited relatively early loss, as expected from a previous report that dexmedetomidine in a blood-primed ECMO circuit was absorbed, with a maximum 73% loss after 1 h [55]. Unlike meropenem, dexmedetomidine and heparin were chemically stable at 37°C; therefore, both R and C showed similar results, with no significant losses (Fig. 2.3.3)

2.3.4 Discussion

Most previous studies related to drug sequestration in ECMO circuits used the entire circuit primed with either saline or blood, in which interactions among all combinations of materials composing the circuit and those of ions included in the base solution are involved. Mehta et al. demonstrated that drug losses and their stability can differ not only by drug type but also by the base solution. For example, 71.8% and 15.4% of ampicillin was lost in a crystalloid-primed and blood-primed circuit after 24 h of circulationAmpicillin samples stored in glass

jars for the control group, one in crystalloid and the other in blood, also exhibited different concentrations at 24 h; i.e., 0% versus 38.6%, demonstrating that complex chemical mechanisms are involved in drug loss [50]. Besides chemical factors, drug loss in the ECMO circuit could be associated with mechanical factors, as blood in the circuit moves with varying flow rates or pressures, being continuously exposed to friction with component surfaces. Therefore, to identify determinants of drug loss in ECMO circuits, the experimental setup must be optimized. Accordingly, the blood path in the ECMO circuit and the component materials in contact with blood during ECMO treatment was identified. A base solution of DI water was used to minimize ionic influences and investigated concentration changes of each drug by individual components.

The greatest loss of dexmedetomidine occurred with B and MaW, all of which are from Maquet Inc. Because there was no significant difference in concentration from MaH and TeH over time, the only difference between which is the surface coating materials, the coating material might not be the cause of drug loss. Moreover, although B showed the greatest decrease in dexmedetomidine concentration, considering that there was no significant difference in the concentrations among the three tubing types, the tubing material could be the source of the cause rather than coating material. Indeed, Preston et al. demonstrated that uncoated polyvinyl chloride (PVC) tubing was the primary cause of fentanyl and morphine sulfate loss and both Bioline coated Quadrox D (Maquet Cardiopulmonary, AG Hirrlingen, Germany) and X-coated Terumo Baby Rx (Terumo Cardiovascular Systems Corp., Ann Rbor, MI) had

very little effect [56]. Therefore, PVC itself may have greater influence on drug loss than the surface-coating material.

Dexmedetomidine is emerging as a promising sedative-analgesic agent for intensive care unit (ICU) patients [57-60]. Dexmedetomidine has gained attention because classic sedatives including midazolam and propofol have adverse side effects such as prolonged mechanical ventilation and propofol infusion syndrome [61]. Moreover, particularly for delirium which generally comes with deep sedation and is one of the most important issues in the ICU [62-65], dexmedetomidine proved to be more effective in reducing such mental disability than either midazolam or propofol [61, 66]. Accordingly, the pharmacokinetic characteristics of such novel sedative-analgesic agent in ECMO circuit are of interest [55], and the in vitro study thus provides an important contribution to related fields.

Shekar et al. demonstrated instability of meropenem in a blood-primed circuit maintained at 37°C [48], which can be associated with both blood components and temperature. Berthoin et al. evaluated meropenem stability in aqueous solution, and reported that meropenem degradation is dependent on time, temperature, and concentration [67]. Concomitant with these previous studies, meropenem at 0.015 mg/mL used in this study maintained stability over time at room temperature, but degrades at physiological temperature (37°C). Considering such degradation, the initial bolus of meropenem for clinical use should be optimized.

To quantify heparin concentration based on the colorimetric method of Smith et al., a great number of pipetting procedures are necessary, which could

result in technical error. To minimize such error, dispensers (VITLAB GmbH, Grossostheim, Germany) and Eppendorf Multipette M4 (Eppendorf, Hamburg, Germany) were used, which improved reproducibility compared to preliminary experiments. Interestingly discovery the heparin concentration increased with MaG, which was also seen in the preliminary experiments in which experimental procedures were exactly the same but both dispensers and Eppendorf Mutipette (N=3, data not shown) were not used. According to Maquet Inc., Bioline is an albumin-heparin coating in which heparin is covalently bonded to albumin immobilized on the surface. The elevated heparin concentration level within MaG might be associated with the bonding strength between the coating material and the polymethylpentene (PMP) microporous fibers of MaG.

Due to cost and limited amount of materials available from a single circuit, experiment was limited to a small sample size (N=3). Although the larger the sample size the greater the statistical power, Student's t-test facilitates statistical analysis of small sample sizes (N<5), as confirmed by Winter [54].

2.3.5 Conclusion

Drug loss due to individual components of the ECMO circuit was quantified, of which PVC tubing and MaW were critical for dexmedetomidine, while no significant losses were found for meropenem and heparin. Considering that there was no significant difference in drug loss due to MaH and TeH, both of which are made of PC, or to PVC-based tubing, the only difference in which is

the coating material, coating materials may have marginal effects on drug loss. Instead, the materials composing tubing and MaW, PVC and polyurethane fibers, respectively, are likely the primary cause of drug loss, suggesting that material selection is vital in ECMO development. Investigations of chemical responses depending on drug properties to develop an ECMO-specific drug dosing protocol and to resolve the altered pharmacokinetics are important, but use of different materials could also minimize pharmacokinetic changes during ECMO treatment.

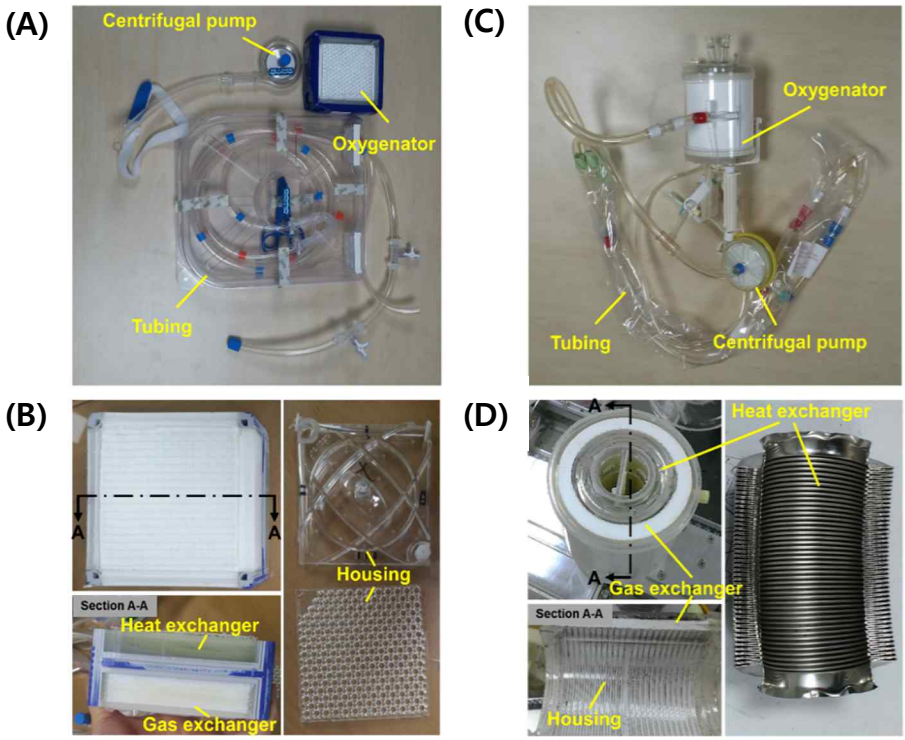

Fig. 2.3.1 Extracorporeal membrane oxygenation (ECMO) circuit components. (A) Maquet ECMO circuit coated with Bioline. (B) Quadrox PLS oxygenator composed of polypropylene microporous fibers for gas exchange, polyurethane fibers for heat exchange, and a polycarbonate housing. (C) Terumo ECMO circuit coated with Xcoating. (D) RX oxyegenator composed of polypropylene microporous fibers for gas exchange, stainless steel heat exchanger and polycarbonate housing.

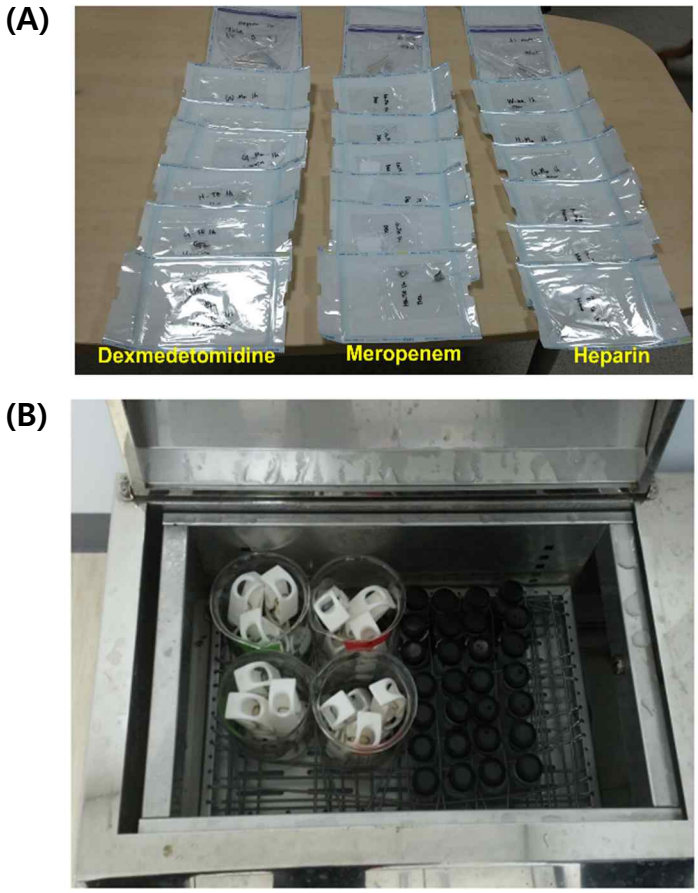

Fig. 2.3.2 Sample preparation and experimental setup. (A) Nine samples from the circuit were considered for each drug and all were sterilized by ethylene oxide (EO) gas. Circuit samples included the gas exchanger, heat exchanger and housing of each oxygenator and three types of tubing (Tygon S-50-HL Medical tubing, Maquet Bioline-coated tubing, and Terumo X-coated tubing). (B) Four sets of circuit samples for 1, 6, 12, and 24 h experiments were moderately agitated in a 37°C water bath for the indicated times**.**

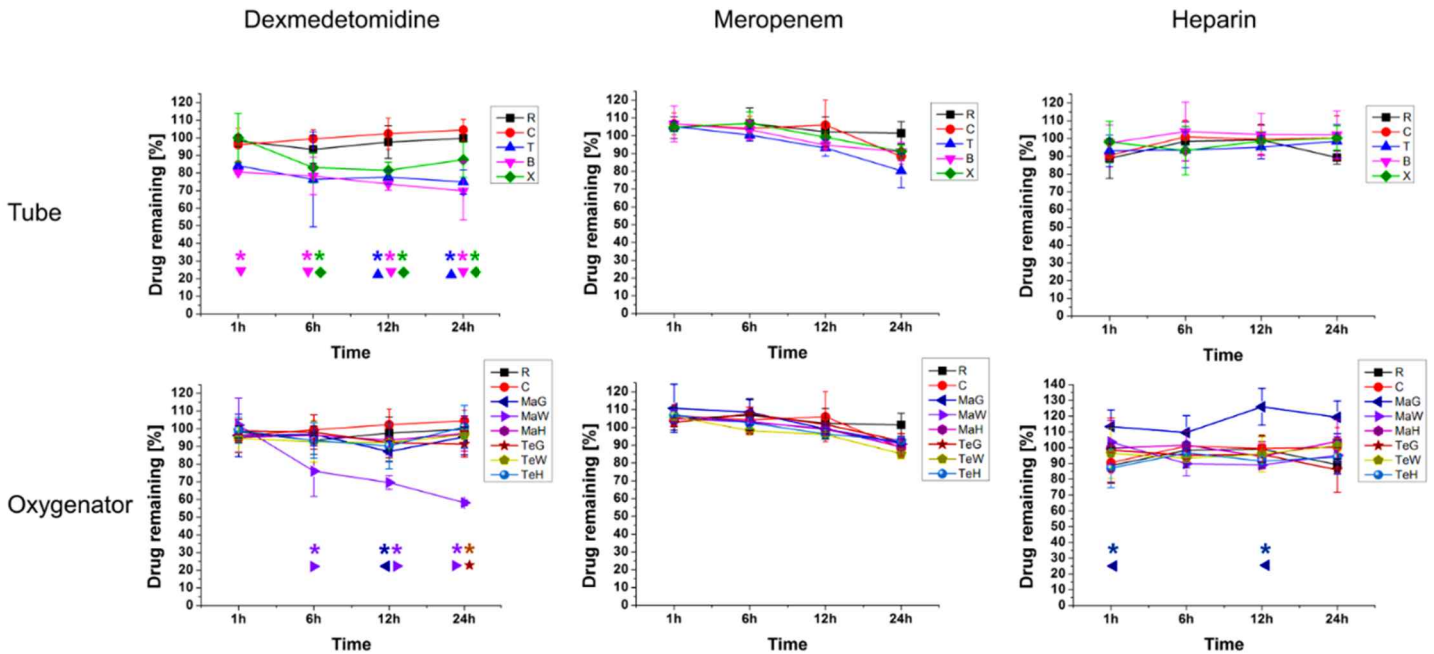

Fig. 2.3.3 Change of drug remaining percentage over time. Upper row shows drug remaining percentages for Tygon (T), Bioline-coated (B), and X-coated (X) tubing at each time point compared to the control group stored at room temperature (R) and 37°C (C). Bottom row shows those for Maquet gas exchanger (MaG), heat exchanger (MaW), housing (MaH), Terumo gas exchanger (TeG), heat exchanger (TeW), and housing (TeH) compared to R and C. Asterisk (*) with material symbol indicates $p<0.05$ compared with C.

Table 2.3.1 Drug remaining percentages at 24 h for dexmedetomidine, meropenem and heparin. B and MaW were common source of significant drug loss for both dexmedetomidine and heparin compared to the control group C. Asterisk (*) indicates $p<0.05$.

Drug remaining at 24 h [%]			
Sample	Dexmedetomidine	Meropenem	Heparin
Control R	99.7 ± 1.3	101.4 ± 6.5	89.2 ± 3.7
Control C	104.4 ± 6.1	88.4 ± 4.4	100.3 ± 12.5
T	75.0 ± 7.0*	80.3 ± 9.6	98.4 ± 9.5
B	69.9 ± 16.5*	91.0 ± 5.1	102.1 ± 13.4
X	87.5 ± 9.9*	91.2 ± 4.3	100.2 ± 6.8
MaG	95.5 ± 10.3	91.4 ± 1.8	119.3 ± 10.3
MaW	58.2 ± 1.7*	90.7 ± 3.5	95.2 ± 11.7
MaH	97.3 ± 10.0	89.0 ± 1.5	104.0 ± 13.6
TeG	91.4 ± 7.3*	92.2 ± 4.3	85.9 ± 14.0
TeW	96.6 ± 2.8	85.2 ± 2.8	101.4 ± 4.6
TeH	101.1 ± 12.1	92.6 ± 2.1	94.0 ± 10.8

Chapter 3.

Micro-scale centrifugal-fluidic system for biomedical application

3.1 A numerical study of the Coriolis effect in centrifugal microfluidics with different channel arrangements [68]

The Coriolis force has been of great interest to control the transversal flow that is critical for mixing or switching fluids in centrifugal microfluidics. Therefore, the variation in the Coriolis effect has been extensively investigated by varying the rotational speeds and the cross-sectional geometry of microchannels.

However, the subject of such investigations has been limited to radially positioned microchannels even though channels can lie everywhere on the rotating platform with different arrangements. In this study, numerical methods were used to investigate the Coriolis effect resulting from the angular alignment (AA) and radial displacement (RD) of rotating microchannels. The analysis focuses on determining the contribution that different channel arrangements have in the deviation of parabolic velocity profiles, which is generally produced by the effective Coriolis force. The simulation result showed that the flow can deviate even at a low rotational speed, where the Coriolis force is negligible, with an AA of up to 33% which is a sufficient amount for flow switching. Once the rotational speed reaches to the critical RPM, the flow deviates by an effective Coriolis force, but the deviation systematically varies with AA or RD. As the Coriolis force becomes more dominant with a high rotational speed, the deviation reaches a saturation point while flow rate is regulated by AA or RD, enabling the flow rate to remain low even at very high RPM, without reducing the deviation. The variation in the Coriolis effect due to the different channel arrangements investigated in this study is believed to provide an essential basis to design and develop centrifugal microfluidic systems.

3.1.1 Introduction

Over the past few decades, significant advances have been made for Lab-on-a-CD systems, which are a representative model of centrifugal microfluidics devices. Such technologies provide a wide range of capabilities for biological and chemical analysis, particularly in biomedical applications such as blood

analysis or high-throughput immunoassays. These devices are thus emerging as clinical laboratory tools with a high potential to replace conventional time-consuming and labor-intensive laboratory methods [18].

One of the major advantages of using centrifugal microfluidic systems is that they achieve compactness by replacing an external pumping device with an embedded rotor that generates rotational forces in order to produce a pressure-driven like flow or other fluidic functionalities with the appropriate channel design, e.g., mixing, valving, metering, sample splitting, or even multiple integrated functions [69]. However, the rotational forces spatially vary depending on the rotational speed, so it is necessary to have a solid understanding of the fluidic behavior under a wide range of rotational forces along the channel in order to achieve a successful implementation.

Three forces govern the fluidic behaviors in centrifugal microfluidics: the centrifugal force (f_ω), the Euler force (f_E), and the Coriolis force (f_C) (Fig. 1.1.1). At a constant rotational speed, the fluid flow is determined by the interaction between the centrifugal force and the Coriolis force. Once the fluid confined in the rotating channels begins to move as a result of the centrifugal force, the Coriolis force begins to have an effect, depending on the direction and speed of the flow. When the Coriolis force is dominant over the centrifugal force, the velocity profile of the typical laminar flow, which is symmetrically parabolic, exhibits a significant change by deviating into one of the sidewalls.

Such a deviation in the flow can have an important role in the microfluidic device since it induces an effective fluidic switch [70], bifurcation [71] or convective mixing [72-75], all of which were originally limited due to the

inherent features of laminar flow through microchannels [76]. Previous studies have attempted to implement active control by integrating magnetic beads with expensive electromagnets [77-79] or microvalves (e.g., electrokinetic valves) [80] to provide microfluidic mixing and routing, respectively. However, such techniques introduce severe complexities into the system, and it is therefore necessary to minimize the number of active components that are in use. A recent study showed that it is important to consider inertial forces even when active controls are used since this creates synergetic effects and further improves the performance of the system [19]. Therefore, it is essential to have a thorough understanding of the physical phenomena that are manifested as a result of the interaction of diverse rotational forces in order to successfully implement the desired fluidic functionality while maximizing passive control in the centrifugal microfluidic systems.

Accordingly, several numerical and experimental studies have been carried out to regulate the centrifugal and Coriolis forces by using various combinations of rotational speed and geometric structures [70, 71, 74, 75, 81, 82]. Recently, a critical rotational Reynolds number was proposed in order to generate the most effective flow deviation via a Coriolis force by analyzing the different rotational speeds and different microchannel hydraulic diameters [83]. However, all of these prior studies have been limited to investigating only a single radially aligned microchannel (radial model) (Fig. 1.1.1), even though channels can lie everywhere on the rotating platform with different arrangements.

Here, the effects that the angular rotation and radial displacement of

rotating microchannels can have on the fluid dynamics of centrifugal microfluidics were investigated. The hypothesis is that different channel arrangements, in addition to the rotational speed or the size and shape of the channel cross-section, influence the rotational forces and, therefore, the fluidic behavior. As a result of this study, the decomposition of the centrifugal force produced according to different arrangements plays an important role in flow routing at a low rotational speed and in maintaining or assisting flow deviation at an intermediate rotational speed. The flow deviation is eventually saturated at a high rotational speed even though the Coriolis force becomes more dominant while the volumetric flow rates change systematically with the different channel arrangements. The new findings of this study are believed to provide the essential basis of the design principles for centrifugal microfluidics in order to realize the desired fluidic functionalities, including mixing and routing, by achieving more convenient liquid handling and better use of the limited space that is available in centrifugal microfluidics platforms.

3.1.2 Model problem

The effects of the channel arrangements on the centrifugal microfluidics were investigated by using two types of non-radial models: angular alignment (AA) and radial displacement (RD). The schematics for these two configurations are shown in Fig. 3.1.1. For the AA configurations, a three-dimensional (3D) rectangular channel on top of a circular disk is aligned at seven different angles (0°, 15°, 30°, 45°, 60°, 75°, 90°) relative to the radial model, which is radially

aligned with the inlet located at a radial distance of 20 mm from the center of the disk. For the RD configurations, a 3D microchannel with a 90° angular alignment moved radially outward at seven different displacements (0, 2, 4, 6, 8, 10, 12 mm). Both models were investigated with ten different levels of rotational speed, at intervals of 400 RPM, from 200 to 4200 RPM, both in the clockwise (CW) and in the counter clockwise (CCW) directions. A previous study shows that a microchannel with a square cross-section generated a maximum deviation in the velocity profile [83], and accordingly, the models were designed to have a height (h) and width (w) of 200 μm with a length (L) of 20 mm.

For each model, the different channel arrangements decompose the centrifugal force (f_ω) into one force along the channel and another parallel to the Coriolis force (f_C) that is perpendicular to the channel length. Assuming that the decomposition of the centrifugal force may contribute to the deviation in the velocity profile, the force relationship that represents the ratio between the force acting along the channel and the force acting perpendicular to the channel was considered for the model problems (Fig. 3.1.2).

Radial model

Under a constant rotational speed, the force relationship between the centrifugal force (f_ω) and the Coriolis force (f_C) governs the fluid behavior in a centrifugal microfluidic system. f_ω and f_C are:

$$\vec{f}_\omega = \rho\omega^2 \vec{d}(r) \tag{3.1.1}$$

$$\vec{f}_c = -2\rho\vec{\omega} \times \vec{u} \tag{3.1.2}$$

where ρ is the fluid density, ω is the rotational speed, r represents the coordinates along the center line of the channel with the origin at the inlet, $d(r)$ is the distance from the point r to the rotating axis, and $\vec{u}$ is the fluid velocity. When u_{max} derived from the balance of the centrifugal and viscous forces (Eq. (3.1.3)) is applied to estimate the Coriolis force, the force relationship between f_C and f_ω becomes that in Eq. (3.1.4).

$$u_{\max} = \frac{\rho\omega^2 d(r)}{8\mu}\Delta w^2 \tag{3.1.3}$$

$$k_{fluid} = \frac{\left|\vec{f}_C\right|}{\left|\vec{f}_\omega\right|} = \frac{\rho\Delta w^2\omega}{4\mu} \tag{3.1.4}$$

where μ is the fluid viscosity and Δw is the width of the channel. According to this relationship, the Coriolis force prevails over the centrifugal force when ω becomes greater than 1000 RPM with the liquid properties of water, which is the working fluid considered in this study [70].

Non-radial model

The force relationship for the non-radial model needs to be modified from that of the radial model since the non-radial model entails the decomposition of the centrifugal force [84] (Fig. 3.1.2). Channel arrangements can be defined by combinations of angular alignment (θ) and radial distance (x), which in turn

determines the distance variable *d(r)* that varies along the channel from inlet to outlet (Fig. 3.1.3). All variations of *d(r)* should affect changes in the velocity profiles. Accordingly, the non-radial model was categorized into AA and RD configurations, which satisfies (θ, *x*)=(θ, *0*) and (θ, *x*)=(*90°*, *x*) respectively, in order to analyze the flow features more systematically. For the non-radial model, u_{max} and *d(r)* is modified by different channel arrangements as:

$$u_{\max} = \frac{\rho\omega^2 d(r)\cos(\theta-\alpha(r))}{8\mu}\Delta w^2 \tag{3.1.5}$$

$$d(r)=\frac{20+r\cos\theta+x}{\cos\alpha(r)} \tag{3.1.6}$$

$$\alpha(r) = \tan^{-1}\left(\frac{r\sin\theta}{20+r\cos\theta+x}\right) \tag{3.1.7}$$

where θ is the channel alignment angle, *x* is the radial displacement of the channel, *r* represents the coordinates along the center line of the channel with the origin at the inlet, $\alpha(r)$ is the angle between f_ω at the *r*-coordinate and the horizontal line, and $d(r)$ is the distance from point *r* to the rotating axis. By applying this modified u_{max} to estimate the Coriolis force, the force relationship that represents the ratio between the force acting along the channel and the force acting perpendicular to the channel becomes:

$$\frac{\left|\vec{F}_{perp}\right|}{\left|\vec{F}_{axial}\right|} = \frac{\left|\vec{f}_{\omega,perp}\pm\vec{f}_C\right|}{\left|\vec{f}_{\omega,long}\right|} = \frac{\rho\omega^2 d(r)\sin(\theta-\alpha(r))\pm 2\rho\omega u_{max}}{\rho\omega^2 d(r)\cos(\theta-\alpha(r))}$$

$$=\tan\left(\theta-\alpha(r)\right)\pm\frac{\rho\Delta w^2\omega}{4\mu} \tag{3.1.8}$$

where the Coriolis force ($\vec{F}_C$) is either added to or subtracted from $f_{\omega,\ perp}$, depending on the direction of the rotation (Fig. 3.1.2). Here, $f_{\omega,\ perp}$ is the decomposition of f_ω acting perpendicular to the channel, and $f_{\omega,\ long}$ is the decomposition of f_ω acting parallel to the channel. $\frac{\rho\Delta w^2\omega}{4\mu}$ is defined as k_{fluid} in Eq. (3.1.4), so the force relationship for AA and RD configurations can be further reduced to Eq. (3.1.9) and Eq. (3.1.10) by satisfying (θ, x)=(θ, *0*) and (θ, x)=(*90°*, x) respectively. Note that Eq. (3.1.8) becomes the force relationship for the radial model, k_{fluid}, with (θ, x) = (*0, 0*).

$$\frac{\left|\vec{F}_{perp}\right|}{\left|\vec{F}_{long}\right|} = k_{AA} \pm k_{fluid} \tag{3.1.9}$$

$$\frac{\left|\vec{F}_{perp}\right|}{\left|\vec{F}_{long}\right|} = k_{RD} \pm k_{fluid} \tag{3.1.10}$$

where $k_{AA} = \tan\left(\theta - \alpha(r)\right)$, with $\alpha(r) = \tan^{-1}\left(\frac{r\sin\theta}{20+r\cos\theta}\right)$, and $k_{RD} = \tan\left(90^\circ - \alpha(r)\right)$, with $\alpha(r) = \tan^{-1}\left(\frac{r}{20+x}\right)$ (Fig. 3.1.3). While k_{fluid} is a constant factor, as it remains constant regardless of either the alignment angle(θ) or the radial distance(x), k_{AA} and k_{RD} are variable factors for each configuration since the range of the values varies along the channel length according to the alignment angle and the radial displacement, respectively. The values for k_{fluid}, k_{AA}, and k_{RD} are described in Table 3.1.1.

3.1.3 Analytical solution

The Navier-Stokes equations for fluid mechanics in rotating microchannels with different angular or radial arrangements are analytically solved by making the following assumptions of the fluid to simplify the problem: 1. incompressible; 2. Newtonian fluid; 3. fully developed; 4. laminar flow; and 5. steady state. Based on Fig. 3.1.3, the momentum equation for the *r*-direction, which is the flow direction along the channel length, has been established. With the following boundary conditions, the momentum equation for the *r*-direction is reduced to Eq. (3.1.11):

$$\begin{aligned} &\frac{\partial^2 u}{\partial x^2} + \frac{\partial^2 u}{\partial z^2} = -\frac{1}{\mu}\left(-\frac{dp}{dr} + F_b\right) \\ &u(x=0,z)=u(x=w,z)=0 \\ &u(x, z = 0) = u(x, z = h) = 0 \end{aligned} \tag{3.1.11}$$

where u is the velocity vector along the *r*-direction, and p is the static pressure as a function of r if the centrifugal force was considered only as the body force, F_b, such that

$$F_b = \rho\omega^2 d(r) \tag{3.1.12}$$

where *d(r)* is the radial distance of the points along the channel from the rotating axis (Fig. 3.1.3). Eq. (3.1.11) can then be easily solved based on the eigenvalue concept ($\Delta u = -\lambda u = f$) by expressing the left and right side of Eq. (3.1.11) as the following series of eigenvalues and eigenfunctions.

$$u(x,z) = \frac{\partial^2 u}{\partial x^2} + \frac{\partial^2 u}{\partial z^2} = \sum_{m=1}^{\infty} . \sum_{n=1}^{\infty} U_{n,m} \Phi_{n,m} \tag{3.1.13}$$

$$f(x,z) = -\frac{1}{\mu}\left(-\frac{dp}{dr} + F_b\right) = \sum_{m=1}^{\infty} . \sum_{n=1}^{\infty} F_{n,m} \Phi_{n,m} \tag{3.1.14}$$

where $\Phi_{n,m} = \sin\frac{n\pi x}{w}\sin\frac{m\pi z}{h}$ is an eigenfunction and $U_{n,m}$ and $F_{n,m}$ are eigenvalues. Solving for $F_{n,m}$ in MATLAB (Mathworks, Inc., Natick, MA),

$$F_{n,m} = \frac{4}{wh} \int_0^h . \int_0^w f(x,z) \sin\frac{n\pi x}{w} \sin\frac{m\pi z}{h}\, dxdz \tag{3.1.15}$$

$$F_{m,n} = \frac{16\frac{dp}{dr}\left(\sin\frac{\pi m}{2}\right)^2\left(\sin\frac{\pi n}{2}\right)^2 - 16\rho\omega^2\left(\sin\frac{\pi m}{2}\right)^2\left(\sin\frac{\pi n}{2}\right)^2 d(r)}{\mu mn\pi^2} \tag{3.1.16}$$

Since $F_{n,m} = 0$ with even numbers for m and n, $F_{n,m}$ is reduced to

$$F_{m,n} = \frac{\frac{16}{\mu}\left(\frac{dp}{dr} - \rho\omega^2 d(r)\right)}{(2m-1)(2n-1)\pi^2} \tag{3.1.17}$$

The $U_{m,n} = -\frac{F_{m,n}}{\lambda_{m,n}}$ derived from the eigenvalue concept is applied, and thus $U_{n,m}$ becomes

$$U_{m,n} = \frac{\frac{16}{\pi^2\mu}\left(-\frac{dp}{dr} + \rho\omega^2 d(r)\right)}{(2m-1)(2n-1)\lambda_{m,n}} \tag{3.1.18}$$

where $\lambda_{m,n} = \left(\frac{(2n-1)\pi}{w}\right)^2 + \left(\frac{(2m-1)\pi}{h}\right)^2$.

As a result, $u(x, z)$ and u_{avg} become

$$u\left(x,z\right) = \frac{16}{\pi^2\mu}\left(-\frac{dp}{dr}+\rho\omega^2 d(r)\right)\sum_{m=1}^{\infty}.\sum_{n=1}^{\infty}\frac{1}{(2m-1)(2n-1)\lambda_{m,n}} \sin\frac{\sigma_m x}{w}\sin\frac{\sigma_n z}{h} \tag{3.1.19}$$

where $\sigma_m = (2m - 1)\pi$, $\sigma_n = (2n - 1)\pi$, and

$$u_{avg} = \frac{1}{wh}\int_0^h.\int_0^w u(x,z)dxdz = \frac{64}{\pi^4\mu}\left(-\frac{dp}{dr}+\rho\omega^2 d(r)\right)\sum_{m=1}^{\infty}.\sum_{n=1}^{\infty}\frac{1}{(2m-1)^2(2n-1)^2\lambda_{m,n}} \tag{3.1.20}$$

A comparison with the analytical solution described by Roy et al. [83] indicates that the analytical solution provides a more general form of the velocity analysis for a rotating microchannel with the parameter *d(r)*, with applicability for the non-radial model (e.g. AA and RD configurations) as well as the radial model.

3.1.4 Numerical solution

The modeling for the AA and RD configurations as well as the three-dimensional (3D) computational fluid dynamics (CFD) was performed by using the laminar flow interface provided in the Microfluidics Module of COMSOL Multiphysics 4.4 (COMSOL Inc., Palo Alto, CA). Centrifugal and Coriolis forces were employed explicitly as body forces.

Simulation was first performed by following the instructions in the

qualified example provided by the COMSOL group (https://www.comsol.com/model/rotating-channel-14033). The only difference was the setting for the inlet boundary condition, for which the instruction specifies applying zero pressure. However, the COMSOL group strongly emphasized that this boundary condition at the inlet is unphysical even though it was commonly used for similar simulations of rotating microchannels by other groups including Glatzel et al. [85]. For this reason, instead of zero pressure, average velocities for the inlet boundary conditions was applied by following Eq. (3.1.21), which is characterized experimentally and is proven to have great correlations with the experimental results [86]. Moreover, considering that the radial model is exactly the same as the square microchannel used by Roy et al. [83] as one of the cases for their analysis, the simulation results from the radial model with those for their square microchannel were compared in order to confirm the numerical simulations performed in this study.

Grid independence test

In this study, a uniform grid is considered in the x, z, and r directions, and a grid independence study was performed with a radial model at 4200 RPM. The mesh was refined until the analytical parameters, maximum velocity magnitude (u_{max}), volumetric flow rate (Q), and flow deviation percentage (DP) became independent of the mesh. Here, DP is defined as the percentage of the maximum velocity displacement from the center to the sidewall in the direction of the channel width (Fig. 3.1.4) to quantitatively measure the change in the parabolic velocity profile from the symmetric to the asymmetric shape. The mesh from

having 18,900 degrees of freedom (DOF) to having 980,100 DOF were examined by computing the percent differences (% diff.) among the analytical parameters (DP, u_{max}, and Q) that results from two successive grid systems. In addition, the velocity profiles at the outlet in both the x and z directions for each grid system were compared by computing the mean differences of the velocity at each grid point in order to ensure grid independency (Table 3.1.2). For comparison, the values that have been calculated at each grid point were connected via cubic spline interpolation in order to provide solutions for the same coordinates in different grid systems. As the number of grid points increases, the percent difference among the analytical parameters for the 38x38x100, 40x40x100, 42x42x120, and 44x44x120 grid systems were all within acceptable ranges (below 0.5%) and the mean differences of the velocity profiles in either the x and z directions were also very small (Table 3.1.2 and Fig. 3.1.5). In particular, the grid system with a size of 40x40x100 further reduced the percent difference for both DP and u_{max} below 0.05%. The velocity profiles in both the x and z directions in the grid system with a size of 40x40x100 also had a high similarity to those of further refined grid systems (42x42x120 and 44x44x120) (Fig. 3.1.5). Therefore, considering the computational efficiency, the grid system with a size of 40x40x100 was finally chosen to use in all subsequent simulations, including for both AA and RD configurations.

Problem set-up

The microchannel was assumed to be connected to a large inlet reservoir at one

end and to a large waste reservoir at the other (Fig. 3.1.6). The average velocity, as given by Duffy et al., depends on the properties of the liquid, the size, location, the configuration of the channel, and the rate of rotation [86][Eq. (3.1.21)].

$$U_{avg} = \frac{d_H^2 \rho \omega^2 \bar{r} \Delta r}{32 \mu L} \tag{3.1.21}$$

where d_H is the hydraulic diameter of the channel, L is the length of the channel, ω is the rotational speed, $\bar{r}$ is the average distance of the liquid in the channel from the center of the disk, and Δr is the radial extent of the fluid that is subjected to the centrifugal force. $\bar{r}$ and Δr are defined with geometric parameters r_0, r_1, and H, as shown in Fig. 3.1.6, such that $\bar{r} = (r_0 + r_1 - H) / 2$ and $\Delta r = (r_1 - (r_0 - H)$, where r_0 and r_1 are the inner and outer radii of the flowing fluid, respectively, and H is the head of the liquid in the inlet reservoir. Assuming that the inlet reservoir is continuously being filled with water during rotation, H is set to 0.01 m in the numerical simulations.

Using Eq. (3.1.9), which is derived considering the centrifugal force only, the average velocities were calculated for all numerical models considered in this study and were applied to the inlet boundary conditions assuming that the Coriolis force is negligible at the inlet. The reason lies in the fact that the effective Coriolis force is generated only after the flow moves with an effective velocity and the inlet is where the flow just starts to move by centrifugal force that acts on it. For the outlet and the side walls, the open boundary condition, which allows the fluid to both enter and leave the domain, and the no-slip boundary condition were respectively given.

In this study, steady-state simulations were performed with the given boundary conditions. Water was considered as the working fluid, and it was considered to have a density (ρ) of 1000 kg/m^3 and a viscosity (μ) of 0.001 Pa·s. The flow behavior for each model was examined by extracting data from the outlet, and the analyses were performed according to three parameters, the flow deviation percentage (DP), the maximum velocity magnitude (u_{max}), and the volumetric flow rate (Q).

3.1.5 Results

In the radial model, the Coriolis force acts on the fluid in a clearly visible manner. The parabolic velocity profile with a fully developed laminar flow starts to deviate toward the sidewall in the direction of the Coriolis force, and the deviation in the velocity profile, which is defined as the deviation percentage (DP), grows as the rotational speed ω increases. Therefore, in the radial model, DP increases as the constant factor k_{fluid} increases, which is proportionally related to ω [Eq. (3.1.3)] by representing the dominance levels of the Coriolis force relative to the centrifugal force. However, the DP is eventually saturated at a high rotational speed, irrespective of the further increase in k_{fluid}, which also can be seen in the results provided by Roy et al. [83]. In this previous study, the effects of the Coriolis force under different aspect ratios (AR) for the cross-sectional area of the channel were investigated, including a channel with AR = 1 identical to the radial model. The resulting velocity profile with AR = 1 in this previous study is also very similar to ours by displaying the saturation of the flow deviation at a high rotational speed.

However, a comparison of the overall results reveals that Roy et al. achieved a DP that significantly changes according to differences in the aspect ratio, even at a high rotational speed, while the results show that DP is rather saturated and is maintained with different channel arrangements (non-radial model) at a high rotational speed while the flow rates, on the other hand, systematically change according to either AA or RD.

For the non-radial model, variable factors (k_{AA} for the AA configuration and k_{RD} for the RD configuration) are produced by the decomposition of the centrifugal force in addition to k_{fluid}. k_{fluid} is either added to or is subtracted from these variable factors according to the direction of the rotation (CW or CCW) to represent the dominance levels of the perpendicular force relative to the longitudinal force. For each configuration, the influence of each variable factor on DP is different for different domains of ω, whether or not an effective Coriolis force exists (Fig. 3.1.7). As the rotational speed reaches the critical RPM, at which $k_{fluid} \sim 1$ (1000 RPM), the trend for the DP is reversed and is eventually saturated at a high rotational speed ($k_{fluid} >> 1$), irrespective of further changes in both k_{fluid} and the variable factors. The trend of the DP saturation is displayed by using a variation of deviation (VD) graph (Fig. 3.1.8), which was produced from a linear regression of the change in the deviation. Therefore, the slope of each fitted line indicates the amount of variation in the DP that is caused by the AA or RD configurations at a given rotational speed (Fig. 3.1.9).

For the AA configuration, DP grows with a k_{AA} increment at a low rotational speed ($k_{fluid} << 1$) regardless of whether k_{fluid} is added to or is

subtracted from it (Fig. 3.1.10 and Fig. 3.1.11), meaning that k_{AA} leads the flow deviation. Therefore, DP and k_{AA} are proportionally related at a low rotational speed, creating positive VDs for both the CW and the CCW rotation (Fig. 3.1.8). However, once the Coriolis force becomes dominant ($k_{fluid} > 1$), k_{AA} becomes an auxiliary component in the flow deviation. At the critical RPM ($k_{fluid} \sim 1$), DP is no more proportionally related to k_{AA}, and the trend is reversed as VD becomes negative, meaning that k_{fluid} starts to lead the flow deviation. However, the CCW and CW rotations exhibit different VDs, meaning that k_{AA} still has an effect on DP. Although the k_{fluid} that is added to k_{AA} by the CCW rotation cannot further increase DP, the k_{fluid} that is subtracted from k_{AA} (Fig. 3.1.11) by the CW rotation further reduces the flow deviation (DP), which may indicate that k_{AA} in the CCW rotation becomes responsible for compensating for the attenuated Coriolis force caused by the reduction in flow as AA increases. At a high rotational speed ($k_{fluid} >> 1$), k_{AA} becomes negligible and DP is saturated in the direction of the Coriolis force for both the CCW and CW rotations, meaning that k_{fluid} entirely leads the flow deviation. Meanwhile, the volumetric flow rates can be effectively regulated with variations in AA, ranging from 9.96 mL/min to 21.3 mL/min at 4200 RPM, for example (Fig. 3.1.12). However, there is no change in DP.

With respect to the RD configuration, the DP generated at a low rotational speed ($k_{fluid} << 1$) by an angular alignment of 90° with respect to the radial direction drops as k_{RD} increases, even when k_{RD} is added to k_{fluid} in the CCW rotation (Fig. 3.1.7B), creating negative VDs (Fig. 3.1.8). This implies that the variable factor cannot cause an effect in the radial displacement that increases

the flow rate along the channel. The initial DP produced by $k_{AA=90}$ at a low rotational speed is greater for the CCW rotation than for the CW rotation due to the different interactions, either addition or subtraction, between the constant factor k_{fluid} and the variable factor. However, the effects of k_{RD} in reducing the initial DP are almost the same as the VDs for the CCW rotation, which overlap well with those for the CW rotation at a low rotational speed. Once the Coriolis force becomes dominant ($k_{fluid} > 1$), k_{RD} becomes responsible for assisting the increases in the deviation, and therefore, DP becomes saturated even faster (as VD approaches to 0) with the CCW rotation where k_{RD} and k_{fluid} act in the same direction. At the initial stage of $k_{fluid} > 1$ section, VD grows until k_{fluid} becomes greater than k_{RD}. VD is particularly larger with CW rotation where k_{fluid} and k_{RD} act in the opposite direction, meaning that DP changes in a relatively systematic way according to the effective $k_{RD.}$ that acts opposite to k_{fluid}. Once k_{fluid} surpasses k_{RD}, the contribution of k_{RD} becomes trivial, and VD starts to decrease and approaches zero as DP becomes saturated at a high rotational speed with a dominance effects of the Coriolis force ($k_{fluid} >> 1$).

For both configurations, the VD crosses zero (reversal of the DP trend) around the critical rotational speed of 1000 RPM ($k_{fluid} \sim 1$, Fig. 3.1.8) with an effective Coriolis force generated as expected from Eq. (3.1.4). However, the DP trend is not completely reversed at this critical RPM with the CCW rotation while an apparent reversal is observed with the CW rotation, meaning that k_{fluid} and the variable factors (k_{AA} or k_{RD}) coexist by providing almost even contributions to DP at this critical RPM. For all ranges of rotational speeds, the CW rotation exhibits larger VDs than the CCW rotation due to the opposing

action, meaning that DP can be systematically controlled by an effective variable factors that act in the opposite direction to $k_{fluid.}$ Although the CCW and the CW rotation have such a different DP trend, there is no difference in the flow rates, which determine the Coriolis force according to Eq. (3.1.2), meaning that different channel arrangements certainly have an effect on the DP in centrifugal microfluidics.

3.1.6 Discussion

The results of the simulation indicate that the deviation in the flow, DP, is relatively unchanged with respect to the channel arrangements particularly when the constant factor (k_{fluid}) and the variable factors (k_{AA} or k_{RD}) act in the same direction with an effective Coriolis force (Fig. 3.1.7 and Fig. 3.1.13) while the volumetric flow rates can be effectively regulated with respect to the channel arrangements (Fig. 3.1.9). Such effects become more obvious at a high rotational speed. For example, the angular channel alignment allows a systematic reduction in the flow rate of more than 50% (i.e., from 9.96 mL/min to 21.3 mL/min at 4200 RPM) with almost no change in the DP at the high rotational speed (Fig. 3.1.14 and Fig. 3.1.15). This may lead to a technique where the residence time of the fluid is manipulated by determining the flow rate. The fluid residence time is known to provide a direct impact on the reaction process [87], and therefore, the maintenance of DP for an extended time by tilting the channel should allow for more efficient mixing or chemical reactions.

Instead of regulating the flow rate, the length of the channel can be

regulated in order to manipulate the residence time. Extending the channel length is another key impact parameters to prolong the residence time not only to ensure efficient mixing but also to achieve a complete flip or switch in the flow by the Coriolis force that is generated [74] in centrifugal microfluidic system. However, it requires additional spaces. Here, aligning the channel other than in a radial direction could provide a solution to reserve spaces, even with an extended channel length. Therefore, the non-radial alignment channel with an extended length could bring synergetic effects for the Coriolis- induced flow phenomena, including patterning, flipping, and multilamination [74, 75, 88] by saving limited spaces available on the rotating platform.

In previous studies, multilamination [75] and flow patterning [74] were described in order to accelerate mixing. Multilamination is based on a split-flip-and-recombine scheme, and flow patterning reshapes the flow by inducing a larger Coriolis force with a higher rotational speed. However, the results of the simulation indicate that more consistent multilamination and patterning could be expected all at once under the same rotational speeds by making good use of the principles described here. For example, with an intermediate CW rotation, where k_{fluid} and the variable factors coexist, DP changes in a relatively systematic way where an AA = 90° channel would provide the minimum DP to achieve a more uniform flow division at the initial branching point. Then, the following AA < 90° channel would increase the DP, prompting flow flipping in the central channel. The flow may be again split or recombined with a channel that is further revolved (AA << 90°) in order for the patterning the flow by maximizing the DP to achieve efficient mixing.

However, if the experimenter tilts the channel only to save the space with no interest in extending the residence time, the weakened DP may become an issue especially when the operating RPM is at an intermediate rotational speed. In this case, RD can provide a solution without frustrating the purpose of saving space. Based on the simulation results, the radial displacement of 12mm, an amount that is only about half the length of the channel, results in slightly larger DP (<2.6%) with CCW rotation under the effective Coriolis force (>1000 RPM) compared to the DP from the radial model (Fig. 3.1.7). This suggests that one may be able to fully compensate DP weakened by tilting with RD that is much less than the channel length.

Another discovery is that different channel arrangements result in a DP that becomes nonzero at the outlet, even at low rotational speeds, by following the variable factors. In a radial model, the symmetrically parabolic flow profile continues toward the outlet, with DP = 0 at low rotational speeds, when the Coriolis force is negligible. However, as the flow reaches the outlet in a non-radial model, it deviates at its final destination, resulting in a nonzero DP. Particularly for the AA configuration, DP is maximized with AA = 90° up to 33%, and such configuration might be effectively used to provide flow routing, such as the flow switching described by Brenner et al. [70].

Note that there is a strange kink with the DP change at the critical RPM (1000 RPM in the present study) (Fig. 3.1.7-3.1.9) at which an effective Coriolis force is generated as expected from Eq. (3.1.4). The k_{fluid} defined in Eq. (3.1.4) is the ratio of the Coriolis force to the centrifugal force exerted on the fluid flowing through the radially positioned channel, representing the

dominance levels of these two forces with respect to one another. With the liquid properties of water and the channel geometry, 1000 RPM turned out to be the transition spot where the ratio starts to exceed 1. However, in non-radial models, additional factors (k_{AA} for AA configuration and k_{RD} for RD configuration) are involved in accord with k_{fluid} to represent the ratio of the perpendicular force to the parallel force exerted on the fluid flowing through the non-radially positioned channel due to decomposition of the centrifugal force by different channel arrangements. In the ranges of rotational speed from low to high, k_{AA} and k_{RD} create odd behaviors during the transition period around the critical RPM, while providing relatively systematic effects with k_{fluid} in other ranges of rotational speed (Fig.3.1.7-3.1.9). Particularly, the obvious difference in DP changes found at the critical RPM between CCW rotation and CW rotation indicates that channel arrangement certainly has the effect of either increasing or decreasing DP along with the Coriolis force. Therefore, considering this distinctive feature during the transition period, special attention on the rotational direction or on the channel design might be required when the experimenter tries to tilt the channel, for example, to save space with the operating rotational speed of the critical RPM. For example, if the experimenter purposed to flow two different fluids by minimizing the interaction between the two fluids to create two distinct layers, CW rather than CCW rotation might be desirable since DP can be reduced to zero with CW rotation at the critical RPM within the AA=90° microchannel. On the other hand, DP remains relatively the same around 20% for CCW rotation at the critical RPM even within the AA=90° microchannel. As another example, considering that the difference in VD

between CCW and CW rotation reaches its maximum value at the critical RPM (Fig. 3.1.8), if the experimenter designs a channel network that is symmetrically branched with respect to the radial direction with different branching angles, the critical RPM will prompt maximized difference in flow between the two sets of branched channels since one side of the flow would move with the flow characterization of CCW rotation and the other with that of CW rotation while the platform rotates in either direction.

3.1.7 Summary and Conclusion

It is very important to have a solid understanding of the fluidic behavior of various microchannel designs under a wide range of rotational forces to successfully implement centrifugal microfluidics in biological and chemical research that requires sample manipulation. However, previous studies have been limited to radially positioned microchannels in order to study the transversal flow that causes a flow deviation in the centrifugal microfluidics by varying either the rotational speed or the size and shape of the cross-section of the channel [70, 71, 74, 75, 81, 82]. Moreover, such studies have shown that the rotational speed is the primary factor that induces an effective transversal flow or a Coriolis force, which, however, would also dramatically increase the flow velocity along the channel, preventing independent control of both parameters.

In this study, the influence of channel arrangements at various angles relative to the radial direction (AA configuration) or at radially outward displacements (RD configuration) on the transversal flow that is generated was

explored. An ability either to regulate the flow deviation in a relatively systematic way at a low and an intermediate rotational speed with the opposite action between the Coriolis force and the decomposition of the centrifugal force or to regulate the flow velocity while maintaining the flow deviation by changing the relative position of the microchannel in the rotating platform, especially at a high rotational speed was demonstrated. The effect that the variable factors (k_{AA} or k_{RD}) had was examined in terms of the results from the decomposition of the centrifugal force for each configuration to the flow deviation and volumetric flow rate. At a low rotational speed, when the variable factors dominate k_{fluid}, the flow deviates to up to 33% at the outlet by following the variable factors, which is the amount that should be useful for flow routing. Once k_{fluid} is dominant and the Coriolis force becomes effective, the entire flow begins to deviate in the direction of the Coriolis force. Here, the deviation in the flow, DP, is relatively unchanged when the constant factor (k_{fluid}) and the variable factors (k_{AA} or k_{RD}) act in the same direction, but DP changes in a relatively systematic way by the channel arrangements when the constant factor and the variable factors act in the opposite direction. Eventually, the deviation becomes completely saturated at a high rotational speed for both the CCW and CW rotation while the volumetric flow rate changes systematically with each configuration. In particular, the ability to manipulate the residence time while maintaining the flow deviation is believed to be critical for a wider variety of applications for centrifugal microfluidics, such as for chemical reactions where the residence time is known to provide a direct impact on the reaction process [87, 88]. In addition, all of the volumetric flow rates that were calculated from

the outlet for each case (Fig. 3.1.9) were within the range of those generated from commercial syringe pumps that are commonly used to generate a controlled flow rate in chip-based microfluidic systems.

The principle that is described here would improve the space utilization in centrifugal microfluidics, for which limited space has been one of the major problems since fluids can only be moved radially outward. When different microchannel arrangements are considered during the design process, more delicate and systematic microfluidic networks could be expected by efficiently utilizing the limited space in order to achieve integrated functions that are necessary for multi-step sample manipulation for a wide range of biological and chemical research.

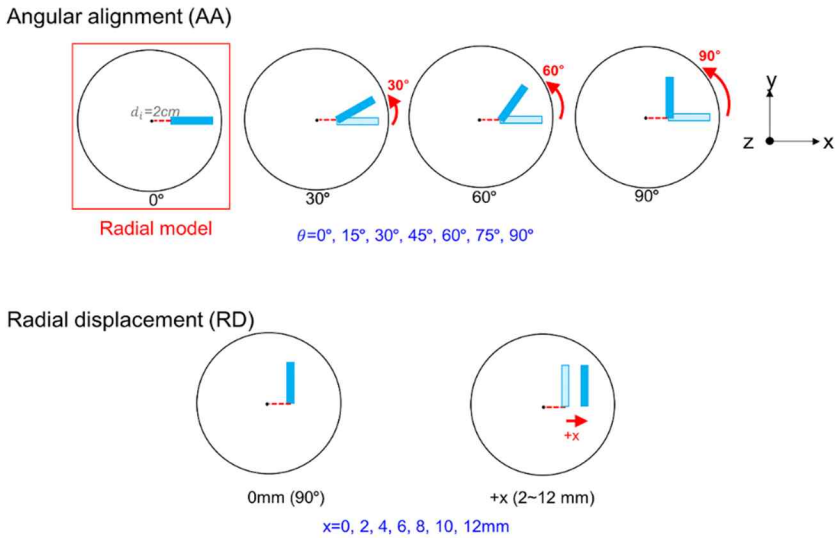

Fig. 3.1.1 Top view schematic for two non-radial models: angular alignment (AA) and radial displacement (RD). The three-dimensional (3D) rectangular channel aligned at 0° represents a radial model. The AA configuration is a modification of the radial model by revolving it by 15° about the inlet located at a radial distance of 20 mm from the center of the disk. The RD configuration is a modification of an AA configuration with a 90° angular alignment by moving it radially outward by 2 mm.

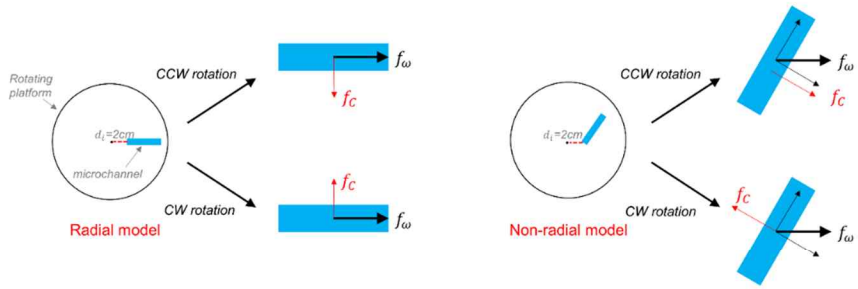

Force relationship	
Radial model	Non-radial model
$\frac{\lvert\vec{F}_{perpendicular}\rvert}{\lvert\vec{F}_{longitudinal}\rvert} = \frac{\lvert\vec{f}_C\rvert}{\lvert\vec{f}_\omega\rvert}$	$\frac{\lvert\vec{F}_{perpendicular}\rvert}{\lvert\vec{F}_{longitudinal}\rvert} = \frac{\lvert\vec{f}_C \pm \vec{f}_{\omega,perpendicualr}\rvert}{\lvert\vec{f}_{\omega,longituditnal}\rvert}$

Fig. 3.1.2 Force balance of the rotational forces acting on a moving fluid along the rectangular microchannel generated by the rotating platform either in the clockwise (CW) or the counter clockwise (CCW) direction. In the non-radial model, the force relationship (defined as the ratio between the force acting along the channel and the force acting perpendicular to the channel) becomes different from that in the radial model due to the decomposition of the centrifugal force.

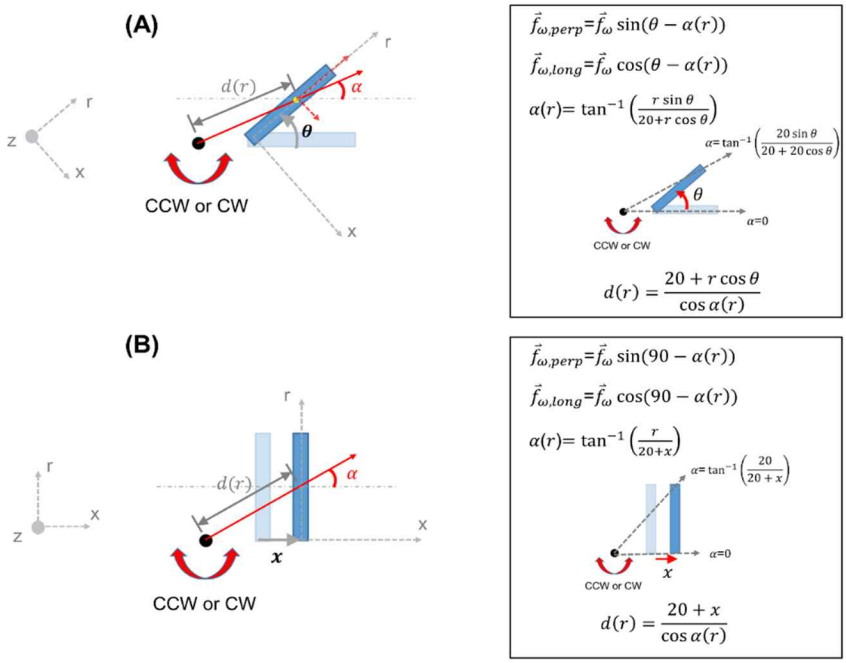

Fig. 3.1.3 Decomposition of the centrifugal force in the (A) angular alignment (AA) and (B) radial displacement (RD) configuration. Unlike for the radial model, the distance vector from the center of the disk (black dot) to the points along the channel ($\vec{d}(r)$), which determines the centrifugal force, is not aligned lengthwise with the channel, and this creates a decomposition in the centrifugal force with one in the longitudinal direction and the other in the perpendicular direction with respect to the channel. The light-colored rectangular shape is the channel in the initial configuration and the dark-colored one is the channel in the modified configuration.

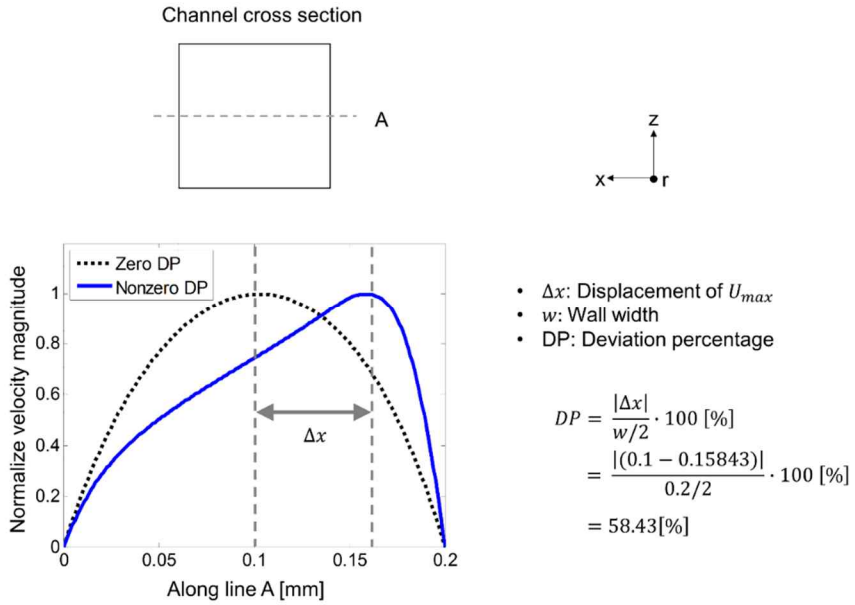

Fig. 3.1.4 Calculation for the flow deviation percentage (DP) for an asymmetric velocity profile. A velocity profile (dotted line) with typical laminar flow is symmetrically parabolic with a maximum velocity located at the center (DP = 0). Significant changes are observed when the velocity profile (solid line) deviates to one of the sidewalls with a maximum velocity that is no longer at the center (DP ≠ 0).

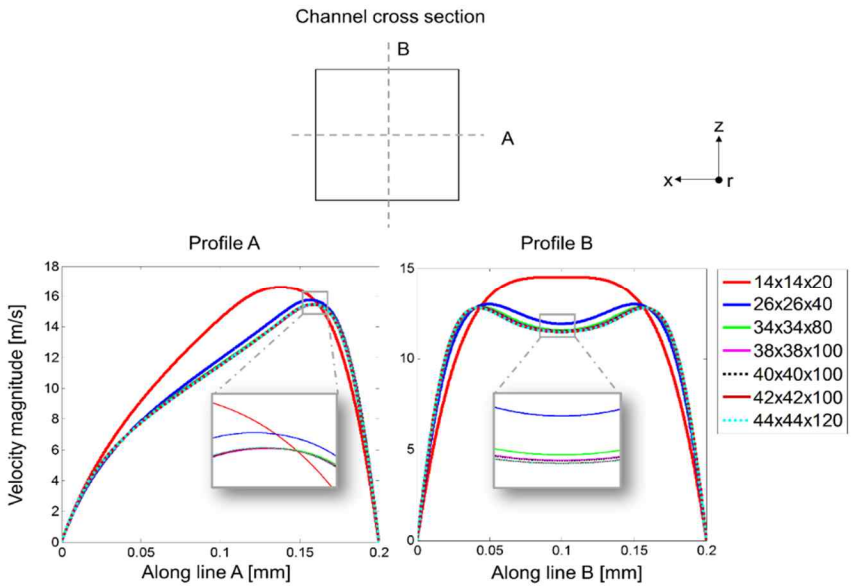

Fig. 3.1.5 Comparison of the velocity profile along lines A and B at the channel outlet to validate the grid independence. The discrepancies between the velocity profiles are reduced as the mesh is refined. The 40x40x100 grid system matches well with the 42x42x120 grid system for both profiles.

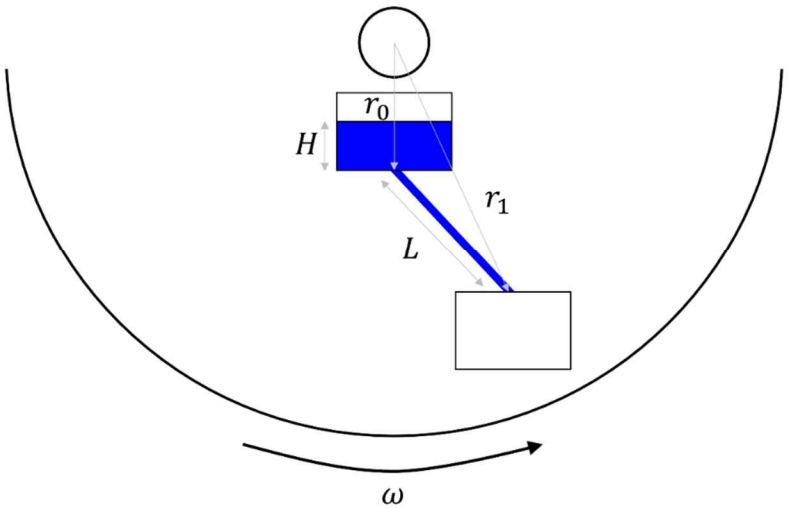

Fig. 3.1.6 Schematic of the channel configuration according to the geometric parameters where r_0 and r_1 are the inner and outer radii of the flowing fluid that fills a microchannel with length L. H is the head of the liquid in the inlet reservoir.

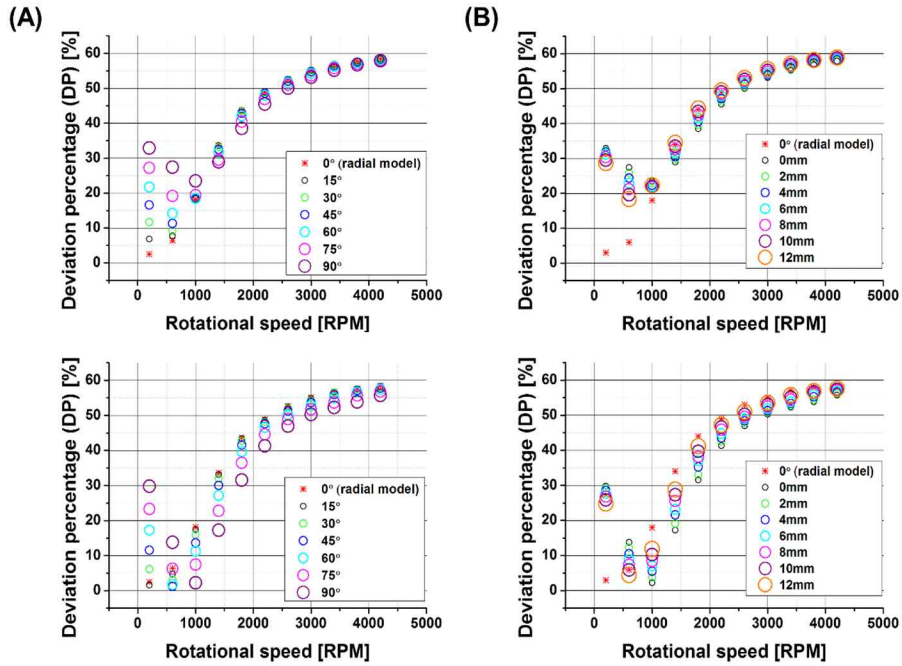

Fig. 3.1.7 Deviation percentage (DP) of the flow at each rotational speed in the (A) angular alignment (AA) and (B) radial displacement (RD) configurations for both CCW (top row) and CW rotation (bottom row). Note that DP trend changes by the critical RPM (1000 RPM). DP for the CCW and CW rotation are also different especially at an intermediate rotational speed with an effective Coriolis force (>1000 RPM) such that the CW rotation causes larger variations of DP for both configurations compared to the CCW rotation, with respect to the channel arrangements. As the rotational speed further increases, the individual DP for either AA or RD at given rotational speed becomes saturated regardless of the direction of the rotation.

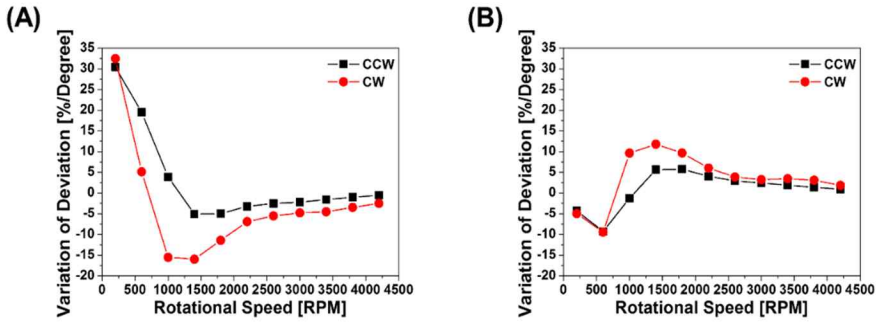

Fig. 3.1.8 Graph of the variation in the deviation (VD) for the (A) angular alignment (AA) and (B) radial displacement (RD) configurations. Each point represents the amount of flow deviation created by systematically changing the channel arrangement of AA and RD at a constant rotational speed. Refer to Fig. 10 for the definition of DP in detail.

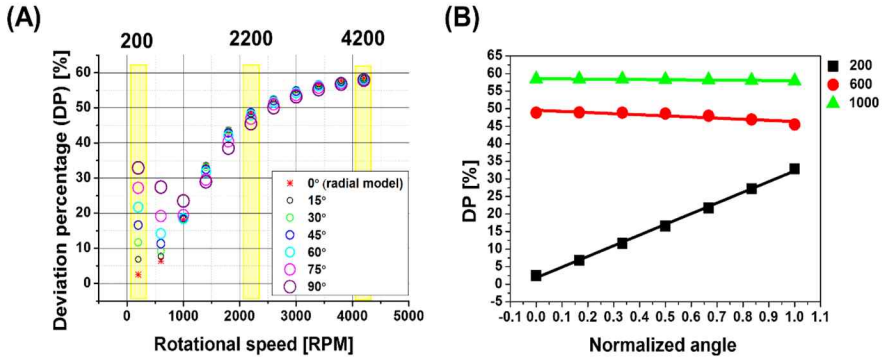

Fig. 3.1.9 Procedure to generate the graph of the variation in the deviation (VD). (A) Deviation percentage (DP) for the angular alignment (AA) configuration with a CCW rotation. (B) Linear regression on a change in the deviation at 200, 2200, and 4200 RPM according to the channel arrangement (AA or RD). In this linear regression procedure, the angles and displacements were normalized to a range from 0 to 1 in order to quantitatively compare the influence of AA and RD on the flow deviation at each rotational speed. The slope corresponds to VD at each rotational

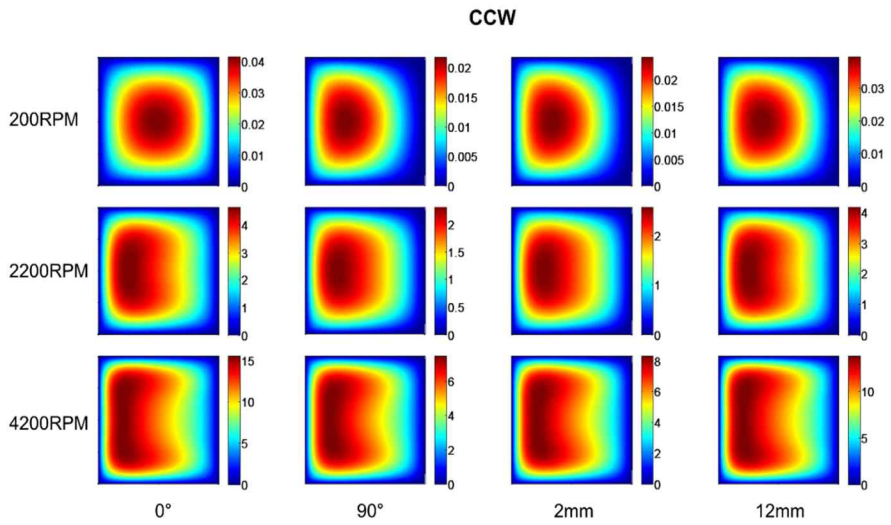

Fig. 3.1.10 Pseudocolor plots of the velocity at the outlet for the CCW rotation. Either an angular alignment (AA) or a radial displacement (RD) generates a flow deviation in the same direction. The Coriolis force is dominant at 4200 RPM, and the flow deviations are almost identical, presenting saturation of the deviation percentage (DP) at a high rotational speed. The color bar scales are different for each case in order to visualize the flow deviation in all pseudocolor plots for the rotational speed ranges from low to high.

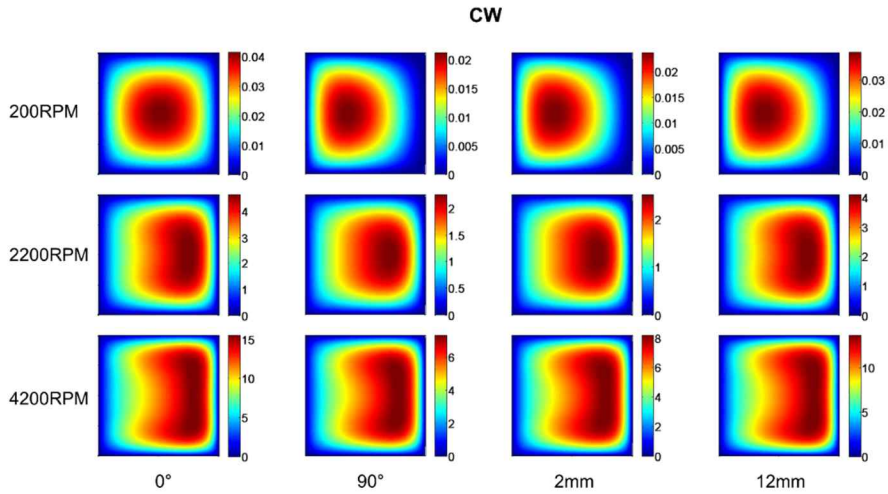

Fig. 3.1.11 Pseudocolor plots of the velocity at the outlet for the CW rotation. Although the direction of the flow deviation initially depends on the channel arrangement at a low rotational speed, it changes to that of the Coriolis force as the rotational speed increases. AA: angular alignment, RD: radial displacement. The color bar scales are different for each case in order to visualize the flow deviation in all pseudocolor plots for the rotational speed ranges from low to high.

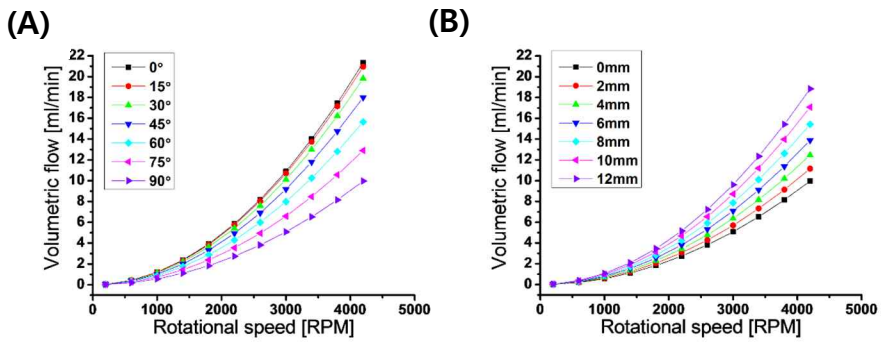

Fig. 3.1.12 Volumetric flow rate for the (A) angular alignment (AA) and (B) radial displacement (RD) configurations. At a constant rotational speed, the volumetric flow rate changes systematically with the channel arrangements for both the AA and RD configuration.

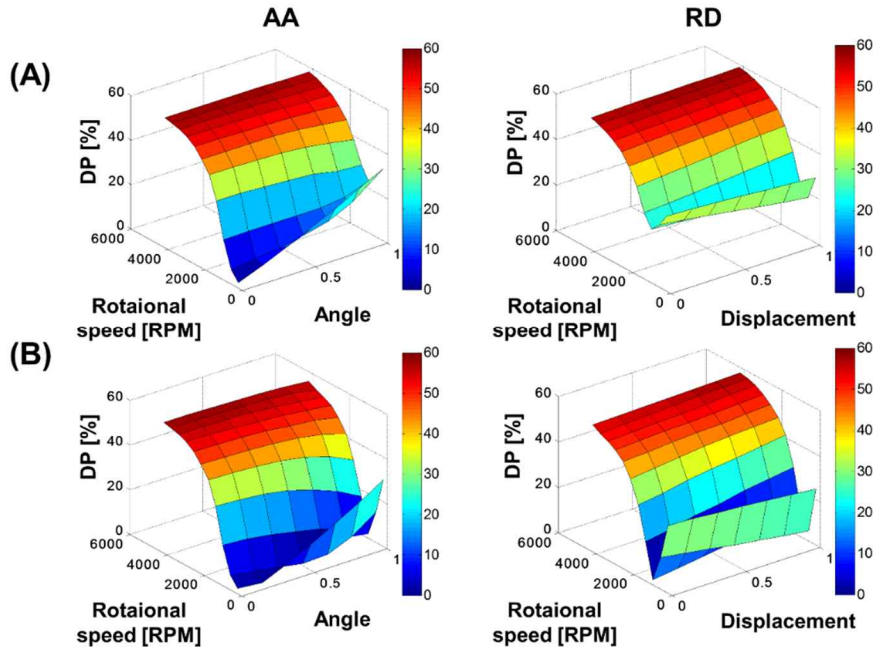

Fig. 3.1.13 Flow deviation percentage (DP) in absolute values with the normalized angle/displacement and a rotational speed (RPM) for (A) CCW and (B) CW rotation. The CW rotation displays a larger variation at a low rotational speed for both configurations, indicating that the flow deviation is more susceptible to the channel arrangement at a low rotational speed. At a high rotational speed, almost no difference is shown between the CW and CCW rotation for both the angular alignment (AA) and the radial displacement (RD) configurations, indicating saturation in the flow deviation when the Coriolis force is dominant.

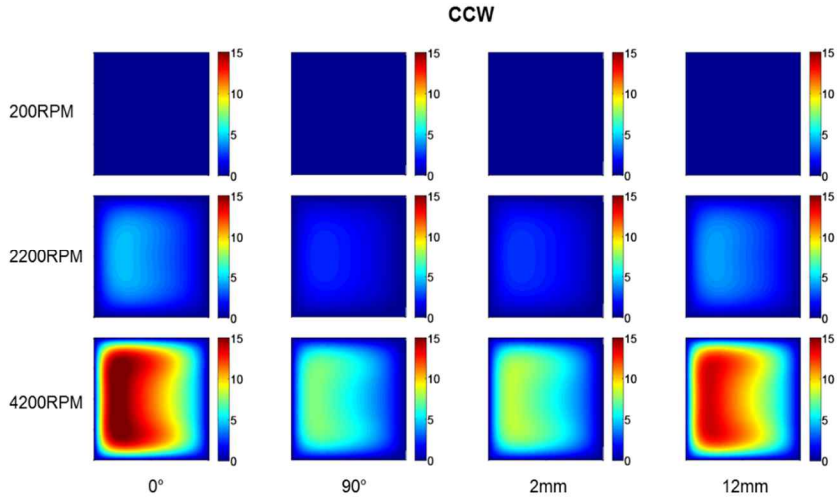

Fig. 3.1.14 Re-drawn figure of Fig.3.1.10 that displays pseudocolor plots of the velocity at the outlet for the CCW rotation. The limits for colorbar ranges are identically set from 0 to 15m/s. At 4200RPM, the plot shows clear differences among velocity magnitude by different channel arrangements, while DPs are maintained at the similar level.

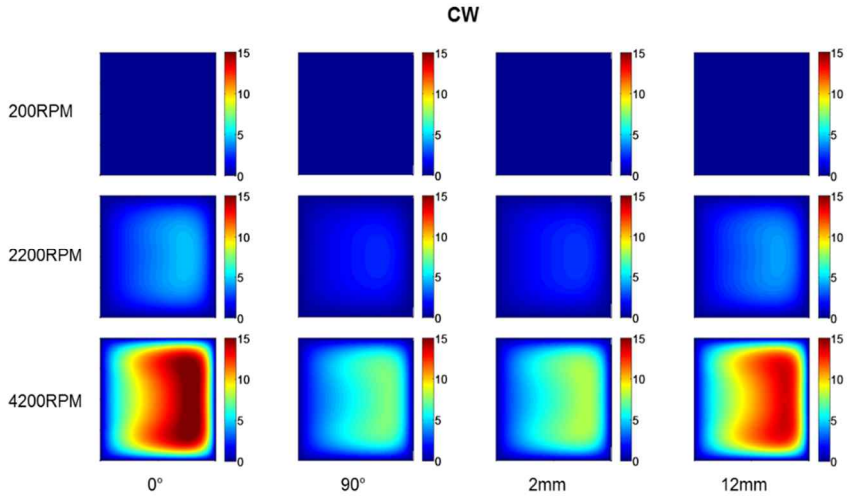

Fig. 3.1.15 Re-drawn figure of Fig.3.1.11 that displays pseudocolor plots of the velocity at the outlet for the CW rotation. The limits for colorbar ranges are identically set from 0 to 15m/s. At 4200 RPM, the plot shows clear differences among velocity magnitude by different channel arrangements, while DPs are maintained at the similar level.

Table 3.1.1. Non-dimensional factors involved in determining the ratio between the force acting along the channel and the force acting perpendicular to the channel for radial and non-radial models.

Radial model		Non-radial model (Angular alignment (AA) configuration)		Non-radial model (Radial displacement (RD) configuration)	
RPM	k_{fluid}	Angle	k_{AA} at outlet	Displacement [mm]	k_{RD} at outlet
200	0.21	0°	0	0	1
600	0.63	15°	0.1317	2	1.1
1000	1.05	30°	0.2679	4	1.2
1400	1.47	45°	0.4142	6	1.3
1800	1.89	60°	0.5774	8	1.4
2200	2.31	75°	0.7673	10	1.5
2600	2.73	90°	1	12	1.6
3000	3.15				
3400	3.57				
3800	3.99				
4200	4.41				

Table 3.1.2 Grid independence test. The parameters of the analysis include the flow deviation percentage (DP; defined as the percentage of the maximum velocity displacement from the center to the side wall in the direction of the channel width), magnitude of the maximum velocity (u_{max}), volumetric flow rate (Q), and mean difference of the velocity magnitude for the velocity profiles at the outlet in both the x (profile A) and the z (profile B) directions (Fig. 3.1.5).

Grid size (x x z x r)	DOF	u_{max} [m/s]	% diff.	DP [%]	% diff.	Q [mL/min]	% diff.	Profile A [m/s]	Profile B [m/s]
14x14x20	18900	16.6091		38.24		20.3542			
18x18x40	59204	16.0379	3.4391	52.33	36.8462	20.6879	1.6395	1.101	0.9964
26x26x40	119556	15.7475	1.8107	56.94	8.8095	21.0511	1.7556	0.3316	0.378
32x32x50	222156	15.564	1.1653	58.58	2.8802	21.206	0.7358	0.1363	0.2025
34x34x80	396900	15.441	0.7903	58.9	0.5463	21.2456	0.1867	0.0882	0.1201
36x36x100	553076	15.4205	0.1328	58.68	0.3735	21.2808	0.1657	0.0348	0.0519
38x38x100	614484	15.4321	0.0752	58.8	0.2045	21.3122	0.1476	0.008	0.0148
40x40x100	679124	15.438	0.0382	58.43	0.6293	21.3406	0.1333	0.0172	0.0293
42x42x120	894916	15.4436	0.0363	58.45	0.0342	21.3662	0.1200	0.0188	0.0295
44x44x120	980100	15.451	0.0479	58.12	0.5646	21.3896	0.1095	0.0092	0.0097

3.2 Centrifugal microfluidic-based viscometer [89]

Viscosity of the fluid is one of the key indicators in chemical and biological studies to represent fluidic conditions. However, commercially available viscometers are often expensive and time consuming to analyze large samples. Here, a centrifugal microfluidic viscometer based on Poiseuille law was developed and its performance with samples with four different glucose concentrations was demonstrated.

3.2.1 Introduction

Viscosity measurement technology has been of great interest for researchers in both academia and industry to investigate rheological properties of a fluid. For biomedical research, in particular, viscosity measurement plays a critical role in patient monitoring as blood visosity can be altered by various factors including glucose levels [90], haematocrit, erythrocyte deformability, pH, and etc. [91]. Commercially available viscometers (e.g. Cone and plate viscometer and capillary viscometer), however, are often highly expensive and time consuming to analyze large samples. In order to provide rapid, accurate, and cost effective method, microfluidic system has emerged as an alternative analytical tool for measuring viscosities [92].

Recently, Kang et al. has developed an integrated microfluidic viscometer based on Poiseuille flow Eq. (3.2.1) and demonstrated its capability to measure relative viscosity of the sample fluid [93, 94].

$$\Delta P = RQ \quad (3.2.1)$$

where ΔP is the pressure drop, R is the fluidic resistance, and Q is the flow rate of the sample fluid.

However, chip-based microfluidic system also has a limitation of using large external pumping device in which pumping efficiency is highly dependent on fluid types and may drop with the fluid that has low shear rate.

Centrifugal microfluidic system, on the other hand, is a compact device that operates by an embedded rotor generating rotational forces to pump samples with high efficiency. In this study, the design criteria that has been used previously [93, 94] was applied to centrifugal microfluidic system and the possibility of its application has been demonstrated.

3.2.2 Materials and Methods

Rotating device integrated with disk platform, DC motor, and speed controller (Fig.3.2.1) based on pulse width modulation (PWM) technique has been developed to regulate rotational forces and pumping velocity of the sample. Microfluidic chip made of polydimethylsiloxane (PDMS) comprises four identical structures and each has two loading chambers, 140 resistance channels, and a waste chamber.

For the experiment, four blue colored glucose solutions with different concentrations (0, 5, 10, and 20%) and one red colored distilled water for reference fluid were prepared.

Under assumptions that the fluidic resistance (R) is proportional to

viscosity (μ) and pressure drop (ΔP) in centrifugal microfluidics is proportional to density (ρ), the relationship between viscosity of the sample (μ_{spl}) and that of the reference(μ_{ref}) described by Kang et al.[93, 94] is modified into the following equation (Fig. 3.2.2):

$$\frac{\mu_{spl}}{\mu_{ref}} = \frac{N_{spl}\rho_{spl}Q_{ref}}{N_{ref}\rho_{ref}Q_{spl}} \tag{3.2.2}$$

where N_{spl} and N_{ref} are the number of resistance channels filled with the sample and reference fluid respectively and Q is a volumetric flowrate. Considering that the average velocity, U generated in centrifugal microfluidic system is proportionally related to the density [18], $\frac{\rho_{spl}Q_{ref}}{\rho_{ref}Q_{spl}}$ can act as a constant.

3.2.3 Results

At 700 RPM with 5μl samples at each loading chamber, the higher the viscosity is, the greater the number of resistance channels is filled up with the sample (Fig. 3.2.3), demonstrating that Eq (3.2.2) can be properly applied to centrifugal microfluidics for viscosity measurement

3.2.4 Discussion

Unlike microfluidic system in which flow can be entirely regulated by external syringe pump, interplay of a number of influential factors including centrifugal force, density, viscosity, and fluid-surface interfaces determine flow characteristics in centrifugal microfluidic system. Therefore, the relationship

described in Eq. (3.2.2) could be too simplified to attain high reproducibility. However, the resultant fluid pattern obtained in accordance with the proposed relationship suggests that improved design criteria based on careful considerations on influential factors and their individual power of impacts could enhance the performance.

Moreover, pressure drop variations in centrifugal microfluidic system as the fluid from inlet propels to outlet and the level of fluid in inlet decreases could be another issue of concern for improvement of the performance [22]. Positioning of the resistance channels before negative pressure becomes effective and retain the effect of positive pressure-driven flow may improve precisions of the result.

Continuous monitoring of the flow generated in centrifugal microfluidic system should be particularly beneficial for precise investigation of the operation. However, observing the flow process that takes place in rotating platform is very challenging and requires a high speed camera which is highly expensive. Development of simple and maintainable method for monitoring rotating microchannels may play an important role in understanding fluid flow fundamentals in centrifugal microfluidic system and its reliable applications.

3.2.5 Conclusion

For future work, chip design needs to be optimized based on a strong theoretical basis and validation through systematic experiments to achieve better reproducibility and eventually to achieve successful performance with non-Newtonian fluid (e.g. blood).

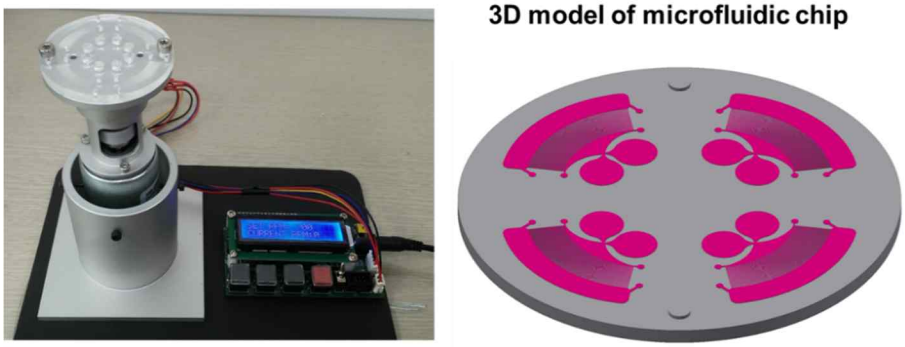

Fig. 3.2.1 Centrifugal microfluidic system for measuring viscosity of the sample. Photogragh of the control device with circular microfluidic chip on the top (left) and 3D model of microfluidic chip (right).

- **Poiseuille flow equation:**

$$\Delta P = QR$$

ΔP=pressure difference, Q=flowrate, R=channel resistance

- **Hydraulic resistance for rectangular cross-section:**

$$R_{channel} \sim \frac{12\mu L}{wh^3(1-0.630h/w)} \rightarrow \boxed{R \propto \mu}$$

μ=viscosity, L=length, w=width, h=height

Microfluidic chip

$$\Delta P_{spl} = \Delta P_{ref}$$

$spl = sample, ref = reference\ fluid$

$$\frac{\Delta P_{spl}}{\Delta P_{ref}} = \frac{R_{spl}Q_{spl}}{R_{ref}Q_{ref}} = 1 \rightarrow \frac{\mu_{spl}}{N_{spl}}Q_{spl} = \frac{\mu_{ref}}{N_{ref}}Q_{ref}$$

$$\frac{\mu_{spl}}{\mu_{ref}} = \frac{N_{spl}Q_{ref}}{N_{ref}Q_{spl}}$$

N=number of channel filled with a fluid

Centrifugal microfluidic chip

$$\Delta P \propto \rho$$

$\rho = density$

$$\frac{\rho_{spl}}{\rho_{ref}} = \frac{R_{spl}Q_{spl}}{R_{ref}Q_{ref}} = \frac{\mu_{spl}N_{ref}Q_{spl}}{\mu_{ref}N_{spl}Q_{ref}}$$

$$\frac{\mu_{spl}}{\mu_{ref}} = \frac{N_{spl}\rho_{spl}Q_{ref}}{N_{ref}\rho_{ref}Q_{spl}}$$

N=number of channel filled with a fluid

Fig. 3.2.2 Modified relationship between viscosity of the sample (μ_{spl}) and that of the reference(μ_{ref}) for applying to centrifugal microfluidic chip

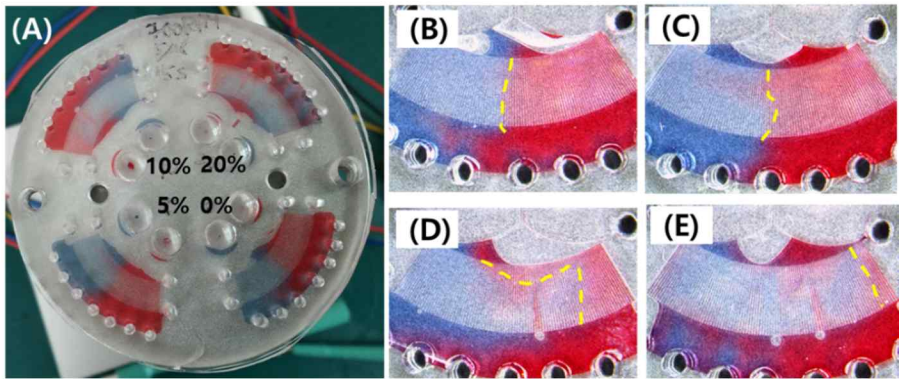

Fig. 3.2.3 (A) Experimental results with four different glucose concentrations. (B-E) Enlarged view of the image (B) for 0, 5, 10, and 20% glucose solutions (Blue) with reference fluid (Red) respectively. Yellow dotted line indicates a boundary line between the sample and the reference fluid.

3.3 Hypergravity-induced multicellular spheroid generation [95]

In living tissue, cells exist in three-dimensional (3D) microenvironments with intricate cell-cell interactions. To model such cellular environment, various techniques for generating cell spheroids have been proposed and improved continually. However, previously reported methods still have limitations on the levels of uniformity, reproducibility, scalability, through-put, etc. Here, a centrifugal microfluidic-based spheroid (CMS) formation method for generating co-culture as well as mono-culture 3D spheroid in highly controlled manner was presented. Circularly arrayed microwells were designed to allow even distribution of cells introduced at the center of a rotating platform and to provide identical hypergravity conditions at each well by centrifugal forces generated. Compared to the conventional well plate-based spheroid (WPS) formation method, CMS formation method significantly promotes sphericity and consistency for both size and shape with high production yields. In addition to mono-culture spheroids, co-culture spheroids in concentric, Janus, and Sandwich shape using human adipose-derived stem cells (hASC) and human lung fibroblasts (MRC-5) were successfully generated, demonstrating versatility of CMS formation method. The new method proposed for generating 3D spheroids is believed to become one of essential technologies in the field of 3D cell culture systems and is also expected to provide an innovative means to assess cellular responses including cell motilities in different hypergravity conditions.

3.3.1 Introduction

Three-dimensional (3D) spheroid cell culture is of great significance for *in vitro* biological studies especially for drug screening and cancer cell research [96]. 3D cells have important advantages of mimicking complex *in vivo* environment, which have been highly limited by routine means of 2D cell culture [97]. Spheroid culture especially has shown dramatic effects in stem cell biology for enhancing differentiation and proliferation of mesenchymal stem cells [98-100]. However, although existing techniques for 3D spheroid formation (e.g. hanging drop technique (HDT) [101], liquid-overlay technique (LOT) [102], carboxymethyl cellulose technique (CCT) [103], Bioreactor [104]) have their own benefits for example mass production allowed by large bioreactors, there are still plenty of room for improvement in terms of handling, regulating spheroid size and shape, generating co-culture spheroids, or working with small number of cells [105]. Depending on cell types and culture techniques, reproducibility and production yield in generating spheroids vary considerably probably due to their complex interactions which is still not fully understood [106]. For example, in the previous study, LOT which has been turned out to be the most suitable technique among other methods including HDT and CCT for generating spheroids with primary osteoblasts, fibroblasts, and endothelial cells, has large variations in rate of yield and in size from 60 to 100% and 400 μm to 700 μm respectively [106].

Motivated by HDT which is based on the cell sedimentation at an air-liquid

interface under the force of Earth's gravity (1G) and the discovery that cells tend to form aggregates under either short term [107] or long term hypergravity conditions [108], a novel method, centrifugal microfluidic-based spheroid (CMS) formation method, was demonstrated for rapid and easy formation of 3D spheroids by promoting cell aggregation and compactness with continuous hypergravity conditions generated by the centrifugal force.

Centrifugal microfluidic system also referred to as lab-on-a-CD has been primarily utilized for biomedical applications such as immunoassay, DNA microarray hybridization assay, colormetric assays for detecting biochemical markers, and nucleic acid amplification (PCR) assay, allowing multiple laboratory procedures (e.g. mixing, valving, sample splitting) to be processed in one single device by making good use of channel designs and rotating forces to manipulate fluids. Such integrating technique and efficient fluid control capabilities have recently guided to a number of blood analysis systems that are fully automated [109] and substantially simplified with all-in-one design [110], demonstrating considerable advancements of centrifugal microfluidic system in point-of-care diagnostics [111]. Development of several cell based assays for biological research has been also attempted by this CD-based system such as cell lysis and cell viability assays, but cell research in this area is relatively unexplored [112]. To the best of the knowledge, the proposed method is the first versatile CD-based spheroid generation method. For evaluating CMS formation method, rotating device composed of DC motor, rotating platform, and speed controller was developed. The device made of aluminum was small in size (100 x 100 x 150 mm) and light in weight (~860 g), achieving portability.

The speed controller developed for regulating a rotational speed in a range from 200 to 4500 RPM, which corresponds to G-force range from 1 G to 521 G at each circularly arrayed microwell, was integrated. By CMS formation method, both mono- and co-culture spheroids were successfully generated with high production yields using human adipose-derived stem cells (hASC) and human lung fibroblasts (MCR-5) both of which are primary interests especially in drug screening based on their 3D spheroid models to investigate therapeutic responses [113-116]. With the sequential co-culture process, concentric, Janus, and Sandwich spheroid were successfully created with cell-cell interfaces between the two different cells. The results show that centrifugal microfluidic technology has a potential to provide a new solution for generating co-culture spheroids of two or more cell types as well as mono-culture spheroids in controlled manner in terms of size, shape, and cell position and may extend its usage in 3D organoid study in which environmental cues are essential key to successful recapitulation of human organs [117]. In recent studies, hypergravity stimulation has been turned out to be a vital physical cue that can significantly improve osteogenic differentiation of mesenchymal stem cells [118] and neuronal differentiation [119] as well. Moreover, in addition to chemical, mechanical, or such physical cues, co-culture can also significantly promote structural and functional differentiation and therefore has a crucial role in organoid development [120]. Considering that CMS culture system is capable of creating various types of co-culture spheroids in different structural forms (concentric, Janus, and sandwich types) providing hypergravity stimulations at the same time, synergistic effects on organoid culture can be expected with the

proposed method by regulating cellular positioning in a controlled manner and by creating appropriate physical environment.

3.3.2 Materials and Methods

Centrifugal microfluidic system development

A centrifugal microfluidic system composed of a rotating platform, a DC motor (MB-4385E, Nurielectricity Inc., Gu-mi, Republic of Korea), and a speed controller was developed for the experiment (Fig. 3.3.1A and Fig. 3.3.8). The rotating platform on the top was designed to integrate poly(dimethylsiloxane) (PDMS) spheroid culture substrate fabricated by replica molding technique [121] and the speed controller was developed to regulate the rotational speed of the motor from 200 to 4500 RPM by applying a proportional-integral-derivative (PID) algorithm with pulse width modulation (PWM) technique [122] (Fig. 3.3.9).

PDMS substrate design and fabrication

Two types of PDMS spheroid culture substrate were fabricated; one for CMS formation experiment and the other for a comparative study with conventional well plate-based spheroid (WPS) formation method (Fig. 3.3.1). The former substrate is a PDMS disk with radius of 6 cm where top and bottom layers are reversibly sealed with four fixation screws in order to extract spheroids at the end of the procedure by opening the top layer. The bottom layer contains a hundred 400 x 400 μm microwells circularly arrayed with each well at the same

radial distance from the rotating axis in order to allow even distribution of cells introduced through conically penetrated inlet at the center of the top layer and to provide identical hypergravity conditions at each well by centrifugal forces generated. The barrier wall at the bottom of the conical inlet was designed to block cell suspension at first and to prevent its dispersion outward when it initially introduced so that cells can be evenly distributed as the platform starts to rotate. Dimensions of the substrate is specified in Fig. 3.3.10. The latter substrate is also made of PDMS and is composed of only a bottom layer where hundreds of 400 x 400 μm cylindrical microwells are arrayed at an interval of 0.8 mm.

Cell culture, staining, and live/dead assay

Human adipose-derived stem cells (hASC) (PCS-500-011, ATCC, VA, USA) and MRC-5 human lung fibroblasts (CCL-171, ATCC) were cultured at 36.5°C in 5% CO_2 atmosphere in Dulbecco's Modified Eagle's Medium (DMEM, ATCC 30-2002, ATCC) supplemented with 10% fetal bovine serum (FBS, ATCC-SCRR-30-2020, ATCC) and 1% Antibiotic-Antimycotic (Gibco 15240-062, Thermo Fisher Scientific, Waltham, MA, USA).

MRC-5 cells were stained with CellTracker Red CMTPX (10 mM, Thermo Fisher Scientific), and hASC were stained with CellTracker Green CMFDA (10 mM, Thermo Fisher Scientific) for 30 min before seeded in the spheroid culture substrate for both CMS and WPS formation method.

To analyze cell vitality, live and dead staining was performed using

LIVE/DEAD® Viability/Cytotoxicity Kit for mammalian cells (L3224, Invitrogen, Carlsbad, CA, USA) by following the manufacture's protocol.

Mono-culture spheroid formation

For CMS formation, 4% pluronic F-127 solution (9003-11-6, Sigma Aldrich, St. Louis, MO, USA) which prevents cell attachment, was initially introduced through the inlet port (Fig. 3.3.1A) while the platform rotates so that the solution disperses evenly onto the entire surface of the PDMS spheroid culture substrate by the rotational forces generated. For 1 min, the rotational speed was set at high (~4000 RPM) in order for the coating solution to completely flow into each microwell by removing micro bubbles caught inside. The spheroid culture substrate was then incubated overnight at 36.5°C in 5% CO_2 atmosphere. Afterward, the pluronic solution was washed thoroughly out with DMEM. Then, 2.5 mL of DMEM was introduced to fill the interior space of the CMS substrate and 200 μL of cell suspensions, containing 5×10^5 cells for hASC or 8×10^5 cells for MRC-5, were added through the inlet port. Different cell numbers by cell types were determined considering different cell sizes in which single cell of hASC is about 1.5 times larger than that of MRC-5. The platform was then rotated at 3000 RPM for 1 min, allowing cells to evenly distributed and trapped into the outermost walls of each microwell by the centrifugal force generated (Fig. 3.3.2A). Two different rotational speeds of 1000 and 2000 RPM, which result in approximately 26 and 103 G force [Eq. (3.3.1)] applied to cell clusters placed at each microwell, were used to evaluate centrifugal force effects on

spheroid formation.

$$[G]=\frac{r\omega^2}{9.8} \quad (3.3.1)$$

where r is a radial distance of each microwell from the rotating center in [m], which is 0.23 m in the substrate design, and ω is angular velocity in [rad/s].

For conventional WPS formation method, PDMS surfaces containing hundreds of cylindrical microwells were also coated with pluronic copolymer solution overnight, followed by introduction of 500 μL aliquots of cell suspensions containing 5×10^6 cells for hASC or 9×10^6 cells for MRC-5 to allow approximately 5000 cells/well (Fig. 3.3.2B). Spheroids were formed and cultured at 37°C in 5% CO_2 atmosphere under Earth's gravitational force (1 G) up to Day3.

Co-culture spheroid formation

By means of CMS formation method, concentric, Janus, and Sandwich type of spheroids were successfully created by sequential seeding procedure with different time intervals; short time interval (3 min) for concentric spheroids and relatively long time interval (3 h) for Janus and Sandwich spheroids. Co-culture spheroids were created under hypergravity conditions of 103 G. However, for Janus or Sandwich, different number of cells might be required depending on the cell type in order to create half-and-half shared or equally layered spheroid, considering their different cell sizes. For example, in order to create Janus spheroids with hASC and MRC-5, 2.5×10^5 cells for hASC, of which the single

cell size is approximately 1.5 times larger than that of MRC-5, were first introduced into the CMS culture substrate and rotated at assigned RPMs, followed by introduction of 4.0×10^5 cells for MRC-5 after 3 h. The procedure for creating co-culture spheroids are summarized in Table 3.3.1.

Morphological and statistical analysis

Sphericity and size of the spheroids were measured through image processing of two dimensional fluorescent images (CKX41, OLYMPUS, Japan) based on the sphericity measurement technique suggested by Cho *et al*. [123]. Fluorescent images were converted into binary images to find outlines of each spheroid, which was then used to determine maximum inner circle radius ($R_{MAX, IN}$) and minimum outer circle radius ($R_{MIN, OUT}$) for estimating sphericity by their ratio and size by their mean (Fig. 3.3.11). Image processing and collecting data for sphericity and size were processed by Matlab software R2013b (The Mathworks Inc, Natick, MA). Outliers at 0.05 significance level were removed from the data analysis. The Kruskal-Wallis H test, a rank-based nonparametric test, was used to determine significant differences among the sphericity, the size, and their standard deviations resulted by three different independent variables, cell type, G force level, and time duration. For the comparison among standard deviations, a non-parametric Levene's test was used to verify the equality of variances in samples. All statistical tests were processed by SPSS 17.0 for Windows (SPSS, Inc., Chicago, IL, USA) at the 0.05 significance level.

3.3.3 Results and Discussion

Time lapse images from 5 min to Day3 were taken in order to evaluate process of spheroid formation by both CMS and WPS formation method. CMS culture substrate has its unique design feature of the barrier wall (Fig. 3.3.1A) that allows cells to uniformly spread into microwells placed at outer edge; until the platform starts to rotate, the cell suspension introduced at the conical inlet is confined by the barrier permitting pipetting or gentle rotation to avoid precipitation of cells and to allow their even distribution right before spreading by the rapid rotation (Step 4, Fig. 3.3.2A). Then, cell suspensions were simply pipetted up and down to re-suspend cells (Step 5), but if the procedure of varying rotational speed with precise control to re-suspend cells by gentle rotation and to activate the spread by rapid rotation is implemented, entire process can be possibly automated and its effectiveness can be further improved. Another unique feature of the CMS culture substrate is the slanted edge (see Fig. 3.3.1A) at the top layer which prevents cells escaping from the well during media exchange through pores surrounding the inlet. Unlike WPS formation method, once cells were properly distributed in CMS culture substrate, cell aggregates situated at each microwell appeared to have reversed U-shape immediately after their settlements and the shape gradually changed into spherical (Fig. 3.3.3) Afterward, the size of the spheroids created by the both methods gradually decreased over time as their compactness improved.

CMS formation method showed superiority over WPS formation method as the sphericity increased with CMS formation method while decreased with WPS formation method over time (Fig. 3.3.4 and Fig. 3.3.12). Comparing last

three time durations, 24 h (Day1), 48 h (Day2), and 72 h (Day3), mean sphericity was significantly greater with CMS formation method compared to WPS formation method for both cell types (Fig. 3.3.5). However, sphericity of the spheroids created by CMS formation method also started to decline at either Day2 or Day3, and such effect has appeared more distinctively at higher hypergravity condition. For both cell types, sphericity under 103 G became significantly inferior to that under 26 G, at Day2 for hASC and at Day3 for MRC-5 respectively, suggesting that hypergravity condition less than 103 G might be needed to retain high sphericity in 48 h. Shape consistency of the spheroids determined by standard deviations of the sphericity measurement was significantly enhanced by CMS formation method compared WPS formation method at 24 h and Day2, but such effects disappeared at Day3 for both cell types as standard deviations of the spheroids cultured by CMS formation method get larger to the level of those by WPS formation method (Fig. 3.3.5A), suggesting that long term culture may be inappropriate to retain shape consistency.

Degree of size reduction was significantly greater with WPS formation method compared to CMS formation method despite of the same well sizes designed for both WPS and CMS formation method and different densities of cell suspension were chosen by the two methods and cell types. Moreover, while both cell types experienced similar size reduction by CMS formation method, MRC-5 apparently experienced greater size reduction than hASC by WPS formation method, suggesting that CMS formation method might be more appropriate for size control in spheroids generation compared to the

conventional method. The significant difference of size generated between WPS formation method and CMS formation method may be associated with hypergravity conditions known to facilitate cell growth [108]. Cell aggregation with enhanced cell proliferation can create sufficient size of spheroids even with small number of cells avaliable, which was one of major limitations for creating spheroids with rare cell types such as cancer stem cells or primary stem cells [105]. The level of hypergravity conditions also had effects on size but only for MRC-5. While sizes created by 26 G and 103 G were similar for hASC, those were different for MRC-5 as its spheroids created under the higher G environment were significantly smaller than those created under the lower G environment, demonstrating that effects of hypergravity condition can differ by cell types. Size consistency, which can be estimated by its standard deviations, was significantly improved by increasing the level of hypergravity conditions. Spheroids created under 103 G had more uniform size compared to those created under 26 G and to WPS formation method (Fig. 3.3.5B), suggesting that the level of hypergravity conditions has positive effects on size consistency.

Above-mentioned results show that CMS formation method has advantages over the conventional WPS formation method for creating spheroids in terms of shape reproducibility, size control, and uniformity. It also may have potential benefits for dealing with rare cell types by utilizing hypergravity conditions to facilitate cell proliferations simultaneously while creating spheroids. However, to achieve optimum shape and size while attaining high consistency, hypergravity conditions need to be properly tuned by cell types.

Another advantages of CMS formation method over WPS formation method is that the production yield reaches to 100 % (Fig. 3.3.13) without cell waste, and therefore much less numbers of cells were needed for generating comparable size of the spheroids with CMS formation method to those with WPS formation method. Cylindrical shape of well-arrays for WPS formation method has structural limitations of having spaces between each well even with their tight arrangement, on which cells can deposit instead of entering into the wells during cell seeding procedure. Even if the identical cell suspension density per well was taken into consideration in the experiment, spheroids created by WPS formation method turned out to have much smaller sizes once they start to aggregate at 4 h, which can be attributed to the cell loss (Fig. 3.3.4 and Fig. 3.3.5).

Spheroids created by CMS formation method were carried in long term culture under continuous hypergravity conditions to validate cell viability, which resulted in most (>99%) live cells at seven days of culture (Fig. 3.3.14). Such result demonstrates that CMS formation method creates spheroids with no perceptible damage.

Versatility of CMS formation method has been also demonstrated by generating co-culture spheroids of various shapes including concentric, Janus (Fig. 3.3.6), and Sandwich (Fig. 3.3.7) with different sequential seeding procedure (Table 3.3.1). For concentric spheroids, two different cells needed to be sequentially introduced in a short time interval since once the initial cell suspension composed of single cell type evenly spreads into each microwell and settles within reversed U-shape due to centrifugal force applied, another

cell type introduced shortly can place at the sunken area shown at the central part of the reversed U-shaped cell aggregation (Fig. 3.3.3). For Janus spheroids, on the other hand, the time interval for the sequential seeding should be longer since the reversed U-shape needs to be filled up by its retraction over time in order to allow another cell type introduced afterward to be occupied the bottom half. With 24 h of culture, concentric and Janus type of spheroids composed of hASC and MRC5s were successfully created (Fig. 3.3.6). Sequential seeding procedure in three steps created three different cell layers like a sandwich (Fig. 3.3.7), demonstrating possibility to further enhance its versatility.

Spheroid model particularly plays a significant role in drug testing and cancer research [124, 125], where evaluation of different proliferative and metabolic responses depending on cell types is primarily important to develop new anti-cancer drugs. However, issues have been raised in terms of reproducibility due to discrepancy among previously reported experimental data especially in cancer research where drug screening using spheroid model is one of the major part in the field [126]. For the possible source of such variability, the recent study suggested that morphological parameters including spheroid volume and shape can be one of the most influential factors [127]. In this regard, CMS formation method may provide an essential solution as the experimental results have shown its excellent performance for creating spheroids with high sphericity and enhancing consistency of the spheroids in terms of both size and shape.

For biomedical research particularly for drug discovery, achieving high productivity is also an essential part of work [128]. In this aspect of view, CMS

formation method is potentially beneficial. Design modifications to the bottom layer of the cell culture substrate to contain more microwells in which cells are seated can increase the number of spheroid generated while maintaining 100 % of production yield without cell loss. For example, the simplest modification might be reducing well size or increasing radius of the microwell position. addition of microwells at inner side can be considered as well sparsely enough to deliver cell suspensions to the outermost microwells. Stacking multiple substrates can be another solution. With such stacking up method, production yield can be increased 10 to 100 fold compared to the present design. Moreover, CMS formation method can considerably reduce laboratory work as it integrates functions of centrifugation, which is also necessary procedures for Aggrewell system either to remove bubbles or to generate clusters within the microwells [129]. Therefore, such integration can improve work efficiency and provide synergetic effects on the production rate.

CMS formation method has shown its capability of generating co-culture spheroids, which should be highly beneficial for advanced study especially in synthetic biology where the mechanism behind cell-cell interactions between different cell populations is of great interest [130]. Moreover, considering that human tissues are involved in complex cellular interactions within various cell types, 3D co-culture model would better recapitulate *in-vivo* microenvironment and their interactions may vary by different surroundings depending on their individual characteristics of the cell types. Indeed, during the experiment of generating co-culture spheroid, distinctive feature of MRC-5 could be observed when co-cultured with hASC. During the sequential seeding procedure

regardless of seeding order, whether MRC-5 was seeded prior to hASC or the opposite, MRC-5 tended to penetrate into inner side of the hASC, which can be highly relevant to their individual motility characteristics [131, 132]. Such motility difference between hASC and MRC-5 could be the reason for imperfect shape of co-culture models such that MRC-5 was likely to form larger proportion than hASC. For future work, this research can be extended to studying cell physiology under different levels of hypergravity conditions more in depth by applying different cell types not limited to MRC-5 or hASC.

3.3.4 Conclusion

A new method for rapid and efficient generation of 3D spheroids using a centrifugal microfluidic system was presented, demonstrating new potentials of the centrifugal microfluidic technologies for the future applications in 3D spheroid formation. Compared to conventional WPS formation method, CMS formation method resulted in better performance in terms shape reproducibility, uniformity, size control, and production yield by permitting even distribution of cells into each microwell without cell loss with the aid of centrifugal force generated. Versatility of the method was also demonstrated by successfully creating co-culture spheroids in different forms including concentric, Janus, and Sandwich within 24 h. Considering that conventional organoid culture has been generally limited to simple mixture of different cell types in co-culture models, the ability to precisely control cell positioning in spheroids by exquisitely stacking different cell types could take on new roles in organoid research by allowing potentially unique morphological features. Achieving co-culture as

well as mono-culture with CMS formation method, the proposed method is believed to make an important contribution to the development in 3D cell culture technology.

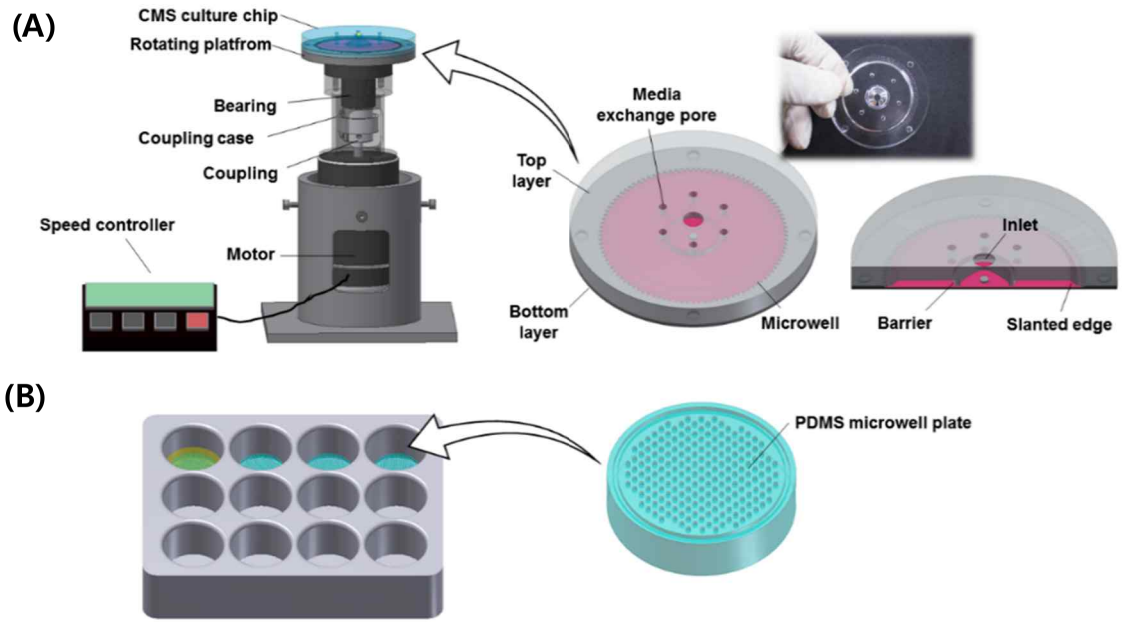

Fig. 3.3.1 Spheroid culture system configurations. (A) Centrifugal microfluidic device with rotational speed controller. A top layer and bottom layer of the PDMS spheroid culture chip placed on the top of the rotating plate were sealed and fixed by eight screws and nuts in order to detach the two layers as necessary for example to extract spheroids created inside the microwells. Dimensions of the chip are shown in Fig. S3 (B) Circular PDMS slice containing hundreds of cylindrical microwells was fabricated to fit into each well of 12-well culture plate.

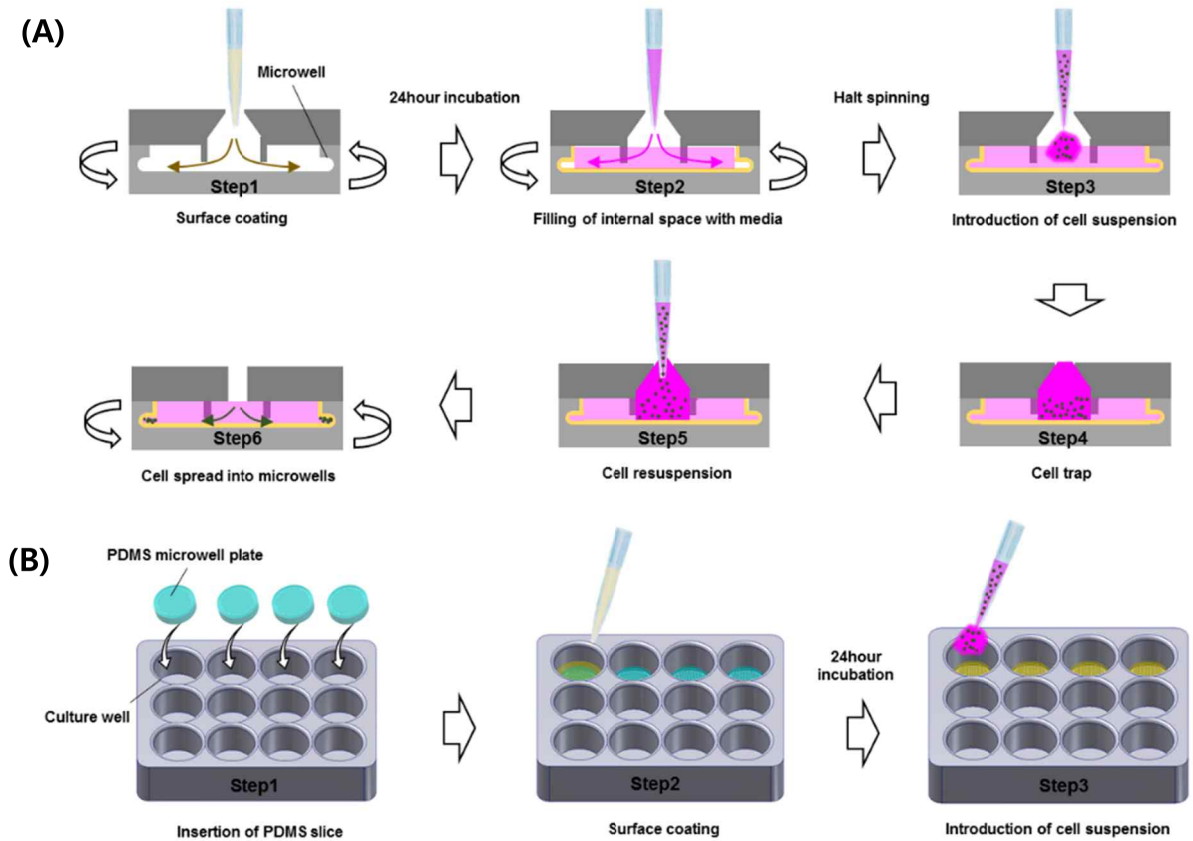
(A)
Microwell
Step1
Surface coating
24hour incubation
Step2
Filling of internal space with media
Halt spinning
Step3
Introduction of cell suspension
Step4
Cell trap
Step5
Cell resuspension
Step6
Cell spread into microwells
(B)
PDMS microwell plate
Culture well
Step1
Insertion of PDMS slice
Step2
Surface coating
24hour incubation
Step3
Introduction of cell suspension

Fig. 3.3.2 Spheroid formation procedure. (A) Experimental steps for CMS formation method are composed of six steps: Step 1: Coat the internal surface with pluronic copolymer solution as rotating the platform at ~4000 RPM. Step 2: After 24 hours of incubation, fill up the pluronic coated surface with media as rotating the platform at 3000 RPM. Step 3: Stop the spinning and introduce cell suspension. Step 4: Once cells are bounded inside the conical inlet, Step 5: re-suspend it to provide even distribution. Step 6: Rotate the platform to spread the cells into microwells. (B) Experimental steps for WPS formation method are composed of three steps: Step 1: Insert circular PDMS slices containing arrays of 200 μm cylindrical microwells into each culture well. Step 2: Introduce pluronic copolymer solution to each culture well containing PDMS slice to coat the surface. Step 3: After 24 hours of incubation, introduce cell suspension.

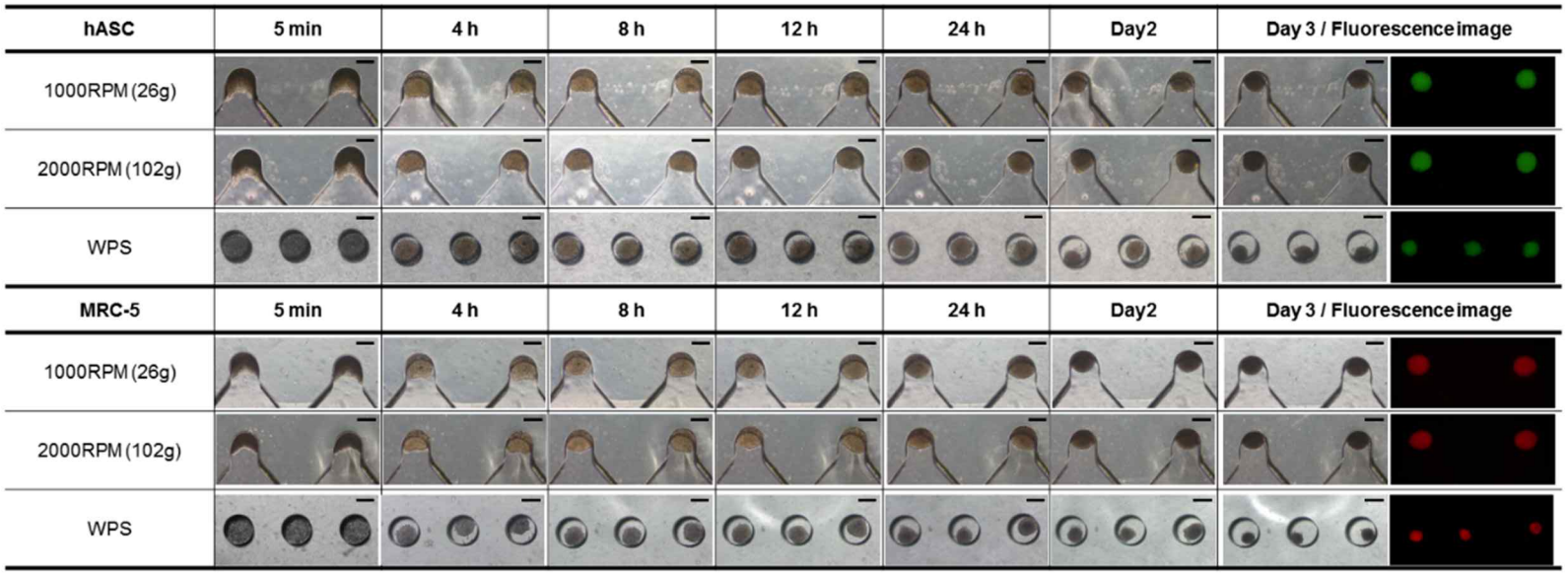

Fig. 3.3.3 Time lapse images of spheroid formation. Images were taken in seven different time intervals; 5 min, 4 h, 8 h, 12 h, 24 h, Day2, and Day3. Cell aggregate initially seated in reversed U-shape with CMS formation method, while completely packed with WPS formation method got smaller over time. Scale bar is 250 μm.

(A) hASC

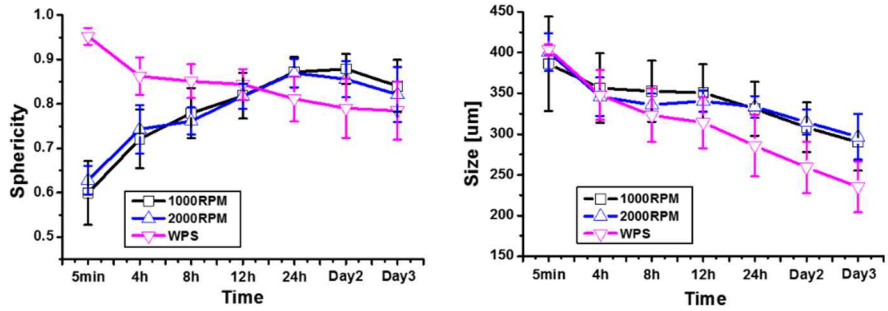

(B) MRC-5

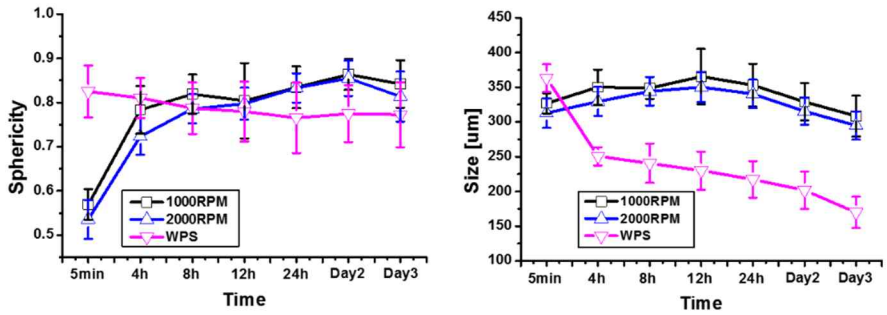

Fig. 3.3.4 Sphericity and size change over time. Spheroids formation process for (A) hASC and (B) MRC-5 by CMS formation method with two different centrifugal forces creating hypergravity conditions of 26 G and 103 G respectively and WPS formation method was examined. Change tendencies for sphericity and size were similar for both hypergravity conditions, while those for WPS formation method were different from them as sphericity decreases with WPS formation method but increases with CMS formation method over time. Degree of the size reduction due to cell aggregation was much higher with WPS formation method compared to CMS formation method.

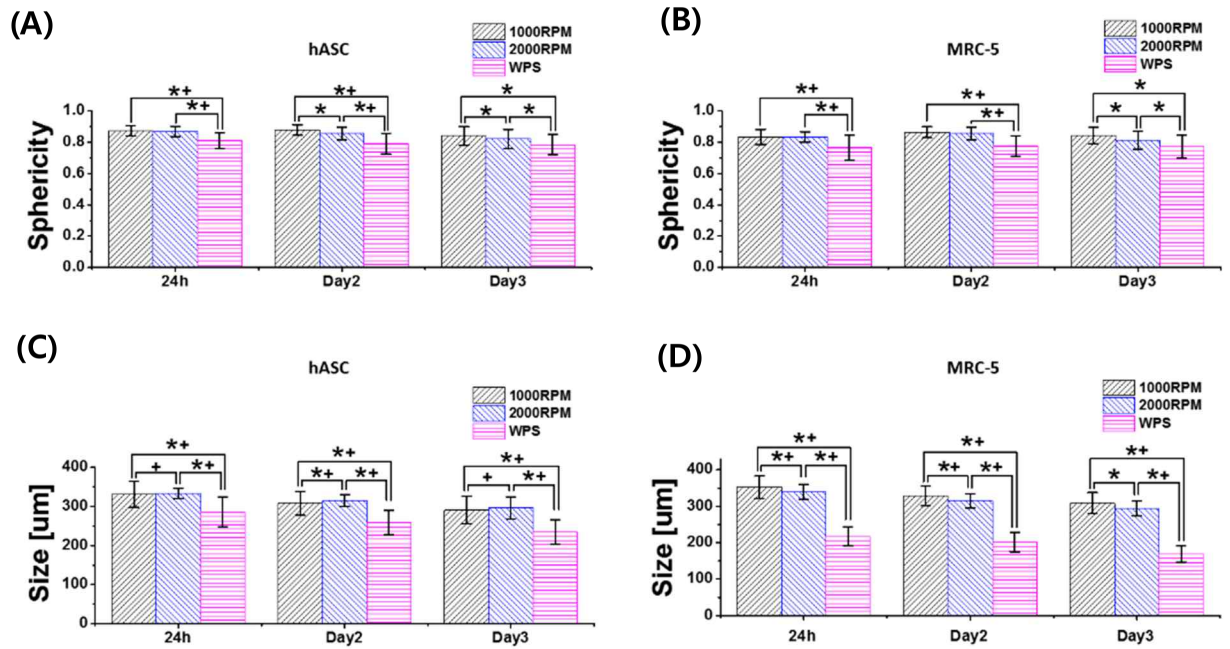

Fig. 3.3.5 Statistical analysis for sphericity and size. Sphericity and size variations at 24h, Day2, and Day3 for (A, C) hASC and (B, D) MRC-5 were compared and analyzed. Mean sphericity was significantly greater with CMS formation method compared to

formation method for all three time durations for both cell types. However, in CMS formation method, the higher RPM undermined sphericity compared to the lower RPM from Day2 for hASC and from Day3 for MRC-5. Standard deviations for sphericity which may indicate shape consistency was significantly greater with CMS formation method compared to WPS formation method at 24h and Day2, but such effects disappears at Day3 for both cell types. Degree of size reduction was significantly greater with WPS formation method compared to CMS formation method despite of the same well sizes designed for both WPS and CMS formation method. While no significant effects on size reduction by different hypergravity conditions were found for hASC, 2000 RPM significantly reduces size compared to 1000 RPM for MRC-5. Standard deviations for size which may indicate size consistency were significantly less for spheroids under 2000 RPM compared to those under 1000 RPM and WPS formation method at all three hour durations, suggesting that the level of hypergravity conditions has positive effects on size consistency.

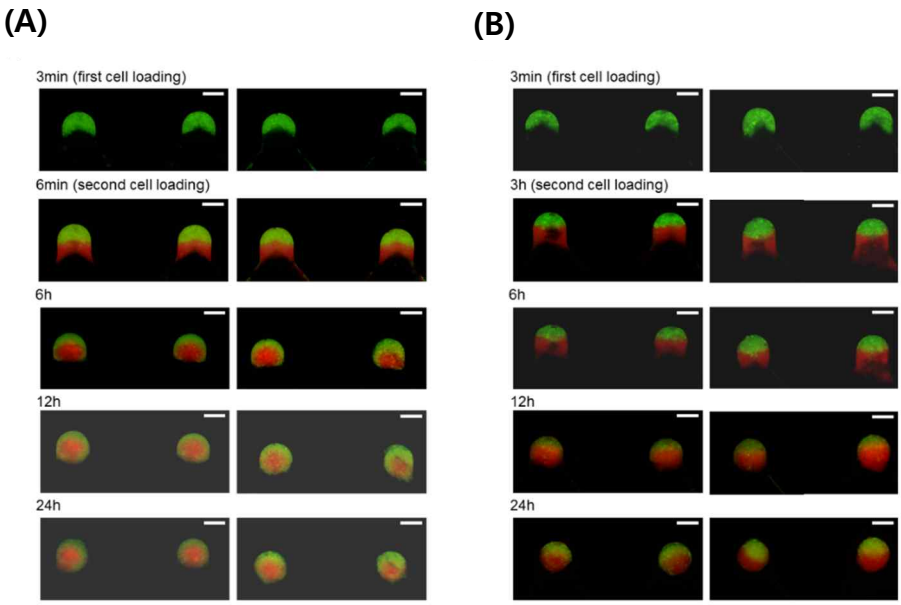

Fig. 3.3.6 Janus and concentric spheroid. hASC (green) and MRC-5 (red) were co-cultured by CMS formation method. Sequential seeding of each cell type in 3min and 2 h interval created spheroids in (A) concentric shape by enclosing one cell type by the other and (B) Janus shape by the two cell types equally sharing the spheroid to have two distinct parts respectively. Scale bar is 250 μm.

(A)

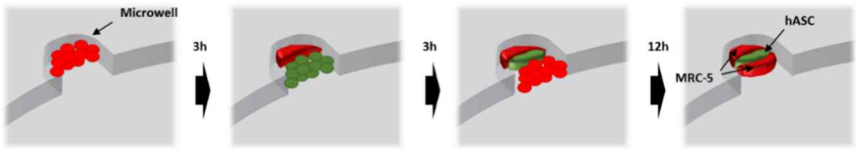

(B)

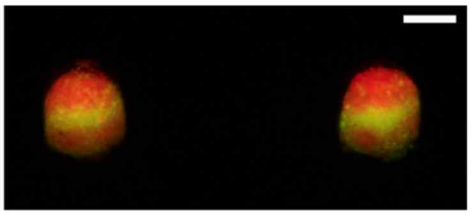

Fig. 3.3.7 Sandwich spheroid. (A) The schematic illustration for creating sandwich shape co-culture model by CMS formation method with the sequential seeding procedure in three different time steps of 3 h intervals. hASC (green) and MRC-5 (red) were accumulated one by one to have three distinct parts. (B) Actual appearance of sandwich spheroid after 12 h of culture. Scale bar is 250 μm.

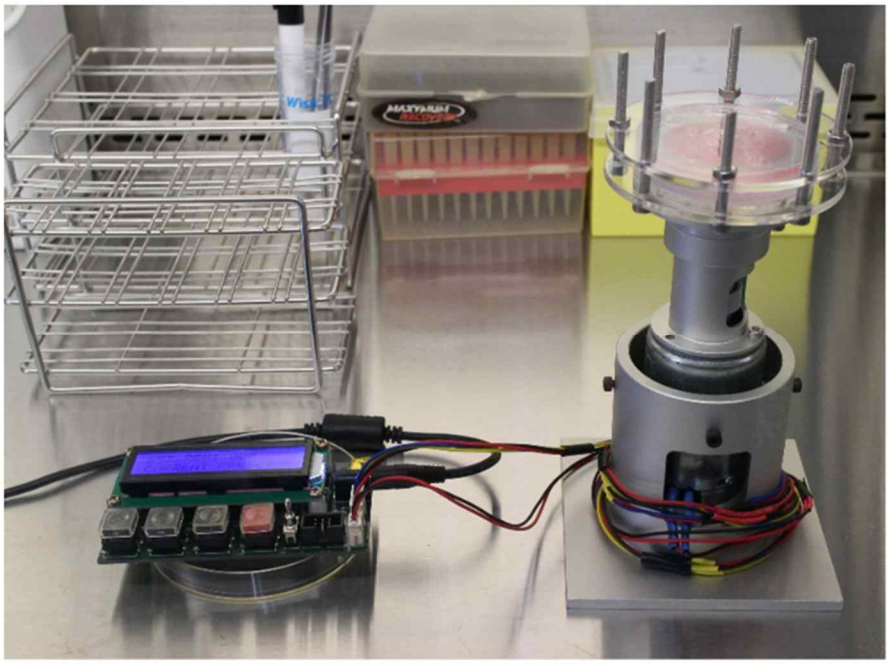

Fig. 3.3.8 Real feature of centrifugal microfluidic-based spheroid (CMS) culture system used in the experiment.

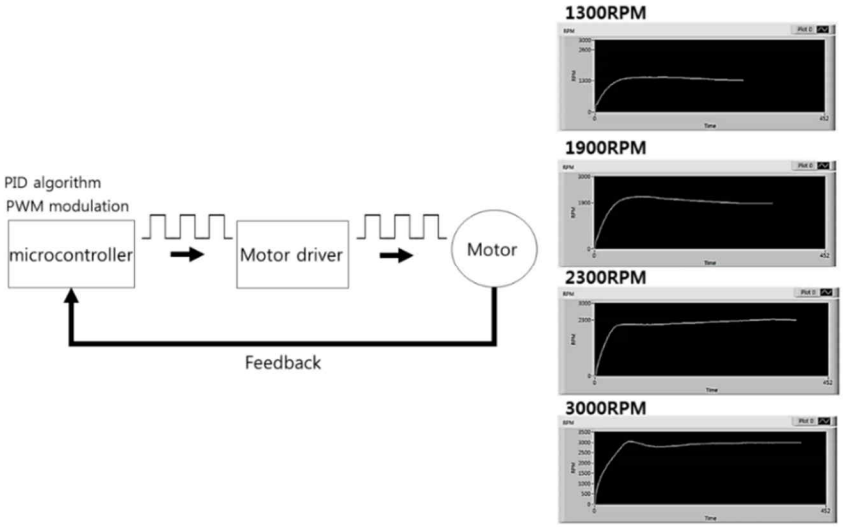

Fig. 3.3.9 Motor controller development by encoding proportional-integral-derivative (PID) algorithm based on pulse width modulation (PWM) technique into microcontroller unit (Atmega128, Atmel Co.). PWM modulated digital signal from microcontroller is transferred to H-bridge motor driver (DRV 8842, Texas Instrument) which is necessary to determine the direction of the motor rotation and finally transferred to motor power line. Feedback pulses from encoder installed in motor into microcontroller were counted to calculate current rotational speed and to apply PID algorithm that adjusts the speed to the target speed. Speed regulation was visualized by Labview program (National Instruments, Austin, Texas) and confirmed its proper regulation from low to high.

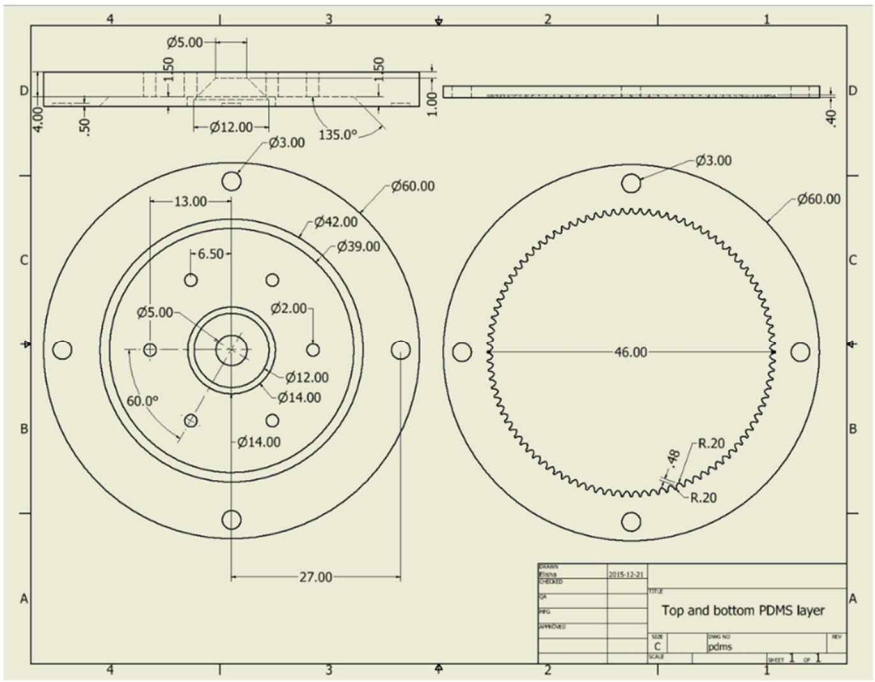

Fig. 3.3.10 Dimensions of top layer (left) and bottom layer (right) of the CMS microchip.

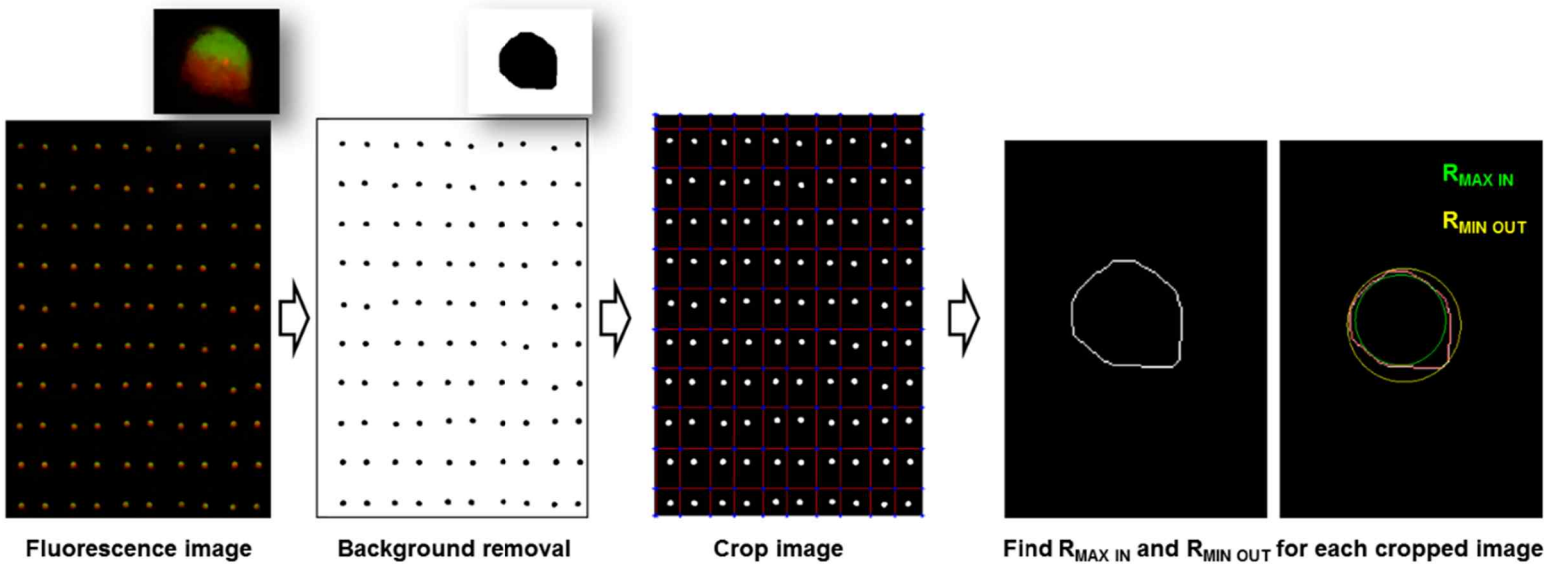

Fig. 3.3.11 Image processing algorithm for sphericity calculation

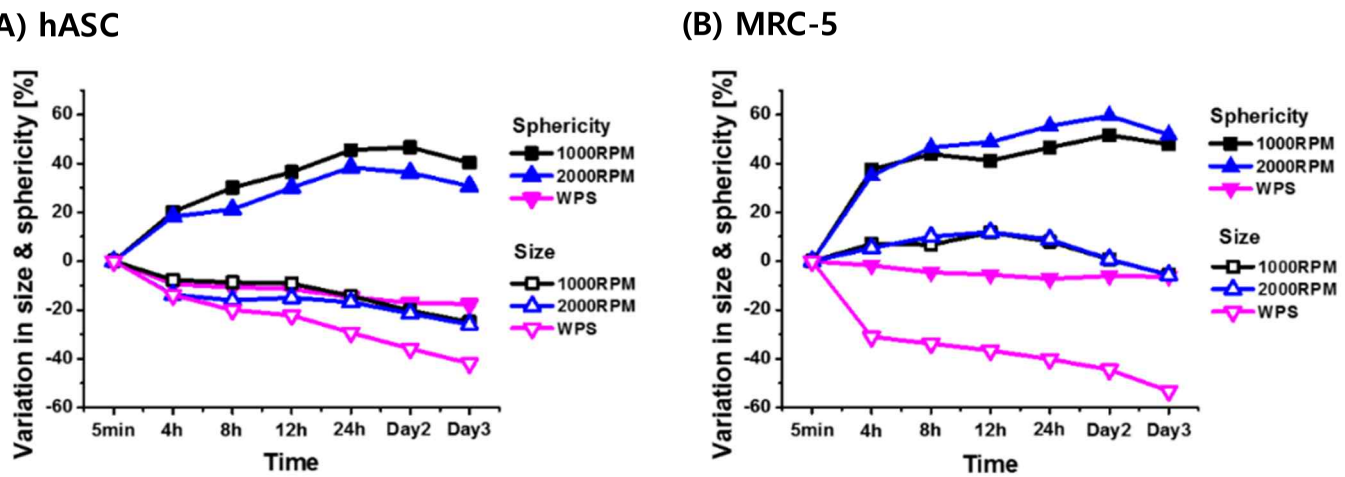

Fig. 3.3.12 Percent variations in size and sphericity for (A) hASC and (B) MRC-5. Mean values were taken from Fig. 4 and normalized by initial measurement at 5 min for each condition to calculate percent values. Percent variations for sphericity of the spheroids created by CMS method were on positive side with increasing manner, while those by WPS method were on negative side with decreasing manner along with size variations

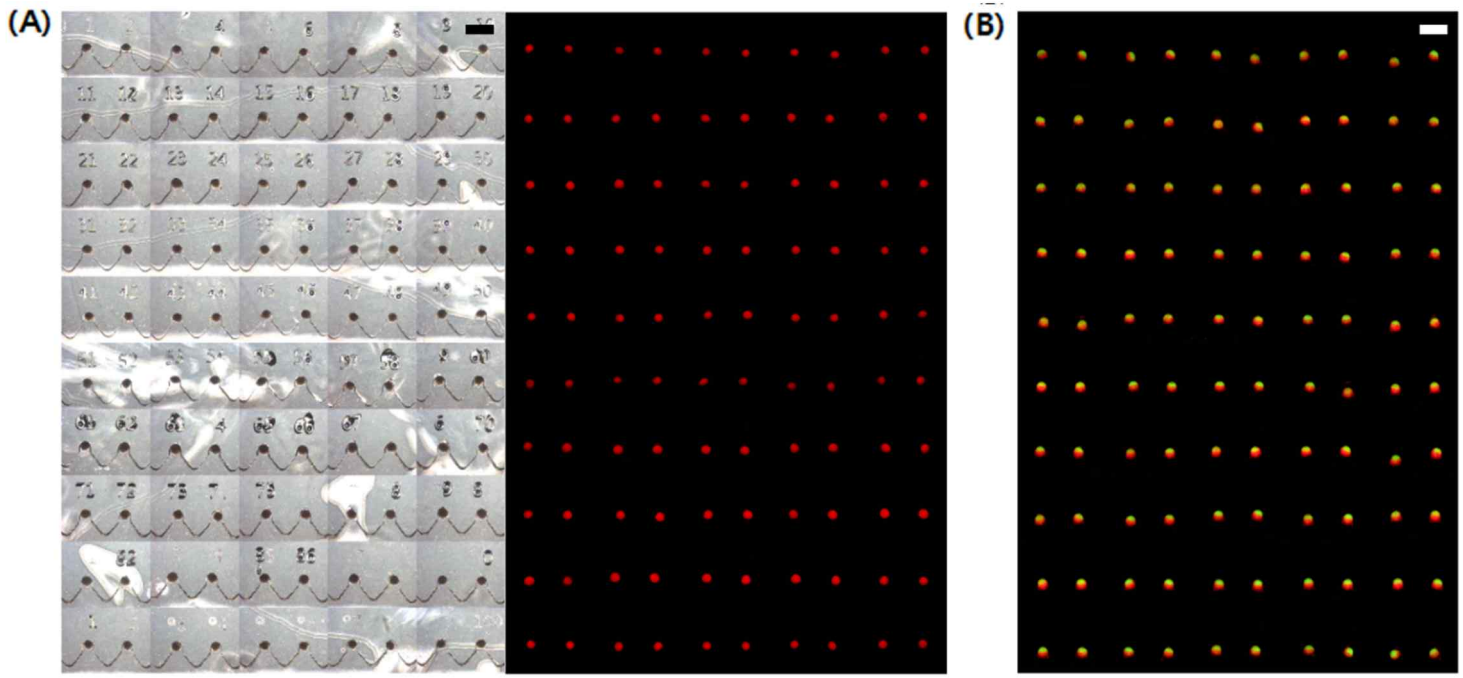

Fig. 3.3.13 (A) Single cell type spheroids of MRC-5 and (B) Janus spheroids created by CMS formation method under hypergravity condition of 102 G (2000 RPM) for 48 h and 12 h respectively. Scale bar is 1mm

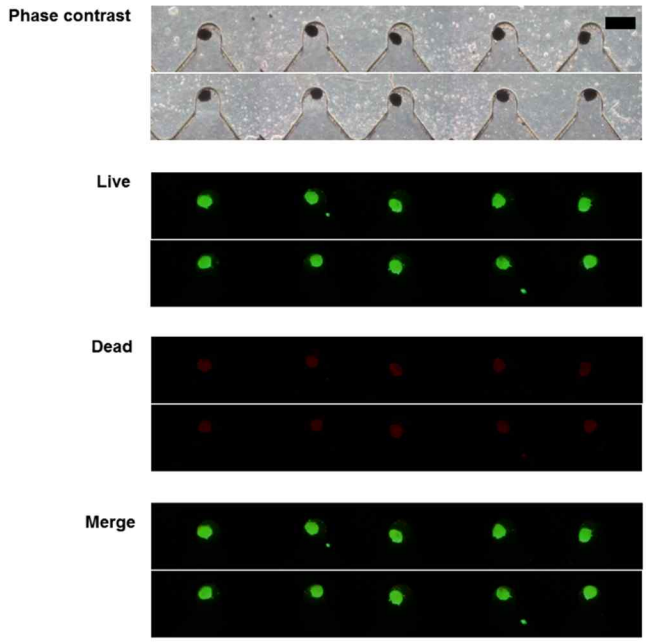

Fig. 3.3.14 Live/Dead assay at Day 7. Scale bar is 250 μm

Table 3.3.1 Summary of sequential seeding procedure for co-culture spheroid by CMS formation method. Resultant feature of co-culture models can be seen in Fig. 3.3.6 and Fig. 3.3.7.

	hASC	MRC-5	Time interval
Concentric	2.5 x 10^5 cells	4.0 x 10^5 cells	3 min
Janus	2.5 x 10^5 cells	4.0 x 10^5 cells	3 h
Sandwich	1.5 x 10^5 cells	3.0 x 10^5 cells	3 h

3.4 A study on adipose-derived stem cells adaptions to hypergravity environment [133]

Most biological studies have been limited to investigation of cellular responses under 1[G] environment assuming that human cells are adapted to Earth's gravitational force (G). However, considering that the culture environment (e.g. scaffold, uniaxial strain) greatly influences cell growth and differentiation particularly for stem cells, a study of cell behavior under different G environment may provide new perspectives in biomedical research. In this aspect of view, centrifugal fluidic system is one of the most appropriate biological tools to use for the described study as it is capable of generating wide ranges of artificial gravitational forces by controlling either rotational speed or channel geometries. For the experiment, human adipose-derived stem cells (hASCs) which are one of the promising types of stem cells in regenerative medicine was chosen. Under 86[G], cell morphology, proliferation, and gene expressions were quantitatively analyzed to characterize the effects of different G environment on the behavior of hASCs.

3.4.1 Introduction

Although human body can be exposed to diverse levels of acceleration other than Earth's gravitational force (1G) in their daily lives, most biological studies have been limited to investigation of cellular responses under 1[G] environment. Riding accelerated automobiles or roller coaster in an amusement park, for example, accompany physiological influences such as rise in heart rate [134].

Astronauts riding on a space shuttle, in particular, experience excessive acceleration up to 4G during space launch, which causes sudden disperse of blood away from brain to lose consciousness for the person who are not trained for high G condition [135]. However, these are all temporary changes by short term exposure to hypergravity, which might be different from the change by long term adaptations. For the long term adaptations, microgravity effects are well known compared to the hypergravity effects as spaceflight duration generally lasts for several days to months. According to National Space Biomedical Research Institute (NSBRI), once the astronauts reach to the space and begin to adapt to the life of weightlessness, they experience critical changes in their body systems including puffy face and smaller leg due to body fluid redistribution [136] and weakening of bones and muscles due to significant decrease in loading [137]. In case of human cardiovascular system responsible for adequate circulation of oxygenated blood throughout the entire body, the size of heart gets smaller since strength of blood pulling toward brain against Earth's gravitational force is no longer necessary in the state of zero gravity and therefore the heart does not have to work as hard as it was used to be [138], meaning adaptation to different G environment may create different physiological characteristics.

In previous research, a number of hypergravity experiments have been carried out using conventional centrifuge. However, they mostly attempted to provide short term hypergravity effects or could not properly replicate different G environment *in vitro*. A. Tschopp et al. has evaluated hypergravity effects on cell proliferation with five different cells (Hela cells, fibroblast, SGS-3 cells,

FBU 3b, and lymphocytes) during 48 hours exposure to 10[G], which resulted in an enhancement of cell growth while no morphological change has been found [139]. W. Hertl et al. also investigated cellular responses with kidney cells under high gravitational forces, but with shear stress generated due to cell culture plate positioned parallel to the rotating arm [140]. Recently, neuronal cells and mesenchymal stem cells were investigated with 1 and 3 hours hypergravity treatments respectively using the same centrifuge system composed of four large rotating arms [118, 119]. In addition, endothelial cells have been another cell type that is extensively explored under hypergravity condition, but the experimental results largely conflicts to each other due to inconsistent protocols used for the stimulation [141].

For the experiment, a portable centrifugal cell culture system (Fig. 3.4.1A) that is able to provide gravity conditions such that the force acts upright was developed [142]. Using this experimental platform, cellular adaptation has been investigated with human adipose-derived stem cells (hASCs), which has great potentials for use in regenerative medicine [143], considering that stem cells, which are not yet functional cell types and undergo environmental cue-dependent differentiation [144-146], could be the most suitable subject to study cell adaptations to different G environments. hASCs were continuously exposed to the defined G force during their whole transition from growth to differentiation. Cell morphology, proliferation, and gene expressions were analyzed under 86 [G] and compared with such parameters resulted from 1 [G] culture to quantitatively characterize the effects of the different G environments on the behavior of hASCs.

3.4.2 Materials and Methods

Cell culture

hASC (PCS-500-011, ATCC, VA, USA) was cultured at 36.5°C in 5% CO_2 atmosphere in Dulbecco's Modified Eagle's Medium (DMEM, ATCC 30-2002, ATCC) supplemented with 10% fetal bovine serum (FBS, ATCC-SCRR-30-2020, ATCC) and 1% Antibiotic-Antimycotic (Gibco 15240-062, Thermo Fisher Scientific, Waltham, MA, USA). Chondrogenesis was induced to when hASC confluency reached to greater than 90% using Chondrocyte Differentiation Tool (PCS-500-051, ATCC, VA, USA).

PDMS/glass chip fabrication and preparation

A single polydimethylsiloxane (PDMS) rectangular channel (10mm in length, 4mm in width, and 4mm in height) was replicated from a plastic master made by 3-dimensional printer (3D Edison, Lokit, Korea) using replica molding technique [147]. The channel was then bonded to a cover glass by an oxygen plasma treatment.

Two holes for inlet and outlet respectively at each end of the channel were bored to pass through side edges (Fig. 3.4.2) in order to prevent leakage of media inside the channel when the glass surface is vertically placed at the centrifugal system for the hypergravity experiment.

The glass surface was then coated with 4% gelatin in Dulbecco's Modified Eagle Medium (Invitrogen, Carlsbad, CA, USA) supplemented with 10 % fetal

bovine serum (FBS) and 5 μg/mL of 0.5% Gentamicine (PCS-999-025, ATCC, VA, USA) and Penicilline (PCS-999-002, ATCC, VA, USA) to seed the cell. The PDMS/glass chip was incubated at 37 °C and 5% CO_2 for 24 hours for the cell attachment prior to hypergravity experiment.

Centrifugal fluidic system development

A mini centrifugal fluidic system that can be operated inside the incubator was developed for hypergravity experiment. The rotating platform on the top was mechanically coupled with 24V DC encoder motor and a speed controller was developed to regulate the rotational speed of the motor from 200 to 5000 RPM constantly by applying a proportional-integral-derivative (PID) algorithm with pulse width modulation (PWM) technique (Fig. 3.3.9). The design feature of the rotating platform allows to perform the experiment under two different G environments at the same time as it has eighteen slots to contain PDMS/glass chips, six at inner and the rest at outer tracks (Fig. 3.4.3).

Hypergravity experiment

For the hypergravity experiment, hASCs were continuously exposed to the defined G environments during their whole transition from growth to differentiation by operating centrifugal fluidic system for 20 days, the first 10 days for growth and the other 10 days for differentiation. In order to observe growth change under different G environments, 1000 cells per each PDMS/glass chip were seeded to achieve confluency about 80~90% at day 10. For the first day of seeding (Day 0), all chips including control groups were

incubated at $37°C$ and 5% CO_2 for 24 hours with the glass surface at the bottom to allow cells to attach. At Day 1, the chips for hypergravity experiment were flipped to place the glass surface vertically upright and were arranged around the slots in the rotating platform in a way that the glass surface faces radially outward in order to provide proper upright gravity conditions such that Earth's gravity acts upon the living organisms. Control groups, on the other hand, were kept in the incubator without flipping and therefore hASCs in control groups were grown under 1[G] environment. The centrifugal fluidic system containing the PDMS/ glass chips was placed in the incubator with its speed controller equipped outside (Fig. 3.4.1B). The change of cell morphology and proliferation at a specific G environment defined by the rotational speed and the radial distance of each slot from the rotating axis have been observed during 10 days. At Day 10, chondrogenic differentiation was induced and gene expression has been monitored.

Viability and cytoskeletal analysis

Cell viability and actin filament structures were consistently monitored by staining with Live/Dead Viability/Cytotoxicity Kit, for mammalian cells (Invitrogen, Cat. #L-3224) and ActinGreen 488 Ready Probes Reagent (Invitrogen, Cat. R37110) respectively by following the manufacture's protocol.

Cell count

In order to examine cell proliferation, cell numbers during first 10 days of hypergravity experiment was measured by manually marking red dots on phase

contrast images (10x) of cells and processed with ImageJ software to automatically count the red dots (Fig. 3.4.4).

Oil red O staining

At Day 20, cell differentiation was assessed by safranin O staining (Sciencell, Cat. 8348) by following the manufacture's protocol.

3.4.3 Results

With phase contrast images, it was difficult to discern morphogical changes between control groups and hASCs grown under hypergravity condition of 86 [G] (Fig. 3.4.5). However, F-actin staining has shown cytoskeletal changes which would accompany morphological changes. Actin synthesis has been significantly increased by Day 10 with the hypergravity condition compared to control groups, which may affect differentiation process [148]. Under hypergravity condition, areas of cell body became larger and F-actin staining also became brighter compared to control groups which could be due to flattening of the cell body by upright gravity forces (Fig. 3.4.6).

Growth rate has been significantly increased with hypergravity conditions compared to control groups (Table 3.4.1).

The number of oil droplet-filled cells was greater with hypergravity conditions compared to control groups (Fig. 3.4.7), which could be simply due to increased proliferation regardless of the level of differentiation. Therefore,

SafarinO staining might be inappropriate for quantifying chondrogenic differentiation in this study where growth rate is also influenced by the environmental cue. However, considering that entire cells expressed orange-red colors (Fig. 3.4.7), hypergravity condition does not at least down-regulate chondrogenic differentiation.

3.4.4 Discussion

Morphology and proliferation of hASCs were turned out to be significantly altered by long term adaptations to hypergravity conditions. Quantification of gene expressions with polymerase chain reaction (PCR) analysis might be necessary to quantify chondrogenic differentiation instead of visual examination using SafarinO staining since growth rate is also affected by hypergravity conditions. As ASCs are abundantly available from readily accessible subcutaneous adipose tissue and has multipotent properties modulated by mechanical stimuli [143, 149], various mechanical stimulations have been applied to study their cellular responses including compressive force [150], equiaxial and uniaxial cyclic stretch [151, 152], and cyclic shear stress [153, 154]. While those mechanical stimulations were found to down-regulate either osteogenic or adipogenic differentiation, the results show that hypergravity conditions promote cell growth and seemed not at least down-regulate chondrogenic differentiation.

Effects of hypergravity condition on cell proliferation shown in this study might be useful in production of antibiotics, drugs, vaccines, and etc. where achieving high throughput is essentially necessary. Moreover, considering that

multiple types of mechanical stimulations are being used in cell biology including stem cell differentiation [155], the centrifugal fluidic system that enables hypergravity experiment may become one of important experimental platforms in cell research.

Present research needs to be further advanced by conducting quantitative analysis on cell morphology, proliferation, and differentiation under different hypergravity conditions, for example with statistical analysis on cell growth, cell heights, and gene expressions respectively.

3.4.5 Conclusion

This study aimed to investigate long term adaptations of hASCs to hypergravity conditions by developing a portable centrifugal fluidic system. hASCs were continuously exposed to hypergravity conditions of 86 [G] in a vertical direction to the cell bodies during their whole transition from growth to differentiation. Cell morphology, proliferation, and differentiation were qualitatively examined by image analysis. As a result, hypergravity conditions turned out to significantly alter cellular behavior of hASCs by flattening the cell body, increasing growth rate, and presumably up-regulate chondrogenic differentiation. Considering that mechanical stimulation plays an important role in studying various types of cell not limited to stem cells, the centrifugal fluidic system developed in this study for hypergravity experiment may become one of universal platforms in biological and biomedical research.

Fig. 3.4.1 A portable centrifugal cell culture system. (A) Eighteen slots, six at inner and the rest six at outer track to contain PDMS/glass chips. Speed controller developed to regulate rotational speed is shown below. (B) Incubator with the speed controller attached to the side.

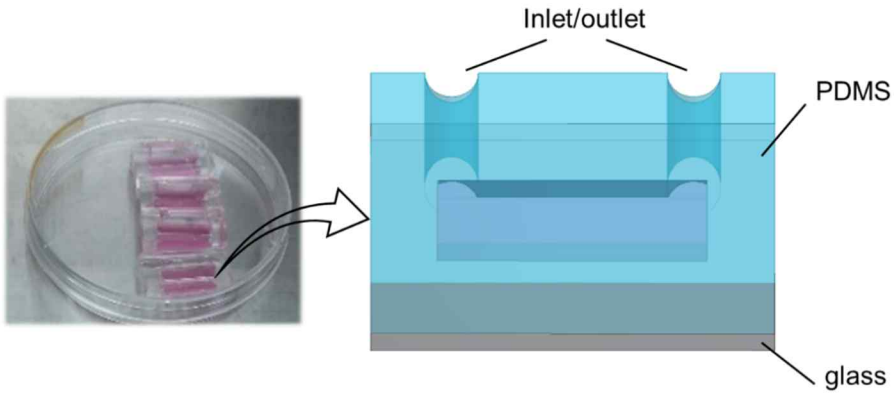

Fig. 3.4.2 PDMS/glass chip. A top PDMS layer composed of a single rectangular channel (10mm in length, 4mm in width, and 4mm in height) was bonded to a cover glass by an oxygen plasma treatment. Two holes were penetrated at the edge of the top layer to the channel for cell seeding and media exchange.

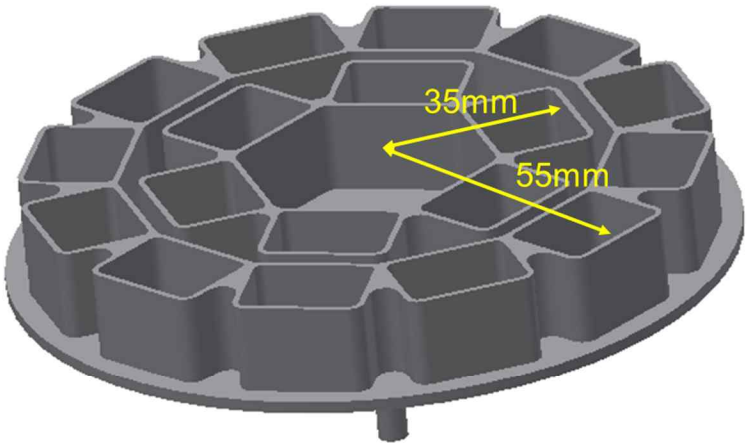

RPM	[G]	R [mm]
300(31rad/s)	3	33
600(63rad/s)	13	33
900(94rad/s)	30	33
1200(126rad/s)	53	33

RPM	[G]	R [mm]
300(31rad/s)	5	53
600(63rad/s)	21	53
900(94rad/s)	48	53
1200(126rad/s)	86	53

Fig. 3.4.3 G environments created at each slot. Rotational speed and radial distances of the slots determine the level of hypergravity conditions.

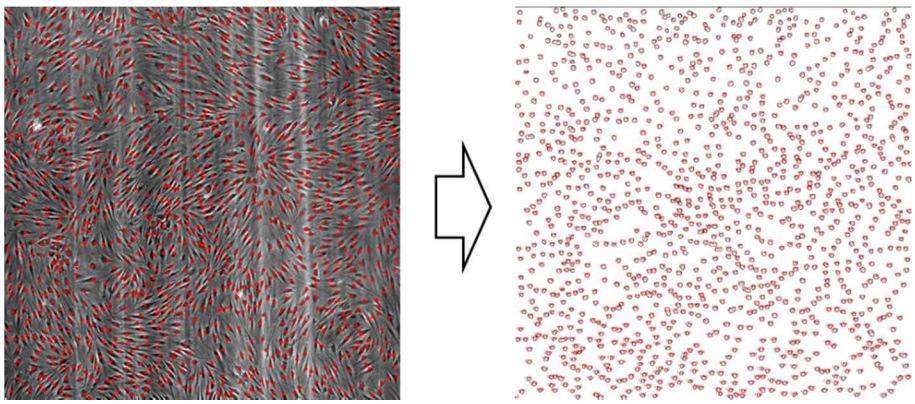

Fig. 3.4.4 Image processing for cell count. Red dots were manually marked at phase contrast images, which was then processing with ImageJ software to automatically count the red dots.

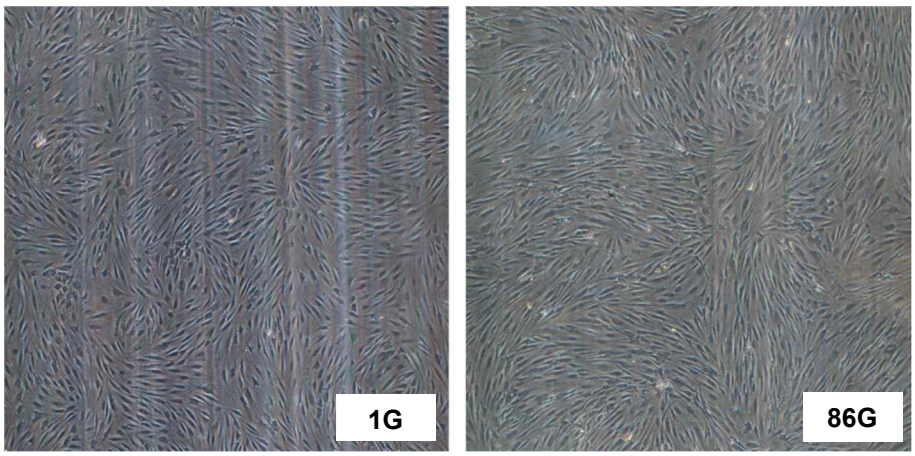

Fig. 3.4.5 Phase contrast images of cells. No morphological difference seen in the images for cells cultured under low and high G environment.

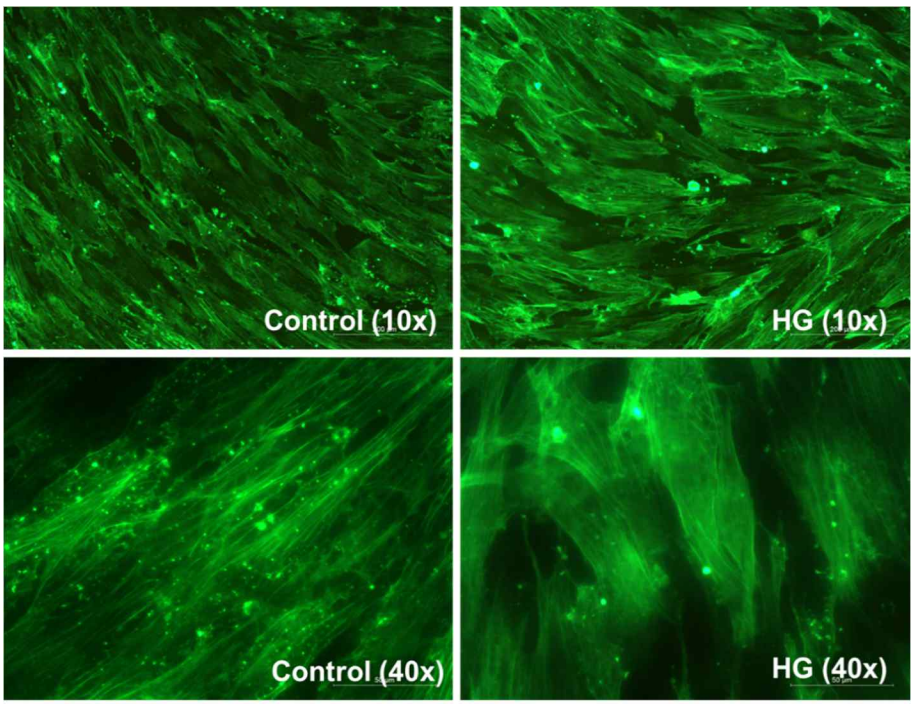

Fig. 3.4.6 F-actin filament staining. Actin synthesis seems to significantly increased by Day 10 with the high G environment (HG) as F-actin staining became brighter compared to control groups.

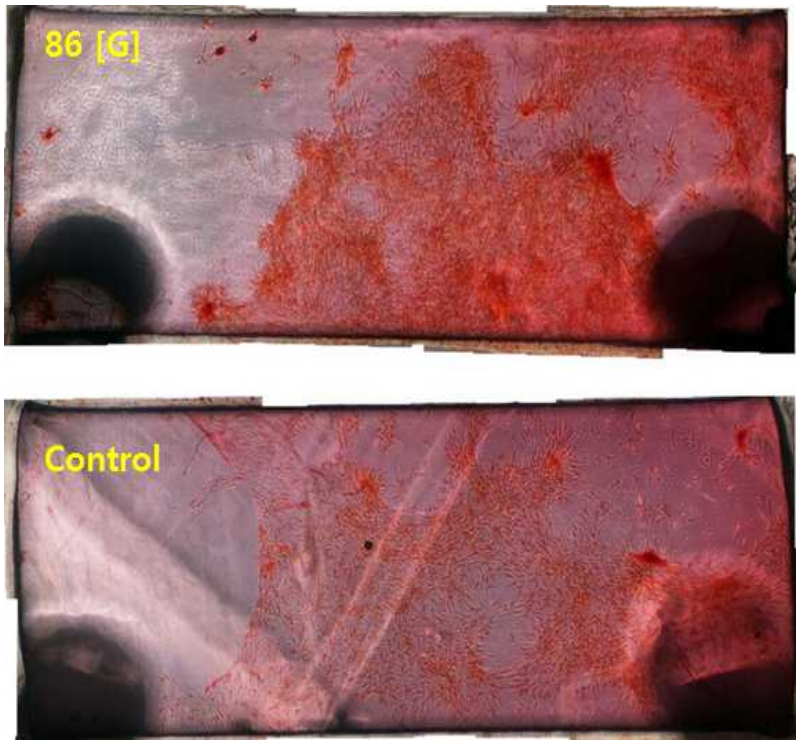

Fig. 3.4.7 Safranin O staining for chondrogenic differentiation analysis. Intensity of red-orange color shows the level of differentiation and it was a lot more greater for cells cultured under 86 [G], but it could be attributed to facilitated cell growth by hypergravity condition and simply due to more number of cells exist in the chip.

Table 3.4.1 Percentage of cell growth was calculated. Twelve PDMS/glass chips for control groups and high G environment (HG) respectively were examined. Growth rate has been significantly increased with hypergravity conditions compared to control groups, and it was the greatest at the first three days.

Control	**Growth rate**			**HG**	**Growth rate**		
	Day1~3	**Day3~5**	**Day1~5**		**Day1~3**	**Day3~5**	**Day1~5**
C1	79%	-9%	62%	**R1**	72%	79%	209%
C2	41%	-7%	32%	**R2**	122%	-5%	110%
C3	31%	-5%	24%	**R3**	140%	7%	156%
C4	70%	4%	77%	**R4**	48%	86%	175%
C5	76%	8%	91%	**R5**	69%	-2%	66%
C6	58%	-7%	47%	**R6**	85%	56%	189%
C7	82%	4%	90%	**R7**	79%	7%	93%
C8	75%	5%	84%	**R8**	111%	20%	153%
C9	85%	-10%	67%	**R9**	127%	46%	231%
C10	65%	-9%	51%	**R10**	66%	27%	112%
C11	59%	-32%	9%	**R11**	66%	49%	147%
C12	36%	51%	106%	**R12**	152%	44%	264%
Total	**62%**	**-3%**	**57%**	**Total**	**91%**	**28%**	**146%**
Mean	**63%**	**0%**	**62%**	**Mean**	**95%**	**35%**	**159%**

Chapter 4.

Conclusion and Perspective

A centrifugal force-based fluidic system has distinct advantages compared to conventional fluidic systems, leading to a number of its biomedical applications. Unlike other bulky fluidic systems, centrifugal force-based fluidic system can manipulate fluids simply by geometric channel designs and rotational speeds, enabling to develop small, light, and compact systems. This dissertation focuses on the design, fabrication, evaluation, and application of a centrifugal force-based fluidic system based on both macro- and micro-engineering disciplines to develop the system qualified for either diverse clinical environments or *in-vitro* biological experimental setup.

In Chapter 2.1, the product development process for a portable smart all-

in-one cardiopulmonary circulatory support device (CCSD) is described. Most CCSD currently available in market are bulky and uncomfortable to use especially in the intensive care unit (ICU) environment. Accordingly, this study aimed to develop a portable and cost-effective smart all-in-one CCSD that is capable of interactively and autonomously operating in accord with various indications of patients. By integrating all the necessary components including core sensor modules for monitoring patient status into one single device, prototypes of smart all-in-one CCSD with preliminary performance result of pump driver and control unit on a mock circulation loop were presented [27].

In Chapter 2.2, evaluation of hemolytic characteristics of centrifugal blood pump designed based on computational fluid dynamics (CFD) is described. Development of a low hemolytic centrifugal blood pump is a key for providing undamaged blood to patients during cardiopulmonary support. Hemolytic characteristics of the pump depend on its design, materials, and manufacturing processes. Design and manufacturing optimizations encompass very challenging problems to achieve low levels of hemolysis. In this study, hemolytic characteristics of multiple types of centrifugal blood pumps designed based on computational fluid dynamics (CFD) simulation study were evaluated. Hemolysis test was performed in accordance with American Society of Testing and Materials (ASTM) standards by preparing a circulation loop consisting of blood bag, polyvinyl chloride medical tubing, flowmeter, clamp, pressure sensors, water bath, and thermometer. 450 mL or 500 mL of fresh blood obtained from normal swine was circulated for 6 hours with a flowrate of 5 L/min at a pressure of 100 mmHg. Normalized indices of hemolysis (NIH) was

determined by measuring free hemoglobin in plasma every hour. By incorporating pivot bearing, NIH value less than 0.005g/100L which was comparable to that of commercial product was able to be stably achieved. Developed prototypes for the centrifugal blood pump were also integrated to the smart all-in-one CCSD for *in-vivo* evaluation and the pivot bearing-based centrifugal blood pump resulted in promising free plasma hemoglobin (freeHGB) measurement during 6 hours of operation comparable to that resulted from the commercial product [29].

In Chapter 2.3, evaluation of drug sequestration in the extracorporeal oxygenation (ECMO) circuit, one of representative model of CCSD, is described. The influence of the elements of ECMO circuit on drug sequestration was quantified by focusing on the interactions between materials and drugs. Tubing of three different brands (Tygon/Maquet/Terumo) and oxygenators of two different brands (Maquet/Terumo) were used. Drugs included dexmedetomidine, meropenem, and heparin which were dissolved in deionized water. Tubing was cut into ~7 cm sections and allowed drug solutions enclosed inside by clamping both ends. The oxygenator housing, gas membrane, and heat exchanger were dissected into ~1 g pieces and submerged into drug solutions. The experimental samples were then immersed in a water bath at 37°C for 1, 6, 12, and 24 h. After 24 h, the dexmedetomidine concentration was significantly reduced in all three types of tubing (<30.1%), the oxygenator heat exchanger from Maquet Inc. (41.8%), and the gas exchanger from Terumo Inc. (8.6%), while no significant losses were found for meropenem and heparin compared to the control group. The heparin concentration within the Maquet gas

exchanger, on the other hand, increased significantly compared to the control group at 1 and 12 h ($p<0.05$). The in-vitro study reveals that material selection is a vital part of ECMO development [43].

In Chapter 3.1, simulation study on fluid flow in rotating microchannel by Coriolis force is described. The Coriolis force has been of great interest to control the transversal flow that is critical for mixing or switching fluids in centrifugal microfluidics. Therefore, the variation in the Coriolis effect has been extensively investigated by varying the rotational speeds and the cross-sectional geometry of microchannels. However, the subject of such investigations has been limited to radially positioned microchannels even though channels can lie everywhere on the rotating platform with different arrangements. In this study, we use numerical methods to investigate the Coriolis effect resulting from the angular alignment (AA) and radial displacement (RD) of rotating microchannels. The analysis focuses on determining the contribution that different channel arrangements have in the deviation of parabolic velocity profiles, which is generally produced by the effective Coriolis force. We found that the flow can deviate even at a low rotational speed, where the Coriolis force is negligible, with an AA of up to 33% which is a sufficient amount for flow switching. Once the rotational speed reaches to the critical RPM, the flow deviates by an effective Coriolis force, but the deviation systematically varies with AA or RD. As the Coriolis force becomes more dominant with a high rotational speed, the deviation reaches a saturation point while flow rate is regulated by AA or RD, enabling the flow rate to remain low even at very high RPM, without reducing the deviation. The

variation in the Coriolis effect due to the different channel arrangements investigated in this study is believed to provide an essential basis to design and develop centrifugal microfluidic systems [68].

In Chapter 3.2, development of centrifugal force-based viscometer is described. Viscosity of the fluid is one of the key indicators in chemical and biological studies to represent fluidic conditions. However, commercially available viscometers are often expensive and time consuming to analyze large samples. Here, we developed a centrifugal microfluidic viscometer based on Poiseuille law and demonstrated its performance with samples with four different glucose concentrations [89].

In Chapter 3.3, development of centrifugal force-based cell spheroid formation method is described. In living tissue, cells exist in three-dimensional (3D) microenvironments with intricate cell-cell interactions. To model such cellular environment, various techniques for generating cell spheroids have been proposed and improved continually. However, previously reported methods still have limitations on the levels of uniformity, reproducibility, scalability, through-put, etc. Here, we present a centrifugal microfluidic-based spheroid (CMS) formation method for generating co-culture as well as mono-culture 3D spheroid in highly controlled manner. Circularly arrayed microwells were designed to allow even distribution of cells introduced at the center of a rotating platform and to provide identical hypergravity conditions at each well by centrifugal forces generated. Compared to the conventional well plate-based spheroid (WPS) formation method, CMS formation method significantly promotes sphericity and consistency for both size and shape with high

production yields. In addition to mono-culture spheroids, we successfully generated co-culture spheroids in concentric, Janus, and Sandwich shape using human adipose-derived stem cells (hASC) and human lung fibroblasts (MRC-5), demonstrating versatility of CMS formation method. The new method proposed for generating 3D spheroids is believed to become one of essential technologies in the field of 3D cell culture systems and we are also expecting to provide an innovative means to assess cellular responses including cell motilities in different hypergravity conditions [95].

In Chapter 3.4, study on cellular adaptation to hypergravity environment using centrifugal force-based platform is described. Most biological studies have been limited to investigation of cellular responses under 1[G] environment assuming that human cells are adapted to Earth's gravitational force (G). However, considering that the culture environment (e.g. scaffold, uniaxial strain) greatly influences cell growth and differentiation particularly for stem cells, a study of cell behavior under different G environment may provide new perspectives in biomedical research. In this aspect of view, centrifugal fluidic system is one of the most appropriate biological tools to use for the described study as it is capable of generating wide ranges of artificial gravitational forces by controlling either rotational speed or channel geometries. For the experiment, we have chosen human adipose-derived stem cells (hASCs) which are one of the promising types of stem cells in regenerative medicine. Under 86[G], cell morphology, proliferation, and gene expressions were quantitatively analyzed to characterize the effects of different G environment on the behavior of hASCs [133].

Described system development and evaluations are believed to become a key foundation for a wide range of centrifugal force-based biomedical applications for example to develop fully integrated and automated CCSD unsusceptible to pharmacokinetic variations, to develop small sample viscometer, to synthetic biology, to organoid study, to drug testing using high quality of mono- and co-culture spheroids generated based on CMS formation method, to study biological adaptations of multiple cell types to hypergravity conditions, etc.

References

[1] M. Tang, G. Wang, S.-K. Kong, and H.-P. Ho, "A Review of Biomedical Centrifugal Microfluidic Platforms," *Micromachines,* vol. 7, no. 2, pp. 26, 2016.

[2] A. C. Passaroni, M. A. Silva, and W. B. Yoshida, "Cardiopulmonary bypass: development of John Gibbon's heart-lung machine," *Rev Bras Cir Cardiovasc,* vol. 30, no. 2, pp. 235-45, Mar-Apr, 2015.

[3] I. S. Morgan, M. Codispoti, K. Sanger, and P. S. Mankad, "Superiority of centrifugal pump over roller pump in paediatric cardiac surgery: prospective randomised trial," *Eur J Cardiothorac Surg,* vol. 13, no. 5, pp. 526-32, May, 1998.

[4] I. Halaweish, A. Cole, E. Cooley, W. R. Lynch, and J. W. Haft, "Roller and Centrifugal Pumps: A Retrospective Comparison of Bleeding Complications in Extracorporeal Membrane Oxygenation," *ASAIO J,* vol. 61, no. 5, pp. 496-501, Sep-Oct, 2015.

[5] R. Saczkowski, M. Maklin, T. Mesana, M. Boodhwani, and M. Ruel, "Centrifugal pump and roller pump in adult cardiac surgery: a meta-analysis of randomized controlled trials," *Artif Organs,* vol. 36, no. 8, pp. 668-76, Aug, 2012.

[6] Y. Nose, "Design and development strategy for the rotary blood pump," *Artif Organs,* vol. 22, no. 6, pp. 438-46, Jun, 1998.

[7] J. Zhang, B. Gellman, A. Koert, K. A. Dasse, R. J. Gilbert, B. P. Griffith, and Z. J. Wu, "Computational and experimental evaluation of the fluid dynamics and hemocompatibility of the CentriMag blood

pump," *Artif Organs,* vol. 30, no. 3, pp. 168-77, Mar, 2006.

[8] R. Kosaka, T. Yada, M. Nishida, O. Maruyama, and T. Yamane, "Geometric optimization of a step bearing for a hydrodynamically levitated centrifugal blood pump for the reduction of hemolysis," *Artif Organs,* vol. 37, no. 9, pp. 778-85, Sep, 2013.

[9] T. Takano, S. Schulte-Eistrup, M. Yoshikawa, K. Nakata, S. Kawahito, T. Maeda, K. Nonaka, J. Linneweber, J. Glueck, A. Fujisawa, K. Makinouchi, M. Yokokawa, and Y. Nose, "Impeller design for a miniaturized centrifugal blood pump," *Artif Organs,* vol. 24, no. 10, pp. 821-5, Oct, 2000.

[10] J. Leme, J. Fonseca, E. Bock, C. da Silva, B. U. da Silva, A. E. Dos Santos, J. Dinkhuysen, A. Andrade, and J. F. Biscegli, "A new model of centrifugal blood pump for cardiopulmonary bypass: design improvement, performance, and hemolysis tests," *Artif Organs,* vol. 35, no. 5, pp. 443-7, May, 2011.

[11] N. Mendler, F. Podechtl, G. Feil, P. Hiltmann, and F. Sebening, "Seal-less Centrifugal Blood Pump with Magnetically Suspended Rotor: Rot-a-Flot," *Artificial organs,* vol. 19, no. 7, pp. 620-624, 1995.

[12] T. Nakazawa, K. Makinouchi, Y. Takami, J. Glueck, S. Takatani, and Y. Nose, "Modification of a pivot bearing system on a compact centrifugal pump," *Artif Organs,* vol. 20, no. 3, pp. 258-63, Mar, 1996.

[13] Y. Orime, M. Shiono, S. Yagi, T. Yamamoto, H. Okumura, K. Nakata, S. Kimura, M. Hata, A. Sezai, S. Kashiwazaki, S. Choh, N. Negishi, Y. Sezai, T. Matsui, and M. Suzuki, "Jostra Rota Flow RF-30 pump

system: a new centrifugal blood pump for cardiopulmonary bypass," *Artif Organs,* vol. 24, no. 6, pp. 437-41, Jun, 2000.

[14] J. P. Mueller, A. Kuenzli, O. Reuthebuch, K. Dasse, S. Kent, G. Zuend, M. I. Turina, and M. L. Lachat, "The CentriMag: a new optimized centrifugal blood pump with levitating impeller," *Heart Surg Forum,* vol. 7, no. 5, pp. E477-80, 2004.

[15] R. Roncon-Albuquerque, Jr., C. Basilio, P. Figueiredo, S. Silva, P. Mergulhao, C. Alves, R. Veiga, S. Castelo-Branco, L. Paiva, L. Santos, T. Honrado, C. Dias, T. Oliveira, A. Sarmento, A. M. Mota, and J. A. Paiva, "Portable miniaturized extracorporeal membrane oxygenation systems for H1N1-related severe acute respiratory distress syndrome: a case series," *J Crit Care,* vol. 27, no. 5, pp. 454-63, Oct, 2012.

[16] T. Fuehner, C. Kuehn, J. Hadem, O. Wiesner, J. Gottlieb, I. Tudorache, K. M. Olsson, M. Greer, W. Sommer, and T. Welte, "Extracorporeal membrane oxygenation in awake patients as bridge to lung transplantation," *American journal of respiratory and critical care medicine*, 2012.

[17] M. M. Hoeper, O. Wiesner, J. Hadem, O. Wahl, H. Suhling, C. Duesberg, W. Sommer, G. Warnecke, M. Greer, O. Boenisch, M. Busch, J. T. Kielstein, A. Schneider, A. Haverich, T. Welte, and C. Kuhn, "Extracorporeal membrane oxygenation instead of invasive mechanical ventilation in patients with acute respiratory distress syndrome," *Intensive Care Med,* vol. 39, no. 11, pp. 2056-7, Nov, 2013.

[18] R. Gorkin, J. Park, J. Siegrist, M. Amasia, B. S. Lee, J. M. Park, J. Kim,

H. Kim, M. Madou, and Y. K. Cho, "Centrifugal microfluidics for biomedical applications," *Lab Chip,* vol. 10, no. 14, pp. 1758-73, Jul 21, 2010.

[19] M. Grumann, A. Geipel, L. Riegger, R. Zengerle, and J. Ducree, "Batch-mode mixing on centrifugal microfluidic platforms," *Lab Chip,* vol. 5, no. 5, pp. 560-5, May, 2005.

[20] C. E. Nwankire, A. Venkatanarayanan, T. Glennon, T. E. Keyes, R. J. Forster, and J. Ducree, "Label-free impedance detection of cancer cells from whole blood on an integrated centrifugal microfluidic platform," *Biosens Bioelectron,* vol. 68, pp. 382-9, Jun 15, 2015.

[21] J. M. Park, M. S. Kim, H. S. Moon, C. E. Yoo, D. Park, Y. J. Kim, K. Y. Han, J. Y. Lee, J. H. Oh, S. S. Kim, W. Y. Park, W. Y. Lee, and N. Huh, "Fully automated circulating tumor cell isolation platform with large-volume capacity based on lab-on-a-disc," *Anal Chem,* vol. 86, no. 8, pp. 3735-42, Apr 15, 2014.

[22] R. Gorkin, S. Soroori, W. Southard, L. Clime, T. Veres, H. Kido, L. Kulinsky, and M. Madou, "Suction-enhanced siphon valves for centrifugal microfluidic platforms," *Microfluidics and nanofluidics,* vol. 12, no. 1-4, pp. 345-354, 2012.

[23] A. Lee, J. Park, M. Lim, V. Sunkara, S. Y. Kim, G. H. Kim, M. H. Kim, and Y. K. Cho, "All-in-one centrifugal microfluidic device for size-selective circulating tumor cell isolation with high purity," *Anal Chem,* vol. 86, no. 22, pp. 11349-56, Nov 18, 2014.

[24] Y. Ouyang, J. Li, C. Phaneuf, P. S. Riehl, C. Forest, M. Begley, D. M.

Haverstick, and J. P. Landers, “Multilevel fluidic flow control in a rotationally-driven polyester film microdevice created using laser print, cut and laminate,” *Lab Chip,* vol. 16, no. 2, pp. 377-87, Jan 21, 2016.

[25] F. Schuler, N. Paust, R. Zengerle, and F. von Stetten, “Centrifugal step emulsification can produce water in oil emulsions with extremely high internal volume fractions,” *Micromachines,* vol. 6, no. 8, pp. 1180-1188, 2015.

[26] S. Hosseini, M. M. Aeinehvand, S. M. Uddin, A. Benzina, H. A. Rothan, R. Yusof, L. H. Koole, M. J. Madou, I. Djordjevic, and F. Ibrahim, “Microsphere integrated microfluidic disk: synergy of two techniques for rapid and ultrasensitive dengue detection,” *Sci Rep,* vol. 5, pp. 16485, 2015.

[27] J. Park, D. A. Shin, J. S. Lee, M. C. Shin, J. C. Lee, and H. C. Kim, “Development of a smart all-in-one cardiopulmonary support system: preliminary performance of pump driver and control unit on a mock circulation loop,” 2015.

[28] G. Ailawadi, and R. K. Zacour, “Cardiopulmonary bypass/extracorporeal membrane oxygenation/left heart bypass: indications, techniques, and complications,” *Surg Clin North Am,* vol. 89, no. 4, pp. 781-96, vii-viii, Aug, 2009.

[29] J. Park, D. A. Shin, H. A. Shin, J. S. Lee, H. Kim, J. C. Lee, and H. C. Kim, “Hemolytic characteristics of a centrifugal blood pump developed for multi-purpose extracorporeal circulation system,” *APSAO 2016 conference*, 2016.

[30] N. Mendler, F. Podechtl, G. Feil, P. Hiltmann, and F. Sebening, "Seal-less centrifugal blood pump with magnetically suspended rotor: rot-a-flot," *Artif Organs,* vol. 19, no. 7, pp. 620-4, Jul, 1995.

[31] D. Xie, Y. Leng, F. Jing, and N. Huang, "A brief review of bio-tribology in cardiovascular devices," *Biosurface and Biotribology,* vol. 1, no. 4, pp. 249-262, 2015.

[32] T. Akamatsu, T. Tsukiya, K. Nishimura, C. H. Park, and T. Nakazeki, "Recent studies of the centrifugal blood pump with a magnetically suspended impeller," *Artif Organs,* vol. 19, no. 7, pp. 631-4, Jul, 1995.

[33] J. Leme, C. da Silva, J. Fonseca, B. U. da Silva, B. Uebelhart, J. F. Biscegli, and A. Andrade, "Centrifugal blood pump for temporary ventricular assist devices with low priming and ceramic bearings," *Artif Organs,* vol. 37, no. 11, pp. 942-5, Nov, 2013.

[34] A. D. Meyer, A. A. Wiles, O. Rivera, E. C. Wong, R. J. Freishtat, K. Rais-Bahrami, and H. J. Dalton, "Hemolytic and thrombocytopathic characteristics of extracorporeal membrane oxygenation systems at simulated flow rate for neonates," *Pediatr Crit Care Med,* vol. 13, no. 4, pp. e255-61, Jul, 2012.

[35] K. Yasui, R. Kosaka, M. Nishida, O. Maruyama, Y. Kawaguchi, and T. Yamane, "Optimal design of the hydrodynamic multi-arc bearing in a centrifugal blood pump for the improvement of bearing stiffness and hemolysis level," *Artif Organs,* vol. 37, no. 9, pp. 768-77, Sep, 2013.

[36] N. L. James, C. M. Wilkinson, N. L. Lingard, A. L. van der Meer, and J. C. Woodard, "Evaluation of hemolysis in the VentrAssist

implantable rotary blood pump," *Artif Organs,* vol. 27, no. 1, pp. 108-13, Jan, 2003.

[37] Y. Ohara, K. Makinouchi, J. Glueck, B. Sutherland, T. Shimono, K. Naito, K. Tasai, Y. Orime, S. Takatani, and Y. Nose, "Development and evaluation of antithrombogenic centrifugal pump: the Baylor C-Gyro Pump Eccentric Inlet Port Model," *Artif Organs,* vol. 18, no. 9, pp. 673-9, Sep, 1994.

[38] J. H. Yen, S. F. Chen, M. K. Chern, and P. C. Lu, "The effect of turbulent viscous shear stress on red blood cell hemolysis," *J Artif Organs,* vol. 17, no. 2, pp. 178-85, Jun, 2014.

[39] S. Park, S. Park, R. A. Jeong, H. Boo, J. Park, H. C. Kim, and T. D. Chung, "Nonenzymatic continuous glucose monitoring in human whole blood using electrified nanoporous Pt," *Biosens Bioelectron,* vol. 31, no. 1, pp. 284-91, Jan 15, 2012.

[40] N. Nakabayashi, "Preparation of biocompatible materials and their evaluation." pp. 591-598.

[41] C. H. Chan, I. L. Pieper, R. Hambly, G. Radley, A. Jones, Y. Friedmann, K. M. Hawkins, S. Westaby, G. Foster, and C. A. Thornton, "The CentriMag centrifugal blood pump as a benchmark for in vitro testing of hemocompatibility in implantable ventricular assist devices," *Artif Organs,* vol. 39, no. 2, pp. 93-101, Feb, 2015.

[42] H. R. Omar, M. Mirsaeidi, S. Socias, C. Sprenker, C. Caldeira, E. M. Camporesi, and D. Mangar, "Plasma Free Hemoglobin Is an Independent Predictor of Mortality among Patients on Extracorporeal

Membrane Oxygenation Support," *PLoS One,* vol. 10, no. 4, pp. e0124034, 2015.

[43] J. Park, D. A. Shin, S. Lee, Y. J. Cho, S. Jheon, J. C. Lee, and H. C. Kim, "Investigation of key circuit constituents affecting drug sequestration during extracorporeal membrane oxygenation treatment," *ASAIO J*, 2017.

[44] J. Guttendorf, A. J. Boujoukos, D. X. Ren, M. Q. Rosenzweig, and M. Hravnak, "Discharge Outcome in Adults Treated with Extracorporeal Membrane Oxygenation," *American Journal of Critical Care,* vol. 23, no. 5, pp. 365-376, Sep 1, 2014.

[45] D. W. Kays, S. Islam, D. S. Richards, S. D. Larson, J. M. Perkins, and J. L. Talbert, "Extracorporeal Life Support in Patients with Congenital Diaphragmatic Hernia: How Long Should We Treat?," *Journal of the American College of Surgeons,* vol. 218, no. 4, pp. 808-817, Apr, 2014.

[46] K. Shekar, J. F. Fraser, M. T. Smith, and J. A. Roberts, "Pharmacokinetic changes in patients receiving extracorporeal membrane oxygenation," *Journal of Critical Care,* vol. 27, no. 6, Dec, 2012.

[47] M. L. Buck, "Pharmacokinetic changes during extracorporeal membrane oxygenation - Implications for drug therapy of neonates," *Clinical Pharmacokinetics,* vol. 42, no. 5, pp. 403-417, 2003.

[48] K. Shekar, J. A. Roberts, C. I. Mcdonald, S. Fisquet, A. G. Barnett, D. V. Mullany, S. Ghassabian, S. C. Wallis, Y. L. Fung, M. T. Smith, and J. F. Fraser, "Sequestration of drugs in the circuit may lead to

therapeutic failure during extracorporeal membrane oxygenation," *Critical Care,* vol. 16, no. 5, 2012.

[49] K. Shekar, J. A. Roberts, C. I. Mcdonald, S. Ghassabian, C. Anstey, S. C. Wallis, D. V. Mullany, Y. L. Fung, and J. F. Fraser, "Protein-bound drugs are prone to sequestration in the extracorporeal membrane oxygenation circuit: results from an ex vivo study," *Critical Care,* vol. 19, Apr 14, 2015.

[50] N. M. Mehta, D. Halwick, B. L. Dodson, J. E. Thompson, and J. Arnold, "Potential drug sequestration during extracorporeal membrane oxygenation: results from an ex vivo experiment," *Intensive Care Medicine,* vol. 33, no. 6, pp. 1018-1024, Jun, 2007.

[51] E. D. Wildschut, M. J. Ahsman, K. Allegaert, R. A. A. Mathot, and D. Tibboel, "Determinants of drug absorption in different ECMO circuits," *Intensive Care Medicine,* vol. 36, no. 12, pp. 2109-2116, Dec, 2010.

[52] K. Shekar, J. A. Roberts, M. T. Smith, Y. L. Fung, and J. F. Fraser, "The ECMO PK Project: an incremental research approach to advance understanding of the pharmacokinetic alterations and improve patient outcomes during extracorporeal membrane oxygenation," *Bmc Anesthesiology,* vol. 13, Mar 21, 2013.

[53] P. K. Smith, A. K. Mallia, and G. T. Hermanson, "Colorimetric method for the assay of heparin content in immobilized heparin preparations," *Anal Biochem,* vol. 109, no. 2, pp. 466-73, Dec, 1980.

[54] J. C. de Winter, "Using the Student's t-test with extremely small sample sizes," *Practical Assessment, Research & Evaluation,* vol. 18,

no. 10, pp. 1-12, 2013.

[55] D. Wagner, D. Pasko, K. Phillips, J. Waldvogel, and G. Annich, "In vitro clearance of dexmedetomidine in extracorporeal membrane oxygenation," *Perfusion,* vol. 28, no. 1, pp. 40-6, Jan, 2013.

[56] T. J. Preston, A. B. Hodge, J. B. Riley, C. Leib-Sargel, and K. K. Nicol, "In vitro drug adsorption and plasma free hemoglobin levels associated with hollow fiber oxygenators in the extracorporeal life support (ECLS) circuit," *J Extra Corpor Technol,* vol. 39, no. 4, pp. 234-7, Dec, 2007.

[57] S. Abuhasna, A. Al Jundi, W. Abdelatty, and M. Urrahman, "Evaluation of long-term infusion of dexmedetomidine in critically ill patients: A retrospective analysis," *Int J Crit Illn Inj Sci,* vol. 2, no. 2, pp. 70-4, May, 2012.

[58] J. Afonso, and F. Reis, "Dexmedetomidine: current role in anesthesia and intensive care," *Rev Bras Anestesiol,* vol. 62, no. 1, pp. 118-33, Jan-Feb, 2012.

[59] M. Kaur, and P. M. Singh, "Current role of dexmedetomidine in clinical anesthesia and intensive care," *Anesth Essays Res,* vol. 5, no. 2, pp. 128-33, Jul-Dec, 2011.

[60] M. Wujtewicz, D. Maciejewski, H. Misiołek, A. Fijałkowska, T. Gaszyński, P. Knapik, and R. Lango, "Use of dexmedetomidine in the adult intensive care unit," *Anaesthesiology intensive therapy,* vol. 45, no. 4, pp. 235-240, 2013.

[61] S. M. Jakob, E. Ruokonen, R. M. Grounds, T. Sarapohja, C. Garratt, S. J. Pocock, J. R. Bratty, J. Takala, and D. L.-T. Sedation,

"Dexmedetomidine vs Midazolam or Propofol for Sedation During Prolonged Mechanical Ventilation Two Randomized Controlled Trials," *Jama-Journal of the American Medical Association,* vol. 307, no. 11, pp. 1151-1160, Mar 21, 2012.

[62] P. Pandharipande, A. Shintani, J. Peterson, B. T. Pun, G. R. Wilkinson, R. S. Dittus, G. R. Bernard, and E. W. Ely, "Lorazepam is an independent risk factor for transitioning to delirium in intensive care unit patients," *Anesthesiology,* vol. 104, no. 1, pp. 21-26, Jan, 2006.

[63] S. Ouimet, B. P. Kavanagh, S. Gottfried, and Y. Skrobik, "Incidence, risk factors and consequences of ICU delirium," *Intensive Care Medicine,* vol. 33, no. 1, pp. 66-73, Jan, 2007.

[64] R. P. Patel, M. Gambrell, T. Speroff, T. A. Scott, B. T. Pun, J. Okahashi, C. Strength, P. Pandharipande, T. D. Girard, and H. Burgess, "Delirium and sedation in the intensive care unit (ICU): survey of behaviors and attitudes of 1,384 healthcare professionals," *Critical care medicine,* vol. 37, no. 3, pp. 825, 2009.

[65] Y. Shehabi, J. A. Botha, M. S. Boyle, D. Ernest, R. C. Freebairn, I. R. Jenkins, B. L. Roberts, and I. M. Seppelt, "Sedation and delirium in the intensive care unit: an Australian and New Zealand perspective," *Anaesthesia and Intensive Care,* vol. 36, no. 4, pp. 570-578, Jul, 2008.

[66] R. R. Riker, Y. Shehabi, P. M. Bokesch, D. Ceraso, W. Wisemandle, F. Koura, P. Whitten, B. D. Margolis, D. W. Byrne, E. W. Ely, M. G. Rocha, and S. S. Grp, "Dexmedetomidine vs Midazolam for Sedation of Critically Ill Patients A Randomized Trial," *Jama-Journal of the*

American Medical Association, vol. 301, no. 5, pp. 489-499, Feb 4, 2009.

[67] K. Berthoin, C. S. Le Duff, J. Marchand-Brynaert, S. Carryn, and P. M. Tulkens, "Stability of meropenem and doripenem solutions for administration by continuous infusion," *J Antimicrob Chemother,* vol. 65, no. 5, pp. 1073-5, May, 2010.

[68] J. Park, G. H. Lee, J. Y. Park, J. C. Lee, and H. C. Kim, "A numerical study of the Coriolis effect in centrifugal microfluidics with different channel arrangements," *Microfluidics and Nanofluidics,* vol. 20, no. 4, Apr, 2016.

[69] M. Madou, J. Zoval, G. Y. Jia, H. Kido, J. Kim, and N. Kim, "Lab on a CD," *Annual Review of Biomedical Engineering,* vol. 8, pp. 601-628, 2006.

[70] T. Brenner, T. Glatzel, R. Zengerle, and J. Ducree, "Frequency-dependent transversal flow control in centrifugal microfluidics," *Lab Chip,* vol. 5, no. 2, pp. 146-50, Feb, 2005.

[71] S. I. E. Lin, "Novel Bifurcation Design for Centrifugal Microfluidic Platform With Wide Range Rotational Speed," *Journal of Nanotechnology in Engineering and Medicine,* vol. 2, no. 1, pp. 011001, 2011.

[72] S. Haeberle, T. Brenner, H. P. Schlosser, R. Zengerle, and J. Ducree, "Centrifugal micromixer," *Chemical Engineering & Technology,* vol. 28, no. 5, pp. 613-616, May, 2005.

[73] M. La, S. J. Park, H. W. Kim, J. J. Park, K. T. Ahn, S. M. Ryew, and

D. S. Kim, “A centrifugal force-based serpentine micromixer (CSM) on a plastic lab-on-a-disk for biochemical assays,” *Microfluidics and Nanofluidics,* vol. 15, no. 1, pp. 87-98, Jul, 2013.

[74] J. Ducrée, S. Haeberle, T. Brenner, T. Glatzel, and R. Zengerle, “Patterning of flow and mixing in rotating radial microchannels,” *Microfluidics and Nanofluidics,* vol. 2, no. 2, pp. 97-105, 2005.

[75] J. Ducrée, T. Brenner, S. Haeberle, T. Glatzel, and R. Zengerle, “Multilamination of flows in planar networks of rotating microchannels,” *Microfluidics and Nanofluidics,* vol. 2, no. 1, pp. 78-84, 2005.

[76] Y. K. Suh, and S. Kang, “A Review on Mixing in Microfluidics,” *Micromachines,* vol. 1, no. 3, pp. 82-111, 2010.

[77] S. H. Lee, D. van Noort, J. Y. Lee, B. T. Zhang, and T. H. Park, “Effective mixing in a microfluidic chip using magnetic particles,” *Lab Chip,* vol. 9, no. 3, pp. 479-82, Feb 7, 2009.

[78] Y. Wang, J. Zhe, B. T. F. Chung, and P. Dutta, “A rapid magnetic particle driven micromixer,” *Microfluidics and Nanofluidics,* vol. 4, no. 5, pp. 375-389, 2007.

[79] A. Rida, and M. A. M. Gijs, “Manipulation of self-assembled structures of magnetic beads for microfluidic mixing and assaying,” *Analytical Chemistry,* vol. 76, no. 21, pp. 6239-6246, Nov 1, 2004.

[80] A. Folch, B. R. Utela, H. Lai, and A. K. Au, “Microvalves and Micropumps for BioMEMS,” *Micromachines,* vol. 2, no. 2, pp. 179-220, 2011.

[81] M. Liu, J. Zhang, Y. Liu, W. M. Lau, and J. Yang, "Modeling of Flow Burst, Flow Timing in Lab-on-a-CD Systems and Its Application in Digital Chemical Analysis," *Chemical Engineering & Technology,* vol. 31, no. 9, pp. 1328-1335, 2008.

[82] Y.-J. Chang, S.-C. Chen, and C.-L. Hsu, "Study on Microchannel Design and Burst Frequency Detection for Centrifugal Microfluidic System," *Advances in Materials Science and Engineering,* vol. 2013, pp. 1-9, 2013.

[83] P. Roy, N. K. Anand, and D. Banerjee, "Numerical simulation of flow and heat transfer in radially rotating microchannels," *Microfluidics and Nanofluidics,* vol. 15, no. 3, pp. 397-413, 2013.

[84] Y. Ren, and W. Woon-Fong Leung, "Flow and mixing in rotating zigzag microchannel," *Chemical Engineering Journal,* vol. 215-216 pp. 561–578, 2012.

[85] T. Glatzel, C. Litterst, C. Cupelli, T. Lindemann, C. Moosmann, R. Niekrawletz, W. Streule, R. Zengerle, and P. Koltay, "Computational fluid dynamics (CFD) software tools for microfluidic applications - A case study," *Computers & Fluids,* vol. 37, no. 3, pp. 218-235, Mar, 2008.

[86] D. C. Duffy, H. L. Gillis, J. Lin, N. F. Sheppard, and G. J. Kellogg, "Microfabricated centrifugal microfluidic systems: Characterization and multiple enzymatic assays," *Analytical Chemistry,* vol. 71, no. 20, pp. 4669-4678, Oct 15, 1999.

[87] D. Boskovic, S. Lobbecke, A. Gross, and M. Kohler, "Residence Time

Distribution Studies in Microfluidic Mixing Structures," *Chemical Engineering & Technology,* vol. 34, no. 3, pp. 361-370, Mar, 2011.

[88] Y. Ukita, and Y. Takamura, "Switching of secondary flow behavior on centrifugal microfluidics," in 16th International Conference on Miniaturized Systems for Chemistry and Life Sciences, Okinawa, Japan, 2012.

[89] J. Park, J. C. Lee, and H. C. Kim, "Centrifugal microfluidic-based viscometer," 2015.

[90] Y. I. Cho, M. P. Mooney, and D. J. Cho, "Hemorheological disorders in diabetes mellitus," *Journal of diabetes science and technology,* vol. 2, no. 6, pp. 1130-1138, 2008.

[91] C. W. van der Elst, A. F. Malan, and H. V. de Heese, "Blood viscosity in modern medicine," *S Afr Med J,* vol. 52, no. 13, pp. 526-8, Sep 17, 1977.

[92] C. J. Pipe, and G. H. McKinley, "Microfluidic rheometry," *Mechanics Research Communications,* vol. 36, no. 1, pp. 110-120, 2009.

[93] Y. J. Kang, and S. Yang, "Integrated microfluidic viscometer equipped with fluid temperature controller for measurement of viscosity in complex fluids," *Microfluidics and Nanofluidics,* vol. 14, no. 3-4, pp. 657-668, Mar, 2013.

[94] Y. J. Kang, S. Y. Yoon, K. H. Lee, and S. Yang, "A highly accurate and consistent microfluidic viscometer for continuous blood viscosity measurement," *Artif Organs,* vol. 34, no. 11, pp. 944-9, Nov, 2010.

[95] J. Park, G. H. Lee, J. Y. Park, J. C. Lee, and H. C. Kim, "Hypergravity-

induced multicellular spheroid generation with different morphological patterns precisely controlled on centrifugal microfluidic platform." - in preparation for submission to Sicence Citation index (SCI) journal by adding computational simulation results conducted by Lee, G. H. Park, J.'s contributions include device manufacturing and data analysis by image processing. Lee, G. H.'s contributions include cell experiments and computational simulation.

[96] E. Fennema, N. Rivron, J. Rouwkema, C. van Blitterswijk, and J. de Boer, "Spheroid culture as a tool for creating 3D complex tissues," *Trends in Biotechnology,* vol. 31, no. 2, pp. 108-115, Feb, 2013.

[97] M. Ravi, V. Paramesh, S. R. Kaviya, E. Anuradha, and F. D. P. Solomon, "3D Cell Culture Systems: Advantages and Applications," *Journal of Cellular Physiology,* vol. 230, no. 1, pp. 16-26, Jan, 2015.

[98] Z. Cesarz, and K. Tamama, "Spheroid Culture of Mesenchymal Stem Cells," *Stem Cells International,* vol. 2015, 2015.

[99] Y. Li, G. Guo, L. Li, F. Chen, J. Bao, Y. J. Shi, and H. Bu, "Three-dimensional spheroid culture of human umbilical cord mesenchymal stem cells promotes cell yield and stemness maintenance," *Cell and Tissue Research,* vol. 360, no. 2, pp. 297-307, May, 2015.

[100] Y. Yamaguchi, J. Ohno, A. Sato, H. Kido, and T. Fukushima, "Mesenchymal stem cell spheroids exhibit enhanced in-vitro and in-vivo osteoregenerative potential," *Bmc Biotechnology,* vol. 14, Dec 6, 2014.

[101] Y. C. Tung, A. Y. Hsiao, S. G. Allen, Y. S. Torisawa, M. Ho, and S.

Takayama, “High-throughput 3D spheroid culture and drug testing using a 384 hanging drop array,” *Analyst,* vol. 136, no. 3, pp. 473-478, 2011.

[102] J. Carlsson, and J. Yuhas, "Liquid-overlay culture of cellular spheroids," *Spheroids in cancer research*, pp. 1-23: Springer, 1984.

[103] T. Korff, T. Krauss, and H. G. Augustin, “Three-dimensional spheroidal culture of cytotrophoblast cells mimics the phenotype and differentiation of cytotrophoblasts from normal and preeclamptic pregnancies,” *Experimental Cell Research,* vol. 297, no. 2, pp. 415-423, Jul 15, 2004.

[104] R. Z. Lin, and H. Y. Chang, “Recent advances in three-dimensional multicellular spheroid culture for biomedical research,” *Biotechnol J,* vol. 3, no. 9-10, pp. 1172-84, Oct, 2008.

[105] G. Mehta, A. Y. Hsiao, M. Ingram, G. D. Luker, and S. Takayama, “Opportunities and challenges for use of tumor spheroids as models to test drug delivery and efficacy,” *Journal of Controlled Release,* vol. 164, no. 2, pp. 192-204, Dec 10, 2012.

[106] W. Metzger, D. Sossong, A. Bachle, N. Putz, G. Wennemuth, T. Pohlemann, and M. Oberringer, “The liquid overlay technique is the key to formation of co-culture spheroids consisting of primary osteoblasts, fibroblasts and endothelial cells,” *Cytotherapy,* vol. 13, no. 8, pp. 1000-1012, Sep, 2011.

[107] A. Ivascu, and M. Kubbies, “Rapid generation of single-tumor spheroids for high-throughput cell function and toxicity analysis,”

Journal of Biomolecular Screening, vol. 11, no. 8, pp. 922-932, Dec, 2006.

[108] A. Tschopp, and A. Cogoli, "Hypergravity Promotes Cell-Proliferation," *Experientia,* vol. 39, no. 12, pp. 1323-1329, 1983.

[109] Y. S. Park, V. Sunkara, Y. Kim, W. S. Lee, J. R. Han, and Y. K. Cho, "Fully Automated Centrifugal Microfluidic Device for Ultrasensitive Protein Detection from Whole Blood," *Jove-Journal of Visualized Experiments*, no. 110, Apr, 2016.

[110] A. Lee, J. Park, M. Lim, V. Sunkara, S. Y. Kim, G. H. Kim, M. H. Kim, and Y. K. Cho, "All-in-One Centrifugal Microfluidic Device for Size-Selective Circulating Tumor Cell Isolation with High Purity," *Analytical Chemistry,* vol. 86, no. 22, pp. 11349-11356, Nov 18, 2014.

[111] I. J. Michael, T. H. Kim, V. Sunkara, and Y. K. Cho, "Challenges and Opportunities of Centrifugal Microfluidics for Extreme Point-of-Care Testing," *Micromachines,* vol. 7, no. 2, Feb, 2016.

[112] R. Gorkin, J. Park, J. Siegrist, M. Amasia, B. S. Lee, J. M. Park, J. Kim, H. Kim, M. Madou, and Y. K. Cho, "Centrifugal microfluidics for biomedical applications," *Lab on a Chip,* vol. 10, no. 14, pp. 1758-1773, 2010.

[113] X. Zhao, S. Du, L. Chai, Y. Xu, L. Liu, X. Zhou, J. Wang, W. Zhang, C.-H. Liu, and X. Wang, "Anti-cancer drug screening based on a adipose-derived stem cell/hepatocyte 3D printing technique," *Journal of Stem Cell Research & Therapy,* vol. 2015, 2015.

[114] Y. R. Lea-Currie, D. J. Duffin, and B. M. Buehrer, "Use of adipose-

derived stem cells in high-throughput screening to identify modulators of lipogenesis," *Adipose-Derived Stem Cells: Methods and Protocols*, pp. 359-368, 2011.

[115] M. Perard, S. Tricot-Doleux, P. Pellen-Mussi, F. Meary, and F. Pérez, "Evaluation of the cytotoxicity of pulp floor perforation filling materials by using in parallel 2d and 3d culture models," *Bulletin du Groupement International pour la Recherche Scientifique en Stomatologie et Odontologie,* vol. 50, no. 2, pp. 42-43, 2011.

[116] M. Majety, L. P. Pradel, M. Gies, and C. H. Ries, "Fibroblasts Influence Survival and Therapeutic Response in a 3D Co-Culture Model," *PloS one,* vol. 10, no. 6, pp. e0127948, 2015.

[117] M. A. Lancaster, M. Renner, C. A. Martin, D. Wenzel, L. S. Bicknell, M. E. Hurles, T. Homfray, J. M. Penninger, A. P. Jackson, and J. A. Knoblich, "Cerebral organoids model human brain development and microcephaly," *Nature,* vol. 501, no. 7467, pp. 373-9, Sep 19, 2013.

[118] A. Rocca, A. Marino, V. Rocca, S. Moscato, G. de Vito, V. Piazza, B. Mazzolai, V. Mattoli, T. J. Ngo-Anh, and G. Ciofani, "Barium titanate nanoparticles and hypergravity stimulation improve differentiation of mesenchymal stem cells into osteoblasts," *Int J Nanomedicine,* vol. 10, pp. 433-45, 2015.

[119] G. G. Genchi, F. Cialdai, M. Monici, B. Mazzolai, V. Mattoli, and G. Ciofani, "Hypergravity stimulation enhances PC12 neuron-like cell differentiation," *Biomed Res Int,* vol. 2015, pp. 748121, 2015.

[120] C. Xinaris, V. Brizi, and G. Remuzzi, "Organoid Models and

Applications in Biomedical Research," *Nephron,* vol. 130, no. 3, pp. 191-9, 2015.

[121] J. C. McDonald, D. C. Duffy, J. R. Anderson, D. T. Chiu, H. K. Wu, O. J. A. Schueller, and G. M. Whitesides, "Fabrication of microfluidic systems in poly(dimethylsiloxane)," *Electrophoresis,* vol. 21, no. 1, pp. 27-40, Jan, 2000.

[122] V. Vishnu, K. Aneesa, A. Lal, and A. Nabi, "Real Time DC Motor Speed Control Using PID in LabVIEW with Arduino," *Imperial Journal of Interdisciplinary Research,* vol. 2, no. 5, 2016.

[123] G. C. Cho, J. Dodds, and J. C. Santamarina, "Particle shape effects on packing density, stiffness, and strength: Natural and crushed sands," *Journal of Geotechnical and Geoenvironmental Engineering,* vol. 132, no. 5, pp. 591-602, May, 2006.

[124] J. Friedrich, C. Seidel, R. Ebner, and L. A. Kunz-Schughart, "Spheroid-based drug screen: considerations and practical approach," *Nat Protoc,* vol. 4, no. 3, pp. 309-24, 2009.

[125] R. Edmondson, J. J. Broglie, A. F. Adcock, and L. J. Yang, "Three-Dimensional Cell Culture Systems and Their Applications in Drug Discovery and Cell-Based Biosensors," *Assay and Drug Development Technologies,* vol. 12, no. 4, pp. 207-218, May 1, 2014.

[126] A. Mobley, S. K. Linder, R. Braeuer, L. M. Ellis, and L. Zwelling, "A Survey on Data Reproducibility in Cancer Research Provides Insights into Our Limited Ability to Translate Findings from the Laboratory to the Clinic," *Plos One,* vol. 8, no. 5, May 15, 2013.

[127] M. Zanoni, F. Piccinini, C. Arienti, A. Zamagni, S. Santi, R. Polico, A. Bevilacqua, and A. Tesei, "3D tumor spheroid models for in vitro therapeutic screening: a systematic approach to enhance the biological relevance of data obtained," *Scientific reports,* vol. 6, 2016.

[128] R. Macarron, M. N. Banks, D. Bojanic, D. J. Burns, D. A. Cirovic, T. Garyantes, D. V. S. Green, R. P. Hertzberg, W. P. Janzen, J. W. Paslay, U. Schopfer, and G. S. Sittampalam, "Impact of high-throughput screening in biomedical research," *Nature Reviews Drug Discovery,* vol. 10, no. 3, pp. 188-195, Mar, 2011.

[129] J. Antonchuk, "Formation of embryoid bodies from human pluripotent stem cells using AggreWell™ plates," *Basic Cell Culture Protocols*, pp. 523-533, 2013.

[130] L. Goers, P. Freemont, and K. M. Polizzi, "Co-culture systems and technologies: taking synthetic biology to the next level," *Journal of the Royal Society Interface,* vol. 11, no. 96, Jul 6, 2014.

[131] J. Allard, and A. Mogilner, "Traveling waves in actin dynamics and cell motility," *Current Opinion in Cell Biology,* vol. 25, no. 1, pp. 107-115, Feb, 2013.

[132] D. A. Lauffenburger, and A. F. Horwitz, "Cell migration: A physically integrated molecular process," *Cell,* vol. 84, no. 3, pp. 359-369, Feb 9, 1996.

[133] J. Park, G. H. Lee, J. Y. Park, J. C. Lee, and H. C. Kim, "A study on adipose-derived stem cells adaptions to hypergravity environment using a portable centrifugal cell culture system ". - in preparation for

submission to Sicence Citation index (SCI) journal with an additional experimental data.

[134] S. D. Pringle, P. W. Macfarlane, and S. M. Cobbe, "Response of heart rate to a roller coaster ride," *BMJ,* vol. 299, no. 6715, pp. 1575, Dec 23-30, 1989.

[135] *Saturn 5 launch vehicle flight evaluation report, AS-510, Apollo 15 mission*, 1971.

[136] D. E. Watenpaugh, "Fluid volume control during short-term space flight and implications for human performance," *Journal of Experimental Biology,* vol. 204, no. 18, pp. 3209-3215, Sep, 2001.

[137] F. W. Booth, "Terrestrial Applications of Bone and Muscle Research in Microgravity," *Life Sciences and Space Research Xxv (1): Gravitational Biology,* vol. 14, no. 8, pp. 373-376, 1994.

[138] D. B. Deever, R. S. Young, S. Wang, B. A. Bradshaw, J. Miles, C. R. Pettis, and M. L. Witten, "Changes in organ perfusion and weight ratios in post-simulated microgravity recovery," *Acta Astronaut,* vol. 50, no. 7, pp. 445-52, Apr, 2002.

[139] A. Tschopp, and A. Cogoli, "Hypergravity promotes cell proliferation," *Experientia,* vol. 39, no. 12, pp. 1323-9, Dec 15, 1983.

[140] W. Hertl, W. S. Ramsey, and E. D. Nowlan, "Assessment of cell-substrate adhesion by a centrifugal method," *In Vitro,* vol. 20, no. 10, pp. 796-801, Oct, 1984.

[141] J. A. Maier, F. Cialdai, M. Monici, and L. Morbidelli, "The impact of microgravity and hypergravity on endothelial cells," *Biomed Res Int,*

vol. 2015, pp. 434803, 2015.

[142] T. Russomano, M. R. Rizzatti, R. P. Coelho, D. Scolari, D. De Souza, and P. Pra-Veleda, “Effects of simulated hypergravity on biomedical experiments,” *IEEE Eng Med Biol Mag,* vol. 26, no. 3, pp. 66-71, May-Jun, 2007.

[143] J. M. Gimble, A. J. Katz, and B. A. Bunnell, “Adipose-derived stem cells for regenerative medicine,” *Circ Res,* vol. 100, no. 9, pp. 1249-60, May 11, 2007.

[144] S. M. Willerth, and S. E. Sakiyama-Elbert, "Combining stem cells and biomaterial scaffolds for constructing tissues and cell delivery," *StemBook*, Cambridge (MA), 2008.

[145] M. M. Nava, M. T. Raimondi, and R. Pietrabissa, “Controlling self-renewal and differentiation of stem cells via mechanical cues,” *J Biomed Biotechnol,* vol. 2012, pp. 797410, 2012.

[146] Y. Mine, T. Hayashi, M. Yamada, H. Okano, and T. Kawase, “Environmental cue-dependent dopaminergic neuronal differentiation and functional effect of grafted neuroepithelial stem cells in parkinsonian brain,” *Neurosurgery,* vol. 65, no. 4, pp. 741-53; discussion 753, Oct, 2009.

[147] J. R. Anderson, D. T. Chiu, H. Wu, O. Schueller, and G. M. Whitesides, “Fabrication of microfluidic systems in poly (dimethylsiloxane),” *Electrophoresis,* vol. 21, no. 1, pp. 27-40, 2000.

[148] R. McBeath, D. M. Pirone, C. M. Nelson, K. Bhadriraju, and C. S. Chen, “Cell shape, cytoskeletal tension, and RhoA regulate stem cell lineage

commitment," *Dev Cell,* vol. 6, no. 4, pp. 483-95, Apr, 2004.

[149] A. Schaffler, and C. Buchler, "Concise review: adipose tissue-derived stromal cells--basic and clinical implications for novel cell-based therapies," *Stem Cells,* vol. 25, no. 4, pp. 818-27, Apr, 2007.

[150] G. Li, N. Fu, X. Yang, M. Li, K. Ba, X. Wei, Y. Fu, Y. Yao, X. Cai, and Y. Lin, "Mechanical compressive force inhibits adipogenesis of adipose stem cells," *Cell Prolif,* vol. 46, no. 5, pp. 586-94, Oct, 2013.

[151] W. C. Lee, T. M. Maul, D. A. Vorp, J. P. Rubin, and K. G. Marra, "Effects of uniaxial cyclic strain on adipose-derived stem cell morphology, proliferation, and differentiation," *Biomech Model Mechanobiol,* vol. 6, no. 4, pp. 265-73, Jul, 2007.

[152] S. Amin, S. E. Banijamali, M. Tafazoli-Shadpour, M. A. Shokrgozar, M. M. Dehghan, N. Haghighipour, R. Mahdian, V. Bayati, and P. Abbasnia, "Comparing the effect of equiaxial cyclic mechanical stimulation on GATA4 expression in adipose-derived and bone marrow-derived mesenchymal stem cells," *Cell biology international,* vol. 38, no. 2, pp. 219-227, 2014.

[153] S. Shojaei, M. Tafazzoli-Shahdpour, M. A. Shokrgozar, and N. Haghighipour, "Effects of mechanical and chemical stimuli on differentiation of human adipose-derived stem cells into endothelial cells," *Int J Artif Organs,* vol. 36, no. 9, pp. 663-73, Oct 3, 2013.

[154] M. Knippenberg, M. N. Helder, B. Z. Doulabi, C. M. Semeins, P. I. Wuisman, and J. Klein-Nulend, "Adipose tissue-derived mesenchymal stem cells acquire bone cell-like responsiveness to fluid shear stress on

osteogenic stimulation," *Tissue Eng,* vol. 11, no. 11-12, pp. 1780-8, Nov-Dec, 2005.

[155] T. D. Brown, "Techniques for mechanical stimulation of cells in vitro: a review," *J Biomech,* vol. 33, no. 1, pp. 3-14, Jan, 2000.

Abstract in Korean

국문 초록

본 논문은 원심력 기반 유체 시스템의 생물의학적 응용에 관한 연구를 목적으로 매크로 및 마이크로 기술을 접목하여 낮은 용혈성 원심혈액 펌프 기반의 심폐순환보조장치, 고중력 기반의 세포배양장치와 세포 스페로이드 생성 장치, 그리고 소체적 점도계에 대한 설계, 제작, 성능평가 등을 포함하는 단계적인 개발을 수행하였다.

매크로 단위 연구로는 핵심 모니터링 센서들이 하나의 시스템으로 결합될 수 있는 스마트 올인원 형태의 심폐순환보조장치를 개발하고 더블 피봇베어링 디자인을 통해 낮은 용혈성 원심혈액펌프를 개발할 수 있었다. 동물실험을 통해 통합시스템에 장착한 원심혈액펌프의 체내 성능을 살펴 본 결과 6시간 동안 기술적 문제 없이 정상돼지에 적용 될 수 있었고 혈액적합성 코팅을 통해 혈액 응고 및 용혈 측면에서 매우 향상된 결과를 얻을 수 있었다. 이와 더불어 상용화 체외막산소화 제품의 재료에 따른 항생제, 진정제, 그리고 항응고제에 대한 약물 흡착 차이를 분석해 본 결과 폴리비닐클로라이드 재질로 이루어진 튜빙과 폴리우레탄 섬유질로 제작된 산화기의 열교환 맴브레인이 약물흡착에 가장 주원인으로 작용하고 있음을 밝혀낼 수 있었다.

마이크로 단위 연구로는 채널 배치에 따른 코리올리 효과의

영향력을 수치해석을 통해 살펴보았다. 그 결과 채널의 각도가 존재할 경우 낮은 회전 속도에서도 유체의 흐름 방향을 변환할 수 있을 정도로 충분히 유체를 측면으로 밀어내는 코리올리 효과를 발생시킬 수 있으며 높은 회전속도에서는 코리올리 효과를 유지하면서 채널 배치에 따라 유체흐름 속도를 효과적으로 제어할 수 있음을 확인하였다. 이와 같이 수치해석을 통한 원심미세유체역학에 대한 이해를 바탕으로 응용연구를 수행하기 위해서 소형 회전장치를 제작하였다. 다수의 저항 채널을 포함하는 부채꼴 모양의 채널 디자인을 통해 서로 다른 점성을 가지고 있는 유체가 푸와죄유 원리에 따라 서로 다른 개수의 저항채널에 채워짐으로써 점성의 상대적 측정이 가능함을 확인하였다. 원형으로 배치된 100여개의 마이크로 웰 디자인을 통해 원심력 기반 세포 스페로이드 생성장치를 개발하였고 기존 방법에 비해 스페로이드 구형도 및 크기와 모양의 일관성을 상당히 향상시킬 수 있음을 확인하였다. 또한 고중력 하에서 세포 배양이 가능하도록 세포배양칩을 끼워 넣을 수 있는 회전 플랫폼을 제작하여 고중력 환경에서의 지방 줄기세포 적응 연구를 수행하였다. 그 결과 세포 증식이 향상되는 것을 확인할 수 있었다.

핵심어: 원심력, 심폐순환보조 장치, 용혈 평가, 약물 흡착, 원심미세유체역학 플랫폼, 고중력

학번 : 2012-21018